New Detectors for Electron Microscopy

A Thesis submission for the degree of

Doctor of Philosophy in Materials Science

Robert Clough

Mansfield College

The University of Oxford

2015

Abstract

Detectors for Electron Microscopy have traditionally used a scintillator to generate photons from fast electrons, which are then detected by a sensor. However, in recent years direct detection has become an area of interest due to the potential improvements to detector performance.

In this thesis various aspects of direct detection are presented. I will begin with simulations of direct detectors based on Joy's model of straight trajectories between Rutherford scattering events, where signal is generated by inelastic scattering events. The effects of microscope operating voltage, detector thickness, a surface electrically dead layer and diode depth on detector performance are presented.

A prototype detector was developed using the DUOS sensor, two thicknesses of the sensor were produced a 50μm thick detector and a 20μm thick detector. EBSD results are presented which show how the use of a reactive ion etch to reduce the dead layer thickness of a mechanically thinned sensor improve the detection efficiency of a sensor allowing EBSD work to be carried out at operating voltages as low as 5keV.

The MTF and DQE of both thicknesses of DUOS sensor are measured at 80kV and 200kV, which show that there is little difference between the two thicknesses at 80kV, but at 200kV the thinner detector shows an improved MTF. The results are then and compared with the equivalent simulated detectors. I show how the high frame rate of a detector and rigid and non-rigid registration can be used to improve image quality, resolving the $\{331\}$ lattice spacing which is not visible with a simple summation of frames.

Detectors using gallium nitride rather than silicon as the base semiconductor are simulated. The MTF at the Nyquist frequency for a GaN detector is double that of a Si detector at an operating voltages of 80kV due to the smaller interaction volume of

an electron in GaN. However, at higher voltages the improvement is much smaller as most electrons pass through the detector.

Acknowledgements

I would like to thank my supervisor Professor Angus Kirkland for his encouragement and expertise. Throughout my time as a research student he has gone above and beyond to help me succeed.

I would like to thank Dr. Grigore Moldovan for his invaluable knowledge and helping me to grasp many of the basics of the field.

I would like to thank my fellow colleagues in my research group both past and present who have helped in a myriad of ways, from help with acquiring data to helping me interpret my results.

I would like to thank the Engineering and Physical Sciences Research Council for funding my research.

I would like to thank the Department of Materials and Mansfield College at the University of Oxford for supporting me with facilities and funding to attend conferences.

I would like to thank the Institute of Structural Molecular Biology at Birkbeck College and the Center for Functional Nanomaterials at Brookhaven National Lab for access to their instruments to carry out experimental work.

Finally I would like to thank my wife, Grace, for her emotional support through the highs and lows that are an inevitable part of research.

Contents

Glossary

Abbreviations

ADC Analogue to Digital Converter.

CCD Charge Coupled Device.

CMOS Complementary metal-oxide semiconductor.

COB Chip on Board.

DDD Direct Detection Device.

DFT Discrete Fourier Transform.

DSSD Double Sided Strip Detector.

DQE Detective Quantum Efficiency.

EBSD Electron Backscatter Diffraction.

ELT Enclosed Layout Transistor.

FFT Fast Fourier Transform.

HAPS Hybrid Active Pixel Sensor.

MAPS Monolithic Active Pixel Sensor.

MOSFET Metal-Oxide-Semiconductor Field-Effect Transistor.

MTF Modulation Transfer Function.

NPS Noise Power Spectrum.

NNPS Normalised Noise Power Spectrum.

PCB Printed Circuit Board.

PSF Point Spread Function.

RIE Reactive Ion Etch.

SEM Scanning Electron Microscopy.

SOI Wafer Silicon on Insulator Wafer.

STEM Scanning Transmission Electron Microscopy.

TEM Transmission Electron Microscopy.

TMAH Tetra-Methyl Ammonium Hydroxide.

Commonly Used Terminology

Detector The full system mounted on a microscope.

Dead Layer A layer in the sensor where energy is not deposited in a detectable form due to a high concentration of recombination centres.

Dynamic Range The number of primary electrons that are required to saturate the detector.

Joy's Model A model for electron trajectories through a material as straight trajectories between Rutherford scattering events.

Pedestal Level The mean pixel count of an unilluminated detector.

Primary Electron A high energy electron which enters the sensor and generates signal.

Pulse Height Distribution The probability distribution of energy deposited by a primary electron.

Readout Electronics The electronics which convert signal generated in the sensitive layer into an image.

Saturation Level The mean pixel count where an increase in dose does not increase the pixel value.

Sensor The semiconductor structure containing the pixels and sensitive volume where charge is generated.

Chapter 1

Introduction and Background

1.1 Introduction

Prior to the introduction of digital detectors, photographic film was the preferred method for recording images in Transmission Electron Microscopy. However there are a number of limitations associated with film; the lengthy development process, difficulties in digitising images, poor signal to noise ratio at low exposure due to high background noise and a non-linear response to electron dose. All of these make this medium undesirable for recording data for quantitative analysis [1–3]. These problems associated with film are not an issue for digital detectors, where large datasets can be generated with immediate feedback in a digital form and with appropriate pixel design and correct gain normalisation the pixel response is almost linear. Charge Coupled Device (CCD) detectors are the most widely used in electron microscopy. However, due to their low radiation hardness [4] CCD detectors are in general operated as indirect detectors in which the CCD is coupled to a scintillator. In this mode electrons dissipate their energy in the scintillator generating photons which are transferred to the detector by either fibre optic or optical coupling and are subsequently detected by the CCD. The major disadvantages of this geometry are the large interaction volume of the electron in the scintillator causing photons to be detected over a large area and optical blurring arising from the coupling system. This implies that a single electron can be detected as signal generated in a relatively large number of pixels, in turn causing blurring of fine features. For this reason CCD detectors have performed relatively poorly compared to photographic film [1, 2, 5, 6] and for many years digital detectors and film have been used side by side. However in recent years the capabilities of digital detectors have begun to match those of film and a "phasing out" of film as the preferred detection medium has been observed. However the issues related to indirect detection still exist.

Direct Detection Devices (DDD) are alternatives to scintillator coupled detectors, where electrons are converted directly to signal in the active layer of the detector. The most common implementation of direct detection uses active pixel sensors. These sensors utilise complementary metal-oxide-semiconductor (CMOS) technology to produce a pixel array. The wider applications of CMOS technology mean that CMOS detectors tend to be cheaper, have faster readout and the higher resolution of CMOS processing makes smaller pixel sizes possible [7]. Active pixel sensors come in two forms; Hybrid Active Pixel Sensors (HAPS) and Monolithic Active Pixel Sensors (MAPS). HAPS are made from two wafers, a detection wafer that contains the pixel structures that collect the charge generated by incident radiation. The detection wafer is bump bonded to another wafer containing the readout electronics which extract the pixel values used to generate an image [8]. Bump bonding, also known as Flip Chip bonding, is a process where connections are made by solder spheres being deposited onto pads on one wafer, with the second wafer being flipped and aligned so that the spheres press onto pads on the second wafer to make a connection. MAPS incorporate some readout electronics within the pixel area, typically in a p-well region [5]. MAPS detectors are one of the most promising methods for utilising the potential benefits of digital detectors, while matching or exceeded the detection characteristics of photographic film and have been the focus of the recent advances with commercial cameras using a MAPS being released by FEI [9], Gatan [10] and Direct Electron [11]. This thesis therefore concentrates on MAPS detectors and describes how they can be used to improve performance.

1.2 Direct Electron Detection Technology

1.2.1 Hybrid Active Pixel Sensors

Hybrid Active Pixel detectors have been investigated as an direct detection technology primarily through the Medipix collaboration [12]. Medipix detectors have been used in a wide range of applications such as astronomy, high energy particle tracking and medical imaging. Faruqi [13] initially proposed the use of the Medipix detector for electrons but noted that technical issues relating to threshold value, counting rates, radiation hardness and spatial resolution would need to be addressed. Based on previous work with the Medipix detector for low energy X-rays [14] it was hypothesised that electrons with energies as low as 5.4keV can be detected with sufficient signal to noise. This is much lower than typical operating voltages used in TEM. Similarly it was noted that the counting rates required are well within the technical limits of the sensor. The effects of radiation on the detector are largely unknown, but the fact the readout electronics are protected should mean that the hardness is better than that of MAPS detectors. Finally Monte Carlo simulations suggested an improvement in spatial resolution of 2-3X over CCD detectors. Faruqi et al. [15] further explored the use of HAPS detectors for electron microscopy. The operating conditions for the detector are found to be a reverse bias of 40V and a threshold voltage of 1.3V for 120keV electrons. These conditions are determined by looking at average counts/pixel as a function of the reverse bias and threshold voltage. The Medipix detector operates in a counting mode, and hence the threshold voltage is the voltage that must be exceeded by a pixel in order to register an electron event which minimises detector noise. The linearity of the detector is shown to be excellent by plotting pixel count vs exposure time. Monte Carlo modelling of the detector showed that the FWHH (full width half height) distance over which the signal drops is a few microns and the signal reaches

1% within 30-40μm. The analysis presented lacks an MTF measurement but the initial modelling of spatial resolution predicts good performance. The MTF along with other detector parameters such as the NPS and the DQE referred to in this chapter are described in full in Chapter 2.

Faruqi et al. [16] subsequently evaluated the Medipix-2 detector which is similar to the Medipix-1 but with a much smaller pixel size, for use in electron microscopy. The Medipix detector is compared to film using an image of a raster of spots formed on both detection systems and showed that the Medipix detector is more sensitive. At low intensity the Medipix detector is able to detect each spot while on film the spots are not recorded. The MTF was measured using the image of an EM grid and the Medipix detector was found to have a MTF 76% of that of film at the Nyquist limit. However, this can be improved at the expense of the DQE or reduced to improve the DQE by altering the threshold voltage. Increasing the voltage means electrons which are scattered, generating signal away from the impact position are less likely to be detected, narrowing the PSF, and improving the MTF. However, some electrons are undetected, particularly those which impact close to a pixel boundary so that the signal is shared over multiple pixels and not detecting some electrons has a negative effect on DQE. A major issue with this measurement is that the MTF is expressed solely as a percentage of that of film, but no information about the type of film, microscope conditions and development process is given, all of which affect the MTF of film. In addition comparing the MTF only at the Nyquist frequency provides no information about the MTF at other frequencies.

McMullan et al. [3] used Monte Carlo simulations to model the number of pixels triggered as a function of the threshold voltage and the proportion of primary electrons which trigger single and multiple pixels (Figure 1.1). One question that arises from these results is the effective fill factor of the detector, as electrons are undetected when impacting close to pixel boundaries where charge is shared between multiple pixels causing no pixel to reach the threshold voltage. This implies that the probability of

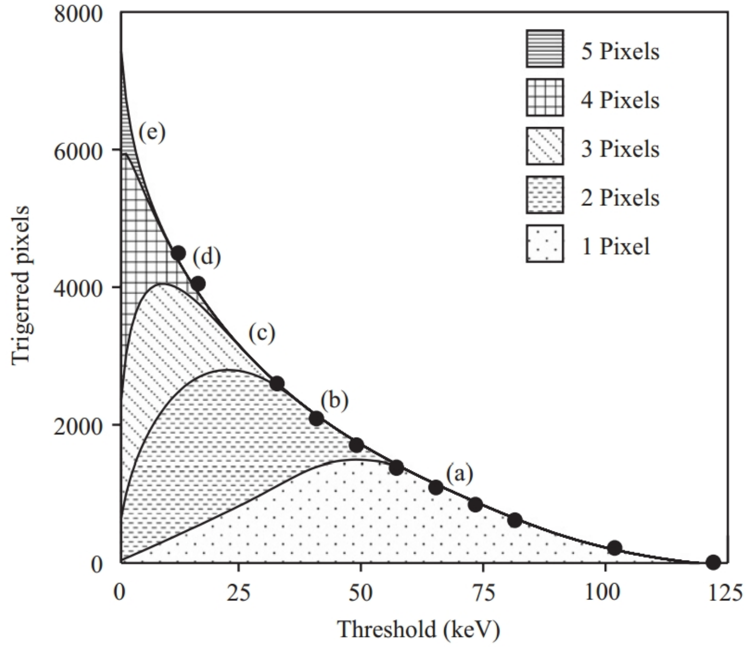

Figure 1.1: Monte Carlo simulations showing pixel counts as a function of threshold voltage and the proportion of the counts which come from events which trigger single or multiple pixels. Reproduced from [3].

detection is position dependent with a dead region between sensitive pixel areas. These problems are associated with the counting method used in the Medipix detector. The detector was developed as a technology for medical imaging and was designed for detecting photons. Photons deposit energy in a single absorption event so deposition is very localised, as opposed to electrons which deposit energy along a trajectory. For dedicated electron detectors more complex counting methods have been developed, including cluster imaging, which will be discussed in detail in Section 1.3.

McMullan et al. [3] also expand upon the previous results from Medipix-2. The effects of microscope voltage on the image quality are investigated with images showing a clear deterioration of image sharpness as microscope voltage is increased. Monte Carlo simulations show that as the energy increases electrons are scattered through a larger volume depositing energy in multiple pixels as shown in Figure 1.2.

Experimental measurement of the MTF using the edge method (as described later) confirms the results of the theoretical models for this sensor (Figure 1.3). Reducing the microscope voltage, and increasing the threshold voltage both have a positive effect on

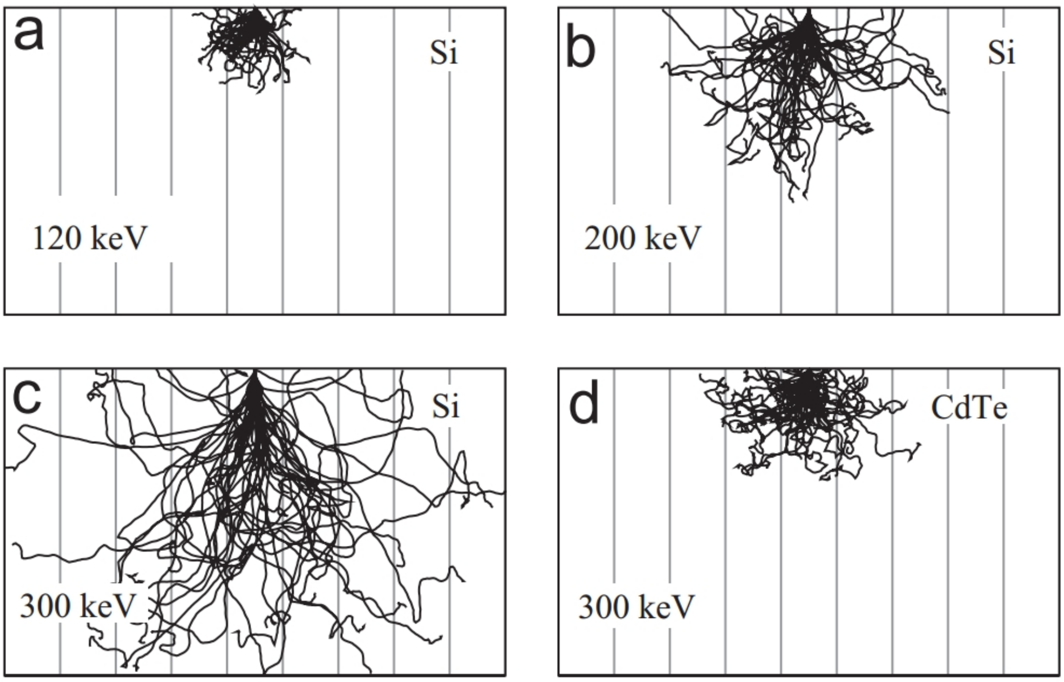

Figure 1.2: Monte Carlo simulations of electron trajectories in Si and CdTe over a range of energies. Reproduced from [3].

the MTF at the Nyquist frequency. It is also seen that at higher threshold voltages the MTF becomes limited by the effects pixelation as only electrons which impact close to the pixel centre are detected. The results from the DQE data also confirm the theoretical predictions. Radiation tests at a range of operating voltages show good radiation hardness up to 200keV, with no discernible damage after a dose of 4×10^8 electrons/pixel. However, rapid deterioration in performance was observed at 300keV with the detector becoming non-functional after a dose around 100kRad. An improvement to the detector is proposed, in which the Medipix-2 sensor reads out data sequentially, with a readout time of 120ms for an array of 516x516 pixels. Introduction of parallel readout of some columns will decrease the readout time, with speeds as fast as 1ms potentially achievable. Another modification to the detector which is desirable is the ability to “butt” individual sensors up to each other with no dead space between them, so larger areas can be imaged without decreasing magnification and resolution.

The work of McMullan presents a comprehensive analysis of the performance of

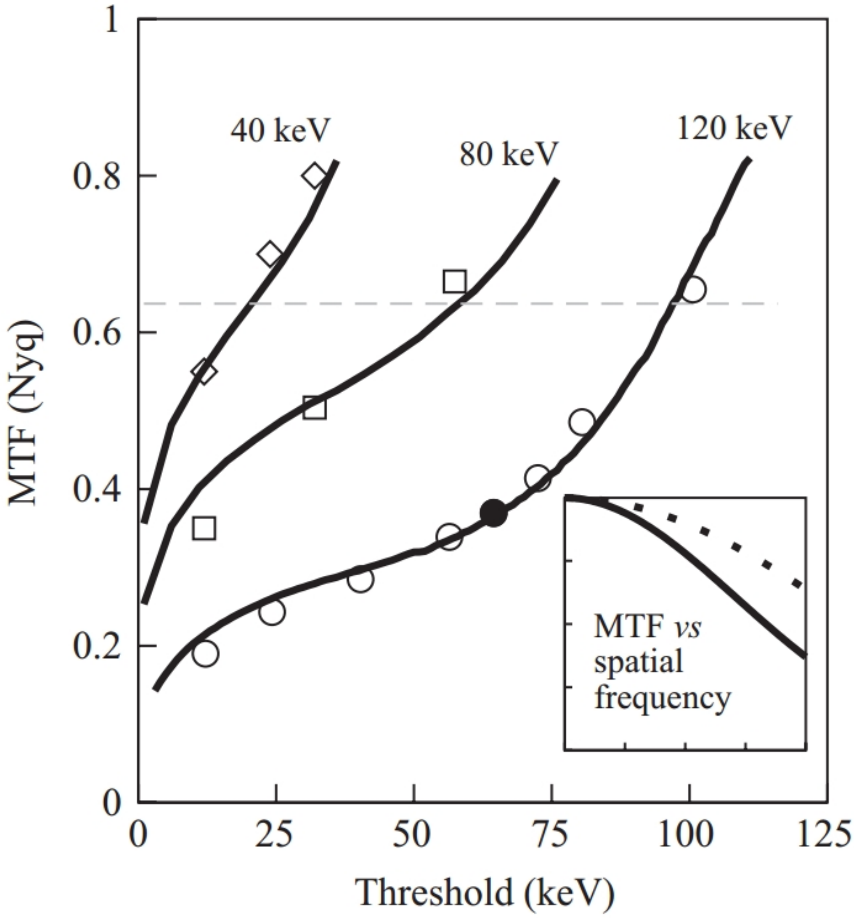

Figure 1.3: The effect of operating voltage and threshold voltage on MTF. Reproduced from [3].

the Medipix-2 sensor, where operating conditions for best performance are established. The limits of the detector are also considered and operation at low energy is required to prevent radiation damage. This latter limit is attributed to electrons which have sufficient energy to pass through the detector layer into the readout electronics which are sensitive to radiation damage. The precise mechanism which causes damage in the readout electronics is not established, but the most probable cause is charge trapping in the gate oxide of readout transistors which can cause them to fail. While damage to the readout electronics does seem the most probable cause of the rapid failure observed, above 260keV radiation damage can also take the form of an atom being displaced from its lattice site in Si. If the operating life was to be increased by improving the radiation hardness of the readout electronics, or the use of thicker sensors, further tests would be required to identify the effect of this latter mechanism on performance.

McMullan and Faruqi [17] reported images of a tobacco mosaic virus to investigate the performance of the Medipix-2 detector in low dose biological applications, where the high sensitivity enables images to be captured while minimising the radiation damage to the sample. Another advantage of this type of detector is the ability to build up an image by adding multiple frames, taking advantage of the fast readout. The position of each frame can also be adjusted to minimise the effects of sample movement between exposures. The biggest issue with this sensor is the large pixel size which arises from technical constraints in the bump bond required between the sensor and readout wafers and the poor performance of the detector at higher operating voltages due to scattering of electrons in the bulk of the sensor.

The problems highlighted by McMullan and Faruqi fundamentally limit the use of HAPS detectors. A proposed alteration is to use CdTe as the substrate for the detector layer, as the distance that electrons penetrate into this material is considerably less, so scattering is reduced. One practical issue is that the CdTe industry is much smaller than the Si CMOS industry and the technology is much less developed. The primary benefits of CdTe arise from the denser material leading to a smaller volume in which energy is deposited. However, this is not the only material parameter which will affect the detection properties. CdTe has a wider band gap, which implies that CdTe will be less sensitive as fewer electron hole pairs are generated for a given primary electron energy.

1.2.2 Double Sided Strip Detectors

A double sided strip detector (DSSD) is a form of counting detector that consists of a thin wafer where all pixels in a row on one side share a common contact, while all pixels in a column on the other side share a second common contact. When carriers are generated in a pixel signal is generated in a row and column allowing the identification of a seed pixel, which allows the electron to be counted [18].

Double sided strip detectors are most widely used in medical imaging using SPECT (single-photon emission computed tomography) where biological structures are imaged by injection of radioactive isotopes and the emitted gamma rays [19–21] are detected. Moldovan et al. [22] used Monte Carlo simulations to predict the performance of similar strip detectors for electron microscopy. The fundamental suitability of DSSD for EM is established as they can be scaled to provide the required field of view, have unlimited dynamic range and with fast readout technology the required frame rates can be achieved. The key requirement for DSSD is high efficiency, which requires that sufficient signal is generated to identify an electron, but that the energy deposited is sufficiently localised such that it only triggers detection in a single strip. The effects of the sensitive layer thickness, operating voltage and strip pitch are modelled to explore their effects on the overall efficiency. Figure 1.4 shows that the optimal detector thickness is *ca.* 50μm. Thinner detectors have poor efficiency due to the low energy deposited in the sensor, while thicker detectors have poor performance due to the large interaction volume, increasing the chance of triggering multiple pixels. Similarly increasing the strip pitch improves efficiency as a larger interaction volume is required to trigger multiple pixels. At higher primary electron energy efficiency is improved as more electrons pass straight through the detector without large angle scattering that increases the size of the interaction volume.

This paper sets a target of 80% efficiency and demonstrates this is quite hard to achieve, for operating voltages above 200kV.

Gontard et al. [23] have reported on an experimental implementation of a prototype DSSD for direct detection of electrons. The paper uses a commercially available sensor with 40x40 strips. However, the sensor thickness (1mm) is much thicker than the ideal thickness identified in the simulations. The readout electronics were designed by the authors such that the sensor could be operated as a TEM detector. This requires a high counting rate so that individual events can be identified. The results show that individual events can be identified at a rate of 1 electron every few μs. While this is a useful proof of concept, there are significant challenges that need to be overcome. In this DSSD, a pitch pitch of 1mm and device thickness of 1mm mean that the detector is too large for practical use as a TEM detector, where even a small, but usable array of 512 x 512 pixels would be 0.5m in width at the current device scale. A device with a 100μm strip pitch and a thickness of 50μm is suggested as an achievable target.

However, there are a number of concerns with the smaller version of this DSSD. Even with the large strip width investigated, cross coupling between neighbouring strips was observed. This effect is likely to worsen as the strips become smaller and closer. The signal to noise ratio is also a concern. The results quoted show that the pulse height associated with an electron is *ca.* 1.3V while electronic noise appears to have peaks at *ca.* 0.2V. For reduced thicknesses, the Monte Carlo calculations predicted a corresponding reduction in the sensitivity of the detector and it will be important to demonstrate that when the device is thinned electron events can reliably be distinguished from readout noise. The final area of concern is that the readout speed is still not sufficiently fast as the results show that individual events can be identified only on the order of 1 electron/μs. Due to the method by which positions are identified in the DSSD, only one electron can be counted in a given time interval giving rise to a

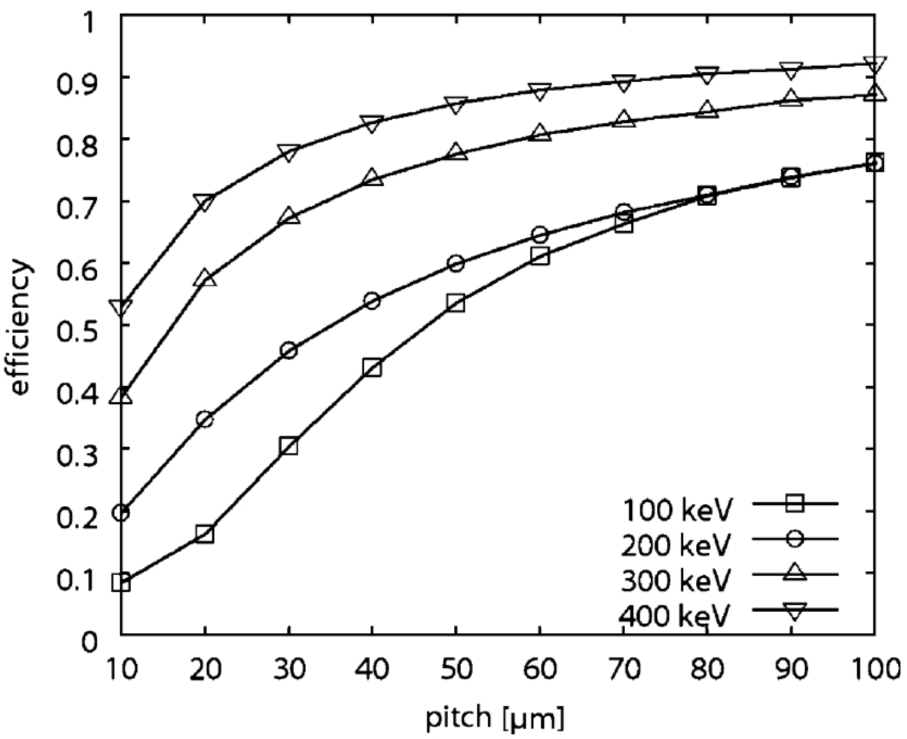

(a)

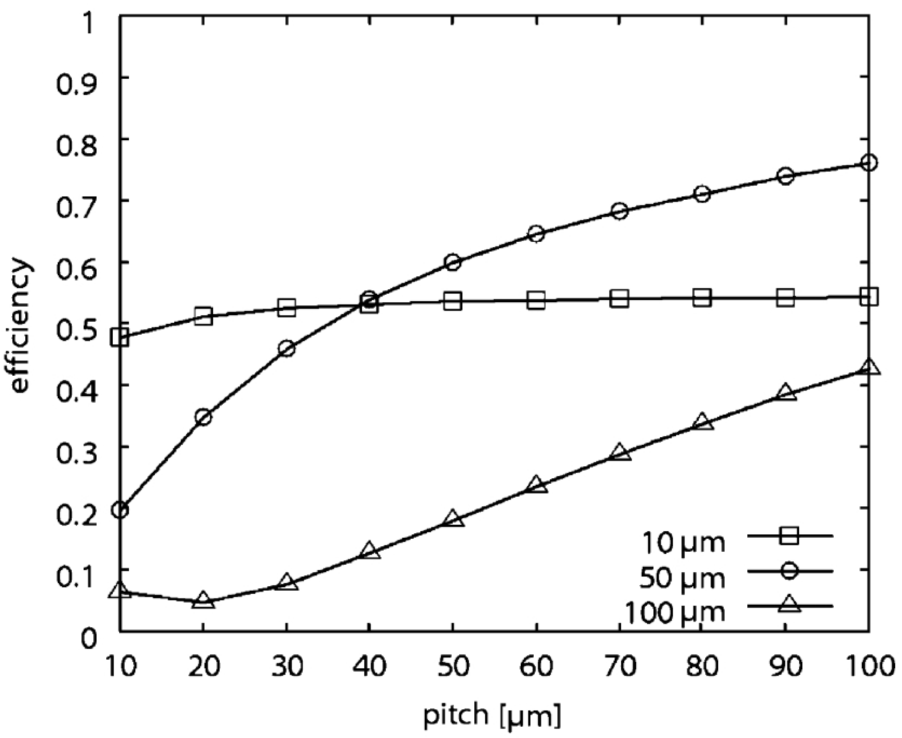

(b)

Figure 1.4: Monte Carlo calculations showing the effects of strip pitch and (a) operating voltage for a 50μm thick detector, (b) detector thickness at a operating voltage of 200kV, on efficiency for DSSD. Reproduced from [22].

dead time. At the quoted identification rate, for a 1s exposure of a 1024 x 1024 pixel image, the image would have an average dose of 1 electron/pixel. This is an extremely low dose and it would require a long exposure to acquire a reasonable signal to noise ratio. The solution would be to implement multi channel readout with each quadrant using a separate readout system.

DSSD sensors are in theory a very promising candidate detector for TEM if the current significant technical challenges can be overcome. However intermediate applications such as pixelated detectors for STEM [24] would be more suited to the DSSD architecture, as these require fewer pixels but conversely require very fast rates.

1.3 Monolithic Active Pixel Sensors

1.3.1 Introduction

As described in Section 1.1 monolithic active pixel sensors are CMOS sensors where the readout electronics are incorporated into the pixel design with the transistors required for readout located in the p-well region above the active layer [25]. A number of different types of readout exist including a three transistor (3T) pixel (1.5a), which has a transistor responsible for resetting the pixel, one to select a row of pixels for readout, and a readout transistor. The more complex four transistor (4T) pixel (1.5b) also includes a transfer transistor which is used in conjunction with a pinned photo-diode to improve charge transfer [26, 27]. As technology has developed more complex pixel designs have also been introduced with larger numbers of transistors [28].

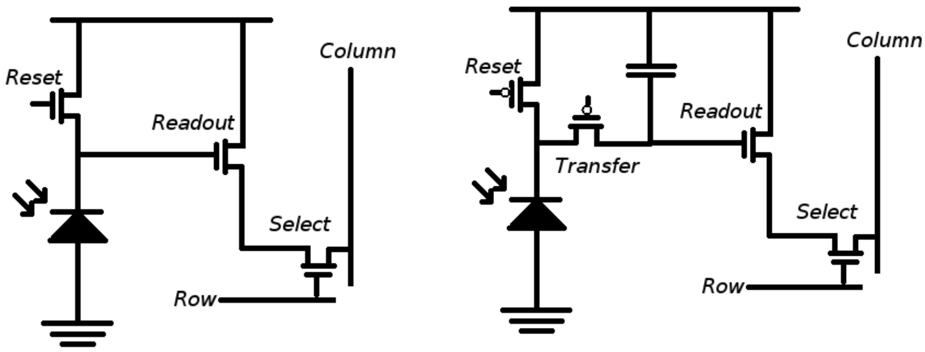

(a) (b)

Figure 1.5: Circuit diagram of (a) 3T pixel (b) 4T pixel, showing the Reset, Readout, Row Select and Transfer transistors.

1.3.2 Detector Imaging Modes

Detectors can be operated in a variety of modes. The integration mode is the most widely used and is also known as bright field since there is no requirement to distinguish individual events. In this mode the primary electrons create signal in a pixel and after a set integration time the total signal generated in the pixel is read out. The binary mode is one where the detector is operated at a rate where individual events can be identified. In each frame pixels which exceed a threshold value, for example four times the standard deviation of the dark image, are incremented in the final image. The counting mode identifies a seed pixel from the distribution of induced signal, incrementing a single pixel by one count.

The integration mode has advantages in that images can be collected more quickly than alternate modes, as each frame can represent a dose of many electrons/pixel. Hence, the signal limit is set by the amount of signal that can be generated in a pixel without saturation. In alternative modes while readout can be very fast, a large number of frames are required to achieve sufficient signal. Other methods require the dose in each frame be of the order of 1 electron/100 pixels so that individual electron events can be identified, meaning that a much larger number of frames is required for subsequent summation to give a total dose that provides sufficient signal to noise. The readout electronics of the integration mode are also much simpler as they do not require implementation of a counting algorithm. However, there are significant disadvantages related to detector performance. Moldovan et al. [29] compared simulated detectors operating in the different imaging modes. The integration mode was shown to have the worst MTF and DQE. This can be understood as the integration mode does not differentiate between induced current and dark current, making images noisier. In addition scattering in the sensor means that each incident electron generates signal in a cluster of pixels, which degrades the MTF. The binary mode differentiates between induced current and dark current, which reduces noise, but does not deal completely with the effects of scattering as a cluster of pixels will still be triggered by a single primary electron. The counting mode produces a dramatic improvement in the MTF by removing the effects of scattering by ignoring signal generated in pixels which are not the seed pixel, and by ensuring all electrons are recorded with equal weight. Further improvements to the MTF can be gained by suppressing large clusters in this mode, which represent primary electrons that have undergone large lateral scattering. However this method has a negative effect on the DQE due to the large number of clusters ignored. Thinning sensors will improve the DQE as this will reduce the number of large clusters.

McMullan et al. [30] have shown how electron counting can be achieved in practice. Data sets were collected where each image had a dose of 1 electron/500 pixels, such that there was only a very small chance of two clusters overlapping. For each cluster a seed pixel was identified, either by taking the pixel with the largest response, or the weighted centroid of the resulting signal. This seed pixel is advanced by one count in the image. An alternative method for implementing counting is to set a threshold value and normalise the remaining signal for each cluster such that each event contributes the same amount to the image. McMullan et al. [31] discuss more of the issues associated with cluster imaging. A significant issue arises from electrons which pass through the sensitive layer, forming one cluster, and are subsequently scattered by the

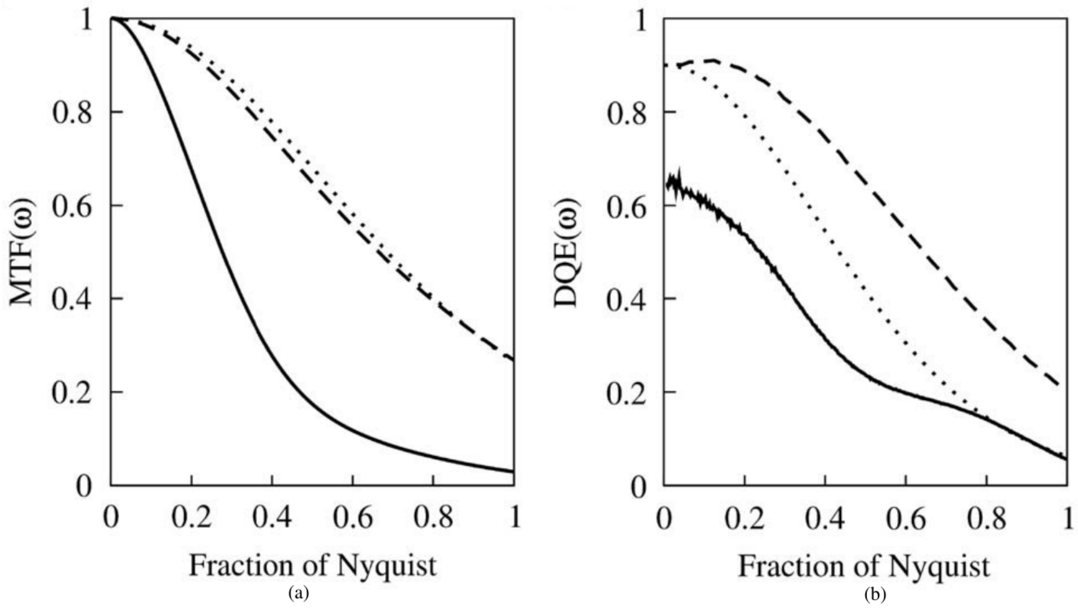

Figure 1.6: (a) MTF and (b) DQE of a detector operating in different readout modes. Integrating mode (—), normalised clusters (- - -) and peak position (· · ·). Reproduced from [30].

support back into the sensitive layer to produce a second cluster generating a false count. Thinning of sensors also reduces this problem by reducing the chance that an electron is scattered back into the sensitive layer.

Figure 1.6 shows that the counting method greatly improves the MTF, with both peak pixel and cluster normalisation producing very similar results. For the DQE assigning the event to the peak pixel results in an improved DQE at low spatial frequency, but at high frequency there is no improvement over the integration method. The reason for this is that assigning an event to a single pixel has a detrimental effect on high frequency noise. The normalisation method still suppresses high frequency noise but improves the MTF by suppressing the large clusters associated with large lateral scattering. While a counting mode offers clear improvements over the integration mode, the trade off in the acquisition and processing time is still an important practical factor and the paper states that operating in a counting mode generates 5000X more data than in an integrating mode.

Battaglia et al. [32] proposed a "centre of gravity" method to reconstruct the incident position of an electron from the resulting cluster and it was found that at 300keV the resolution can be reduced to 2.8μm for a pixel size of 9.5μm. This method of reconstruction leads to a much improved PSF, which translates into an improved MTF. However there are technical constraints to the implementation of this method which requires a frame rate of several hundred frames/second and the ability to reconstruct impact positions in real time. Importantly this method enables information to be recovered at spatial frequencies beyond the physical Nyquist frequency as sub pixel positional information is obtained. A prototype camera which employs sub-pixel resolution was presented by Mooney et al. [33] and a simpler implementation where each pixel is split into four sub-pixel units has been commercially introduced in the Gatan K2 Summit system released in 2012 [34].

Ultimately the choice of imaging mode is a balance of speed *vs.* performance and a major barrier to the widespread adoption of the counting mode is the readout speed of the detector. This is an issue not only for the efficiency of data collection, but can also introduce problems from sample drift if the acquisition time is too long. Decreasing the readout time by readout of pixel rows in parallel has made the counting mode feasible. Image processing software also needs to be optimised for dealing with the large amounts of data counting modes generate. Storing raw data is undesirable given that each image could require as much as 10Gb of data storage. However building up the final image during acquisition will improve throughput as raw data will not need to be written to a HDD, which is a time intensive process.

1.3.3 Performance of Monolithic Active Pixel Sensors

Faruqi et al. [6] have measured the performance of a 525x525 pixel MAPS detector, where the pixels are of the 3T type and contain four photo-diodes/pixel. The pixel size is 25μm and there is one analogue to digital converter per column so that each row is read out in parallel. The MTF of this detector was measured using images of an EM grid at low magnification and although the full MTF is not shown it is compared to the MTF of photographic film under the same conditions at the Nyquist frequency. The method used to measure the MTF was to take a Fourier Transform of an image of an EM grid. However, this is not optimal as it does not correct for dark current and pixel gain variations which can lead to inaccuracies. For 120keV electrons the MTF is at 50% of the value for film, while at 40keV, the MTF is over 75% of that achieved with film. This shows is that in this early design for a MAPS detector for TEM further improvements are required to make direct detection superior to film. While this comparison with film is useful, additional information about the film is required to make more quantitative comparisons, since different film emulsions perform differently. The restriction of analysis of the MTF to the Nyquist frequency is also limiting as in general information is required at a number of different spatial frequencies. The paper also lacks any analysis of the DQE, which is arguably the more important parameter of the detector as it takes into account noise.

McMullan et al. [2] have further characterised the MAPS detector developed by Faruqi by looking at the performance at 300keV. At this voltage it was found that the MAPS detector performs very well, exceeding the performance of film across most spatial frequencies. The DQE was also measured, where it was found that the MAPS detector generally has a performance worse than film, but is better than film very close to the Nyquist limit. These observations that the improvements to the MTF are greater than those to the DQE was attributed to the DQE being dependent on all electrons being detected with equal weight. However MAPS detectors have a relatively wide pulse height distribution, leading to a wide distribution in the detection weight which is particularly noticeable in the sharp drop in the MTF at low spatial frequencies. In turn this is attributed to electrons which are backscattered by support structures and re-enter the sensitive layer generating signal far away from the initial impact position. This conclusion is supported by Monte Carlo simulations, which compare backthinned detectors to thick detectors. A good match to the experimental data is shown for the thick detectors, while the results for thin detectors show much better performance and

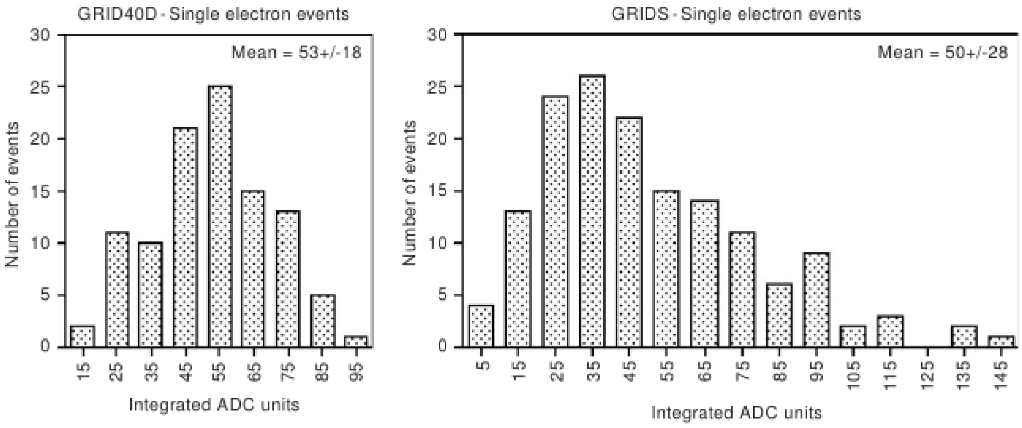

Figure 1.7: Pulse height distributions for 40keV and 120keV electrons. Reproduced from [6].

a particular improvement in the sharp drop in the MTF at low spatial frequencies. The results shown in this paper offer a more complete analysis of the performance of a MAPS detector including both MTF and DQE across the full spatial frequency range, but the DQE measurements all show high levels of noise particularly at low spatial frequency.

One detrimental effect to the MTF arises from scattering of electrons in the detector support [6]. The pulse height distribution is a histogram of the signal generated by each primary electron and can be found experimentally by producing the histogram of the integrated ADC count of all the clusters. Typical pulse height distributions for 40keV and 120keV electrons are shown in Figure 1.7. It can been seen from these plots that the histograms have a Landau distribution.

Milazzo et al. [5] reported on a detector with 128 by 128 pixels and a 20μm pixel size. The pixels on this detector all contain 4 diodes/pixel to improve charge collection efficiency and reduce pixel cross talk. The pulse height distribution measured for this detector also displays a Landau distribution. The explanation proposed for the tail is that it arises from incident electrons which are backscattered by the substrate into the sensitive layer. Experimental pulse height distributions showed electrons depositing up to 10$\times$ the energy into the sensitive layer of the detector compared to the average for a primary electron. This effect is problematic as it leads to generation of charge at greater distances from the incident position, widening the point spread function, which is detrimental to the MTF. It also implies that electrons are detected with different weight which affects the DQE. However, by thinning the sensor the contributions from backscattered electrons can be reduced.

Thinned detectors can be modelled using datasets acquired from a detector operating in electron counting mode by rejecting clusters which correspond to more than 10keV being deposited in the sensitive layer, indicative of contributions from backscattered electrons. This method produces images with no backscattered electrons, however even with thinning some electrons are expected to undergo scattering events that lead to them depositing much more energy in the sensitive layer than average. This approximation is therefore appropriate for examining the theoretical performance improvements for thin detectors at high energies, such as the situation described by Milazzo et al. [5] where a detector was modelled with a 30μm substrate at 300keV and it was found that signal from backscattered electrons contributed only 1% of the total signal.

Deptuch et al. [1] have evaluated the performance of the MIMOSA V chip as a direct sensor for electron microscopy. The MIMOSA range of sensors were previously developed for particle tracking applications [35] and the MIMOSA V version is a 1k by 1k pixel sensor, with a pixel size of 17μm and a 14μm thick active layer. The standard thickness of the substrate for this chip is 120μm, where the substrate thickness had been reduced by mechanical grinding and polishing. Two forms of the sensor were studied, the standard front illuminated chip and a back illuminated chip [36]. The back illuminated chip was produced by attaching a support wafer to the front of the chip and backthinning the original substrate. The advantage of this design is that the primary electrons go directly into the active layer rather than having to first pass through the CMOS electronics. This paper presents MTF plots acquired using the edge method (Figure 1.8). However, the MTF is poor, having dropped to 0 at the Nyquist frequency. The reason that this chip performs much worse than that described by Faruqi et al. [6] is due to much higher cross talk between pixels. The MIMOSA V chip has only one small charge collecting diode per pixel which means that a large proportion of the charge is collected in adjacent pixels to the pixel in which the charge is generated. Figure 1.8 shows two plots corresponding to the front side and back side illuminated chips. The back side illuminated chip performs slightly better as there is less scattering due to the absence of an electrically dead layer in front of the sensitive epitaxial layer. These improvements achieved by back illumination are interesting and could be incorporated into future detector designs. A notable omission is the lack of DQE measurements which is important as changing the position of the active layer relative to the electron trajectory will change the amount and spread of energy deposited, both of which will effect the DQE.

Jin et al. [37] have reported measurements of the MTF of a prototype direct detection device, where the key feature is a much smaller pixel size with the pixel pitch being 5μm. The MTF is calculated at 300keV and compared with the MTF of the MIMOSA V sensor [1]. Comparison of the MTF in units of 1/pixel, shows that the prototype performs better at low spatial frequencies, but performs worse at high spatial frequencies. However, comparison of the MTFs in units of (lp/mm) of the image on the detector, the new prototype greatly outperforms to MIMOSA V chip at the expense of field of view. The prototype performs badly on a 1/pixel scale (Figure 1.9), as the small pixel size means that the same scattering volume will produce signal in a larger cluster of pixels.

In principle, the same image can be formed on any detector with the same number of pixels regardless of the pixel size of the detector. To achieve this, the magnification needs to be selected such that each pixel samples the same area of the sample, which in turn means that a detector with larger pixels requires a larger microscope magnification. If the intermediate and projector lenses do not introduce image distortions at higher magnification, then the image on the detector is the same and in this case the larger pixel detector will produce a better image at high spatial frequencies as the MTF

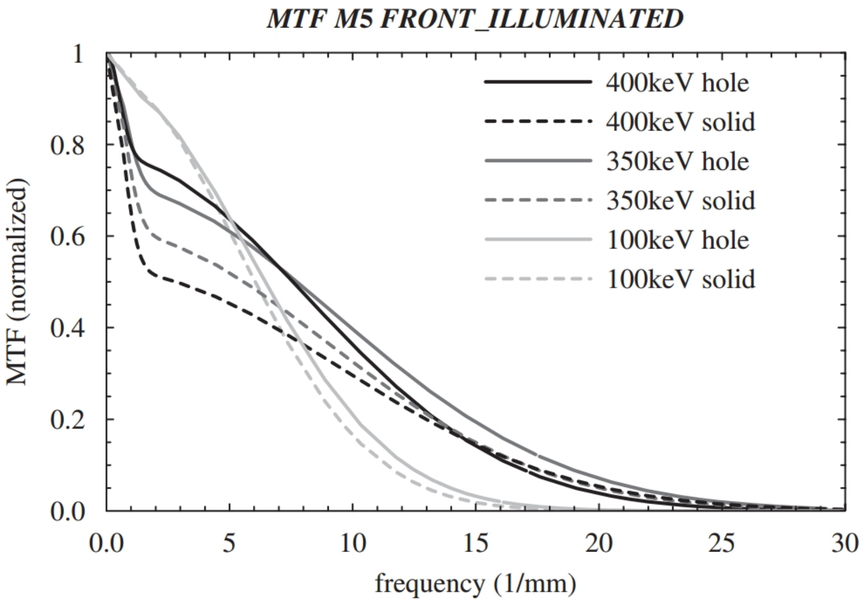

(a)

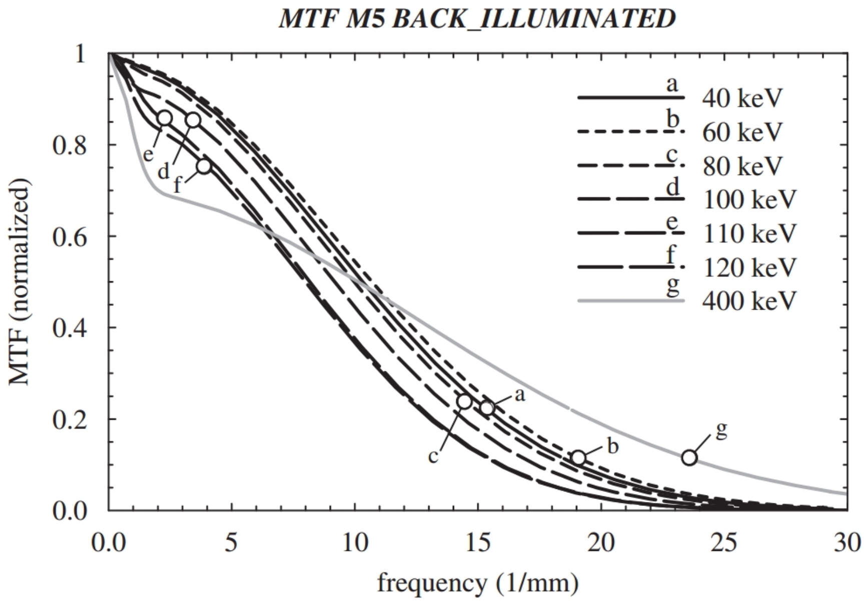

(b)

Figure 1.8: MTF of the MIMOSA V chip calculated using the edge method for (a) front side illumination. (b) back side illumination. Reproduced from [1].

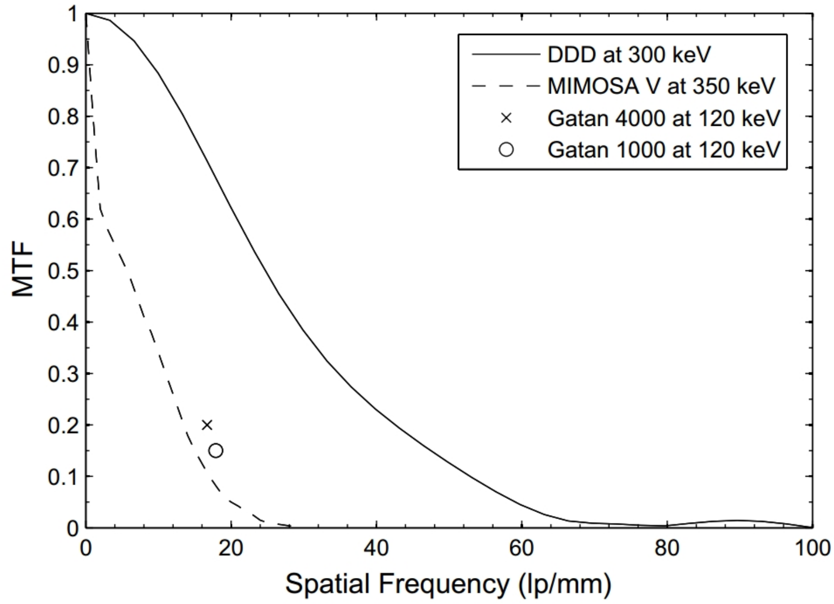

(a)

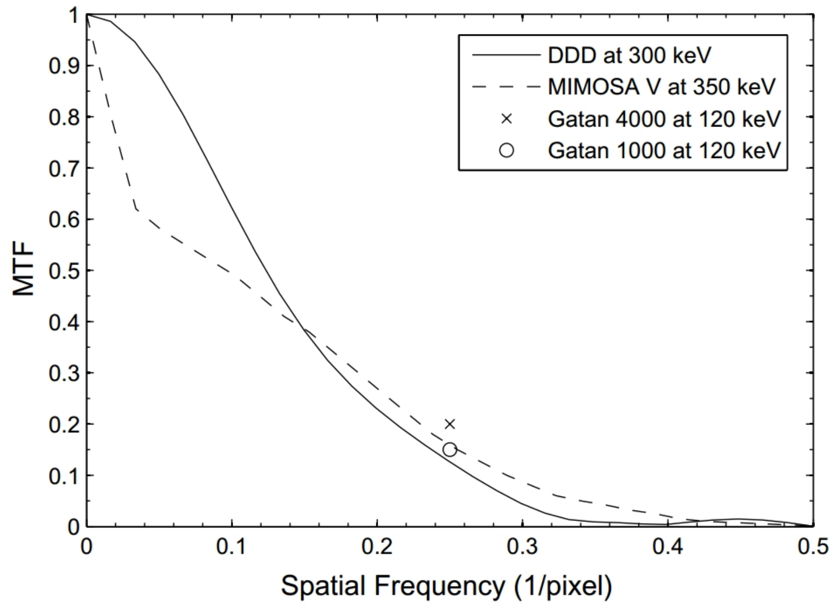

(b)

Figure 1.9: Comparison of two different detectors (a) using lp/mm scale (b) using 1/pix scale. Reproduced from [37].

is better. Typically electron optical distortions are <0.5% so are not a significant factor and therefore it is misleading to present data as if magnification is fixed when it would be natural for a user to adjust magnification so the region of interest fills the field of view.

Milazzo et al. [38] further characterise the detector produced by Jin et al. [37] and compare it to CCD cameras. The MTF and DQE of this detector is measured at 120keV and 200keV. The measured MTF at 200kV confirms the results of Jin et al. [37]. The measured MTF at 120kV enables direct comparisons with CCD data to be made, which show no improvement at low spatial frequencies while higher spatial frequencies show an improved MTF for the direct detector which can be attributed to the larger pixel size of the CCD and the use of a lp/mm scale making this improvement dependent on the considerations already discussed. DQE measurements suggest improved performance at high energy but as the paper notes there are alternative CCD cameras which have a similar DQE performance to the DDD. The reason for this discrepancy is that the detector used for the original comparison has a larger pixel size and so performs less well when the comparison is made in units of lp/mm. If a CCD camera had been selected with a smaller pixel size then the performance difference would disappear. At low energy the DQE of the CCD outperforms that of the DDD. However the comparisons that can be made are somewhat limited, as whilst the DQE performance of the DDD detector has been measured across the full spatial frequency range, that of the CCD comprises a single data point. There is no explanation given for the poor performance in the DQE at low energy however as the MTF results are very similar, the poor performance must arise from a worse NPS for the DDD detector.

Milazzo et al. [38] have also considered the dynamic range of the detector. It is found that the pixels exhibit a linear response up to 2380ADC for a conversion factor measured as 3.6 ADC to 1mV. This gives a dynamic range of 6.8dB after the reduction in dynamic range from dark signal has been accounted for, which is very limited. However, the readout time of the detector is much faster than that of a CCD, meaning that multiple images can be captured and summed to increase the dynamic range. If ten frames are captured then the overall frame rate is *ca.* 1Hz, which is comparable to that of a CCD, this method gives the direct detector a dynamic range of 68dB compared to 72dB for a CCD.

As discussed by Milazzo et al. [5] many theoretical models show that there should be an increased performance associated with thinning of MAPS detectors to greatly reduce the signal from backscattered electrons. McMullan et al. [39] show experimental results for the MTF of 35μm and 50μm thick backthinned sensors compared to an unthinned version. The resultant MTFs are reproduced in Figure 1.10 which illustrate that thinning of the detector and the removal of the associated backscattered signal leads to an improvement in the MTF, especially at low spatial frequencies where the sharp drop associated with backscattered electrons is removed or suppressed.

Battaglia et al. [40] have considered the use of direct detection in aberration corrected transition electron microscopy, using a detector thinned to 50μm with a pixel size of 9.5μm. Two variants of the detector were investigated; one is a 1Mpix detector and one is 4Mpix. The number of pixels is important, as more pixels imply a wider field of view for a given magnification, an important requirement for many applications. The detector was tested in two imaging modes and the method chosen to measure MTF used a Au wire to obtain a line spread function. However the wire was mounted parallel to the pixels, which is not optimal as parallel mounting of the wire can lead to aliasing artefacts since it is not possible to oversample the line profile by combining data from multiple rows as each row contains the same information. This may have lead to inaccuracies in the line profile acquired and the MTF curves presented.

Guerrini et al. [41] have described a camera that has specifically been designed as a commercial prototype utilising direct detection methods. The focus of this work is on overcoming barriers to commercial implementation of DDD. Specifically radiation hardness has been improved by the use of enclosed layout transistors which will be

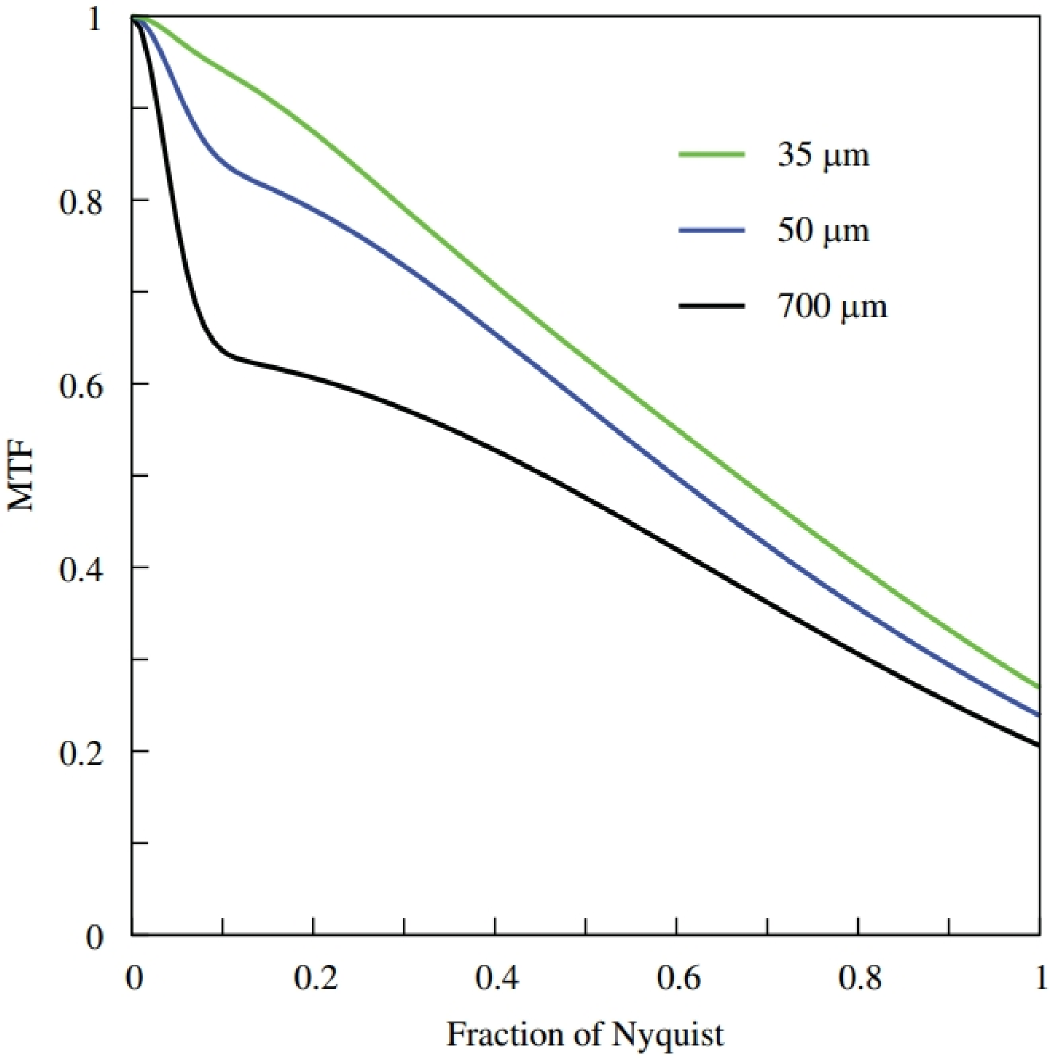

Figure 1.10: MTF of a MAPS detector at different thicknesses. Reproduced from [39].

discussed more fully in the next section. Improvements to readout speed have also been achieved through parallel readout of the pixels, which is required to maintain the frame rate while increasing the number of pixels to improve field of view. Characterisation of the detector is reported as a design specification rather than as experimental results. The detector performance is compared against a minimum specification proposed by the authors as a viability benchmark for a system, with the only criteria that is not met by the camera being readout noise. At 0.1 primary electrons/pixel, it is twice the value specified, but the detector otherwise meets the design specification.

Contarato et al. [42] report another prototype detector with a pixel size of 5μm and a better radiation tolerance while maintaining high readout. This sensor was thinned to 50μm and tested at 300keV, in both a bright field mode, counting mode and cluster imaging mode, where electron positions were obtained to sub-pixel resolution using a weighted centroid. The decreased pixel size has a detrimental effect on the dynamic range as the well depth is less than 1/4 of that found in detectors with a 10μm pixel size. This is not an issue for cluster imaging where the detector is operated far from the point of pixel saturation given the low dose per pixel required in this mode. For bright field imaging much larger numbers of frames must be summed to achieve the same dynamic range, greatly increasing the acquisition time. The choice of publishing the measured LSF rather than the MTF makes comparison with other work difficult, as the MTF is the Fourier transform of the LSF and hence the transform cannot be carried out without access to the raw data. A LSF of 1.5μm is sharp, but cannot be compared to other detectors using similar technology where only the MTF is reported.

Li et al. [43] have examined how dose rate effects the performance of the counting mode of the K2 detector. Since a key requirement of counting mode is that individual events can be identified, as the dose rate increases, the chance of a coincidence event is also increased. A coincidence event is one where more than one electron impacts the same region of the detector in the same readout cycle. In this situation the two electrons are counted as a single event, leading to a reduction in efficiency. The paper shows that as the dose rate increases there is a drop in efficiency as more electrons are not counted due to coincidence loss. Since the loss occurs when two electrons cannot be distinguished, the loss occurs more often in high intensity areas of the image. This is particularly important when measuring the MTF as the bright region is much more prone to coincidence loss than the region beneath the edge. It is shown that the NPS can be fitted to a function of the form $\mathrm{NPS} = a - b \quad mathrmsinc^2(fd)$ where a and d are constant with dose rate, and represent a noise level without coincidence effects and the distance in which two electron events cannot be distinguished respectively. The parameter b is dose rate dependent and increases with dose rate representing the larger influence of coincidence loss. Finally the parameter f is the spatial frequency. The sinc^2 dependence arises from the coincidence loss acting as a circular top hat mask with events outside the masking distance being detected normally whereas those inside are lost.

As this field has matured a number of commercial cameras have been brought to market that utilise direct detection. Four of these are characterised by Ruskin et al. [44], the Gatan K2 Summit, the Direct Electron DE-12 and the FEI Falcon I and Falcon II. This paper also tracks the developments that have been seen in this field, with the unthinned FEI camera performing worst, the integrating DE-12 camera performing better and the counting mode of the K2 showing the best performance both in terms of the MTF and the DQE.

McMullan et al. [45] have also compared the performance of commercial detectors. Three detectors, the Falcon II, the Gatan K2 Summit and the Direct Electron DE-20 were investigated at 300kV. The MTF behaviour of the Gatan K2 Summit is in agreement with the previously published results [44], however there is a more complete discussion of why the detector does not exhibit a DQE(0) of 1, proposing that increases in noise can arise from events which have long tracks causing problems for the counting algorithm and from readout noise triggering the counting algorithm to generate an event with equal weight to that of a primary electron. The integrating detectors are also shown to have improved DQE performance compared to film. The MTF of the DE-20 is shown to be much better than the Falcon II despite the smaller pixel size. This is attributed to a thicker sensitive layer so there is an increased effect from carrier diffusion between pixels. Carrier diffusion is random movement of carriers following a random walk as opposed to drift associated with the influence of an electric field, diffusion leads to lateral spreading of signal causing crosstalk between pixels. As the thicknesses of the sensors are unpublished, there may also be increased lateral scattering from a thicker detector. There are concerns about the accuracy of the Falcon II result; at high frequencies above *ca.* 3/4 of the Nyquist Frequency the Falcon II exhibits the best DQE despite having the worst MTF. This represents a three times increase in the performance compared to the detector at 200kV [44]. Given that the small MTF is being divided by a small NPS, any errors are going to be more noticeable.

MAPS detectors for direct electron detection have seen considerable development in the past decade, and three key features of CMOS MAPS detectors have made them a desirable choice for DDD. Firstly, MAPS detectors can be thinned, unlike CCD and HAPS devices where the necessity for a thick scintillator or additional readout electronics increases the device thickness. Thick detectors lead to backscattering of electrons to the detriment of the point spread function and thin MAPS detectors greatly reduce this backscattered signal. MAPS detectors can also be operated in counting mode due to the high sensitivity and fast readout that can be achieved and this mode of operation results in much better detector performance than the traditional integration mode.

1.3.4 Radiation Hardness of Detectors

The radiation hardness of detectors is important as equipment must have a satisfactory operational lifetime. The low radiation hardness of the first CMOS detectors has been a barrier to their widespread commercial introduction, but recently significant progress has been made in improving the radiation hardness of these devices. This section discusses the various investigations of radiation hardness in a number of different sensors and Table 1.1 at the end of this section summarises these findings.

There are two units commonly used to describe the dose on a detector. The first is electrons/pixel which is a useful unit which is easily interpreted. However, when discussing the effect of radiation damage in terms of dose in electrons/pixel, an energy must be specified as the same number of electrons at high energy will cause significantly more damage. The traditional unit for describing radiation dose is Rads, where 1 Rad is defined as 0.01 Joules of energy deposited in 1 Kg of material (1Rad=0.01J/kg). The energy of the electrons is again important as different damage mechanisms become significant at different energies. Ionisation damage which causes excess positive charge requires less energy than displacement damage, in which an atom is displaced from its lattice site [46]. Faruqi et al. [47] have described a method for converting from electrons/pixel into Rads. Firstly the dose is divided by the pixel area to yield the dose in electrons/μm^2. Secondly the penetration depth of the electrons at a specific energy is used to obtain a value for the energy deposited/μm/electron. Multiplying these two values gives the energy deposited/unit volume, from which the dose in Rad can be obtained if the density is known. This method can be described mathematically in equation 1.1.

$$Dose(Rad) = Dose(e/pix) \times 0.01 \frac{E\rho}{AP} \tag{1.1}$$

Where E is the electron energy in joules, A the pixel area and P the penetration depth. For thin detectors where many electrons pass through the detector, a more detailed analysis is required as not all of the electron energy is deposited. In this case a Monte Carlo simulation can provide a pulse height distribution which gives the average energy deposited by an electron in a detector.

Faruqi et al. [6] have examined the radiation hardness of their detectors by looking at the pedestal level after exposure of the detector to a known dose. The pedestal value is the required count that is subtracted from a pixel to correct for dark current and is found by taking images at the same exposure time but with no incident beam. Images were taken at doses of 10,000, 250,000 and 600,000-900,000 electrons/pixel using 120keV electrons. When exposing the detectors an EM grid was imaged so that there were some pixels which remained relatively undamaged. After a dose of 10,000 electrons/pixel, a shadow of the EM grid could be seen in the dark images as the pedestal level rose in irradiated pixels and for a dose of 250,000 electrons/pixel the sensor was still usable but become unusable between a dose of 600,000 - 900,000 electrons/pixel, however the authors are not clear about what they mean by usable. Faruqi estimates that this equates to a radiation dose of 10,000-15,000 rad. This indicates very low radiation hardness, which will need to be improved to make this a feasible detection device for general use. However this result establishes a useful benchmark for the range of radiation dose that a device can sustain and still be usable. The primary source of damage seems to be an increase in leakage current as illustrated by the shadowing observed, but no mechanisms for damage are suggested. Deptuch et al. [1] have reported the radiation hardness of the MIMOSA V sensor. An increase in the pedestal value of 1.8ADC units after an approximate dose of 25,000 electrons/pixel was observed. However a more quantitative measure of damage is required to draw meaningful conclusions, specifically measurements of the effect of radiation damage on the dynamic range, the MTF and the DQE are desirable.

McMullan et al. [30] have described another manifestation of radiation damage as "hot" pixels, which are pixels with a high value in the absence of any electron events. Hot pixels are particularly important when operating a detector in counting mode, as they generate false positives when detecting incident electrons. They can however, be distinguished from true events as they only effect a single pixel, whereas a true event generates signal in a small cluster. They also appear in the same position in successive frames, while true events have a low probability of occurring in the same position in multiple sequential frames. These hot pixels arise from the reset transistors in the pixels not functioning properly, so a pixel retains charge between frames. The observation of an increasing leakage current and associated pedestal value is identified as a consequence of radiation damage, but it is relatively easy to correct this effect so the detectors ability to capture an image is not addressed. The increase in leakage current affects detector performance as it reduces the dynamic range as more of the pixel capacitance is filled by dark current. There is no consideration of other radiation effects induced on detector performance. However, radiation appears to have an effect on the readout electronics so it seems plausible that this may also affect readout noise, which would effect both the NPS and DQE.

Battaglia et al. [48] detail the development of detectors with pixels designed to be radiation hardened. The mechanism believed to be responsible for radiation damage is the generation of trapped charge in the oxide layers. This trapped charge generates an electric field which can invert the silicon in contact with the oxide, i.e. change the type of majority carrier. This effect is the same as that which occurs when a voltage is applied to the gate, so when this damage occurs in the gate oxide it can cause an increase in the leakage current of the transistor. To overcome this form of radiation damage pixels have been designed with an enclosed gate layout. In addition a different diode design was implemented in different areas of the sensor, with implanted p^+ guard rings, a thin oxide layer over the entire diode and a polysilicon ring covering potentially inverted regions all being investigated.

The enclosed layout transistor is also known as the endless transistor, and is a transistor geometry designed to be radiation hardened. In this geometry the gate region is fabricated as a ring around either the source or drain. The shape of the gate is a generally a square with bevelled corners, as shown in Figure 1.11. The overall behaviour of this type of transistor can be found by treating the structure as multiple transistors connected in parallel, with the different types of transistor corresponding to the three different regions marked on Figure 1.11 [49].

The enclosed gate layout has been investigated as a means of improving radiation hardness for CMOS detectors by Eid et al. [50]. The method used to describe the

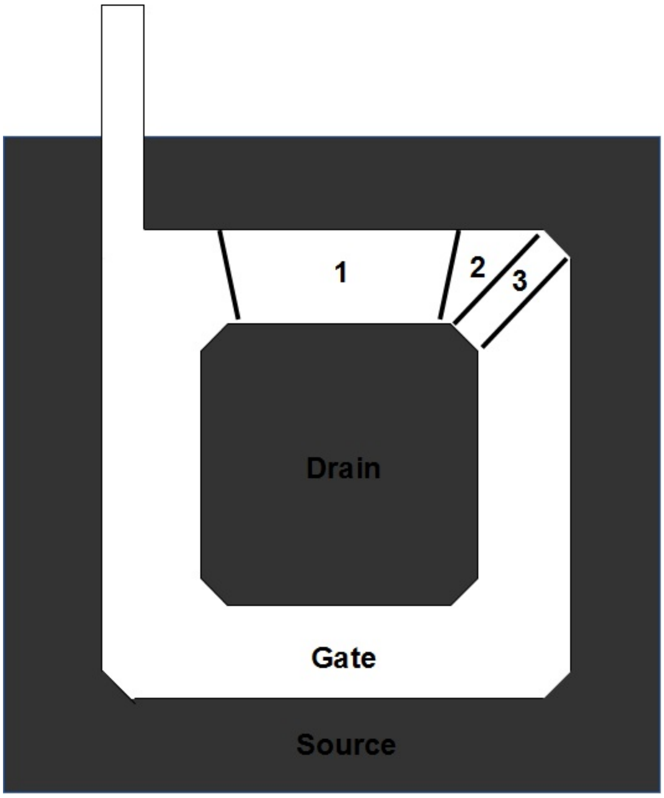

Figure 1.11: Geometry of the ELT showing the three different region types treated as separate transistors connected in parallel for the purpose of calculating the overall behaviour of the transistor. Redrawn from [49].

effects of radiation damage is to express the dark current as a percentage of the saturation current. Four different pixel designs were tested but the results showed that the most important factor for radiation hardness is the size and shape of the photodiode and the presence of a *n* well. It was also shown that the pixels with large photodiodes retain more of the dynamic range. However smaller photodiode pixels have less dynamic range initially, due to the smaller well capacitance, implying that even though the leakage current increase is less for smaller photodiodes, the proportion of the dynamic range lost is greater. A thin gate oxide also has a beneficial effect on radiation hardness, as with a thin oxide it is possible for the trapped carriers responsible for the charge to tunnel out of the oxide, which leads to a form of recovery [50].

The use of an enclosed transistor geometry is not without issue as the footprint of the transistor in this geometry is much larger; typically the fabrication of transistors in this geometry required pixels to be twice as large compared to those fabricated with a traditional MOSFET geometry [51]. Eid et al. [50] show a substantial improvement in radiation hardness with a significant proportion of the dynamic range being retained at doses as high as 30MRad. However this paper is a discussion of a general use of a MAPS detector and the radiation used is gamma radiation rather than electrons. More specifically the gamma rays used come from the decay of Co-30, which generates gamma rays with energies of the order of 1MeV. This radiation is of a much higher energy, is highly penetrating and is deposited in a different way to keV electrons and therefore investigations into the improvement in radiation hardness for fast electrons are still required.

The radiation hardness of MAPS detectors with ELT transistors has also been investigated by Battaglia et al. [48] for the LDRD2-RH prototype chip. The chip was irradiated using 200keV electrons and 29 MeV protons up to a dose of 1MRad. A Gold mesh was used to protect areas during electron irradiation for comparison of irradiated and undamaged regions. The results from this work showed that use of the enclosed transistor layout greatly improves the radiation hardness. However, the pixels are still sensitive to radiation with leakage current increasing with dose but to a lesser extent than pixels not using the enclosed transistor layout, as the sensors were still usable at the maximum dose tested. Improvements were also seen in pixel noise. ELT pixels showed little variation in pixel noise with dose while the soft pixels had a strong dose dependence. When irradiated with 29MeV protons the sensors was more susceptible to radiation effects. The reason for this appears to be when irradiated by electrons the radiation damage is limited to ionisation, whereas the larger energy of the protons is sufficient to cause displacement damage. The energy required to cause displacement of atoms in Si is 260keV which means that when operating at high energy the detector is susceptible to additional damage. Further development of radiation hard detectors is presented in Battaglia et al. [40], where sensors were irradiated at a dose of 5MRad. The effects of radiation were again noticeable and it was found that the dynamic range was reduced by 30% and single pixel noise increased by 25%. However the detector was still operational at this level of damage. The success of the enclosed gate layout for radiation hardened pixels has been confirmed by Guerrini et al. [41] where detectors operated to a dose of up to 300 million electrons/pixel were shown to be still operational. However, the increase in single pixel noise raise questions about how radiation effects the NPS as any increase in single pixel noise would suggest a detrimental effect on the NPS which in turn leads to a worse DQE.

An alternative method for analysing radiation damage has been reported by Faruqi et al. [47], where an EM grid was imaged before and after irradiation and the level of contrast between bright and dark regions was compared. They observed that at a radiation dose of 0.2MRad contrast was reduced to 85% and further reduced to 82% at 1MRad. The effects of annealing were also investigated in which the sensor was irradiated to 0.2MRad then left for a month at room temperature and the contrast remeasured. After annealing the sensor shows some recovery of contrast, with the residual contrast returning to 87%. Annealing at above room temperature may improve the level of recovery further but could also affect the CMOS devices. Overall, measuring residual contrast is a useful measure of damage as it allows the differentiation of lifetimes of the detector for different applications. For structures with high contrast, lower residual contrast can be tolerated, whereas in low contrast imaging any reduction in contrast is a much more significant problem.

Contarato et al. [42] have shown that radiation hardness is also improved by a decrease in pixel size. Using the same pixel design as Battaglia et al. [48] but using a 0.18μm CMOS process, reducing pixel size from 9.5μm to 5μm, the leakage current at a dose of 80MRad is $\sim 4\times$ lower than for the larger pixels. An increase in pixel noise up to *ca.* 100 e^- was also observed.

Moody and Gubbens [52] have a patent for an alternative method for improving radiation hardness. The patent revolves around a simplification of the pixel structure, by removing the buffering amplifier from the pixel, turning it from an active to a passive pixel. In this way the radiation tolerance should be greatly increased at the expense of noise and readout speed, although the performance can be improved by multi-pixel shared buffer amplifiers. The patent also describes the use of a shutter so that the detector is only exposed when recording an image helping to minimise unnecessary exposure. The patent has no quantitative data about the radiation tolerance and the negative impact in performance from this change. However this method has the potential to be useful for higher dose work if the detector still outperforms a CCD.

The radiation hardness of direct detection device presents a challenge for the technology to overcome before widespread adoption as detectors in electron microscopy. The introduction of the enclosed transistor layout has resulted in a step change in the radiation hardness of detectors, taking the operational lifetime from a few 10's of kRad to 100MRad. However the performance of the detector is still radiation dose dependent, as the dynamic range decreases with the lifetime of the detector and hence increasing radiation hardness further is still beneficial. The level of radiation hardness that has been achieved means that many images can be collected in low dose applications before damage becomes unmanageable. The radiation hardness however is still not yet at the level where a DDD could offer an alternative for imaging high intensity diffraction patterns, where the entire electron dose is concentrated is a small number of pixels. The effects of radiation damage on the NPS and DQE have also not been investigated despite initial results that show an increase in pixel noise [40–42].

Name	Description	Method	Findings	Reference
Unnamed sensor	525x525 3T pixels with a pitch of 25μm, with 4 diodes/pixel.	Irradiated with 120keV electron from 10,000 to 900,000 electrons/pixel.	Usable after 250,000 electrons/pixel. Failure between 600,000 and 900,000 electrons/pixel, corresponding to 10-15 kRad.	[6]
MIMOSA V	17μm pixel size 1kx1k pixels detector.	Irradiation 25,000 electrons/pixel.	Increase of 1.8 ADC units to the pedestal level.	[1]
MI3 "Vanilla"	520x520 3T pixels with a pitch of 25μm.	Characterisation of the detector at 120kV.	Observation of "hot" pixels, increase in leakage current.	[30]
Unnamed sensor	Designed to be radiation hard, with thin oxide and enclosed layout transistors.	Irradiated with gamma rays from a Co-30 source up to a dose of 30MRad.	A significant proportion of the dynamic range retained.	[50]
LDRD2-RH	20μm pixels fabricated with ELT and guard rings to improve radiation hardness.	Irradiated with 200kV electrons and 29MeV protons using a gold mesh to mask parts of the sensor.	An increase in leakage current was observed but the detector was still usable.	[48]
TEAM1K	1024x1024 9.5μm radiation hard pixels.	Sensor irradiated to a dose of 5 MRad with 300kV electrons.	Dynamic range reduced by 30%, single pixel noise increased by 25%.	[40]
Falcon	*ca.* 4000x4000 pixels with a pitch of 14μm.	Irradiated to 300 million electrons/pixel.	Detector was still functional.	[41]
STAR250	512x512 pixels with a 25μm pitch, each pixel has four charge collection diodes.	Comparing contrast of an EM grid before and after irradiation to 0.2MRad, 0.2MRad annealed at room temperature for a month and 1MRad.	85% residual contrast at 0.2MRad, 87% after annealing and 82% after 1MRad of radiation.	[47]
Unnamed sensor	As the LDRD2-RH but scaled to a 5μm pixel size.	Irradiated to 100MRad with 300keV electrons.	At 80MRad the leakage current was 4x smaller for the smaller pixel size, the detector was usable at 100MRad.	[42]

Table 1.1: A summary of the investigations into the radiation hardness of detectors for direct electron detection.

1.3.5 Applications of DDD

Two of the most attractive properties of direct detectors are high sensitivity and gain, making them ideal for applications where the sample is dose sensitive, as is often the case with biological samples. Jin et al. [37] have imaged muscle tissue in a TEM with a DDD. In this work the small field of view was addressed by forming an image as a mosaic, stitching together images to build up a bigger picture.

Milazzo et al. [53] have evaluated the use of a direct detector in cryo-electron microscopy. Cryo-EM is a technique often used in biological studies to maximise the radiation resistance of samples by embedding them in vitreous ice. They initially show that the DDD performs better than a CCD camera using Fourier Transforms that show an improved response at higher spatial frequencies. Measurement of the MTF using the edge method also shows an improved performance of the DDD. A common technique used in cryo-electron microscopy is the 3D reconstruction of proteins. The improved resolution of a DDD over a CCD means that a level of resolution can be achieved in 3D reconstruction that was previously unattainable. Reconstruction of the GroEL protein was carried out using both a CCD and DDD. The DDD produces a higher resolution reconstruction and it is noted that resolution achieved in previous reports [54, 55] was observed, despite the fact the specimen and the detector were not optimised.

Further experimentation into using the DDD for cryo-EM is presented by Bammes et al. [56]. Using images of graphite and amorphous carbon films, it is shown that the signal to noise ratio at the Nyquist limit is sufficiently high to extract information, with a signal to noise ratio 5X that observed for a CCD detector. The performance of this detector for Cryo-EM was measured through the detector's performance in a reconstruction of the $\varepsilon 15$ bacteriophage. The sum of the Fourier Transforms of 55 particles in a single frame showed signal transfer was sufficiently strong that information up to 4/5 of the Nyquist Frequency could be used in the reconstruction and similar results were achieved for the P22 procapsid.

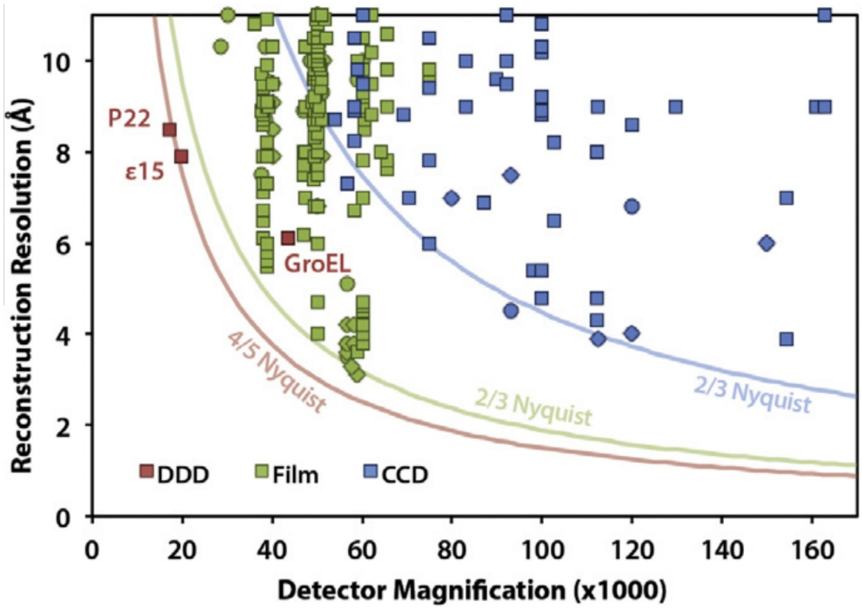

Figure 1.12: Summary of the resolution achieved in single particle reconstructions in cryo-EM from DDD (red), CCD (blue) and photographic film (green) datasets. Reproduced from [56].

Figure 1.12 shows the theoretical resolution if the limiting effects of the detector are independent of the detector magnification. These results suggest that the DDD provides the highest resolution for a given detector plane magnification, exceeding the levels that film can achieve. While it is clear that the theoretical resolution limit has been reached at low magnifications, it has yet to be seen if the performance can be replicated at higher magnification and resolution. Bammes et al. [56] also raise the question as to whether the fast readout of the DDD can be utilised to improve resolution. From Figure 1.12 it is clear that increasing magnification increases resolution. However for film recording magnifications above 60,000x are rarely used because of the number of particles required for a reconstruction, typically 7,500 - 20,000. At higher magnifications fewer particles per frame are recorded, and so more frames are required, with consequently more data to store and process. This is a limiting factor for film where every image taken needs to be developed and digitised before it can be used in a reconstruction. In contrast, the workload for processing data recorded electronically is much smaller making it viable to use at higher magnification.

Finally Brilot et al. [57] have used a direct electron detector to investigate beam induced motion of samples in cryo-EM. The detector was used to make a "movie" of a carbon film with holes, initially captured at 40 frames/s, with 10 frames added to achieve sufficient contrast for analysis, producing a film at 4 frames/s. Using the detector in this way allows the rotation between frames to be measured. Movement of the sample is shown to be due to damage from the beam and motion is a drum like rotation. This rotation means that different points in the sample move at different speeds, corresponding to the distance of the point from the rotation axis. A new technique is also suggested, which is only made possible by use of a direct detector in which by taking a series of frames the motion of sample can be determined. Once the motion is determined it is possible to form a final image of a particle by undoing the transformations and rotations measured and averaging the frames, preserving the high resolution signal. This method greatly reduces the blurring in the final image arising from the motion of the sample during the exposure.

Direct detection of electrons has been shown to have very high efficiency, making high resolution low dose imaging possible. This capability makes direct electron detectors a natural choice for use in cryo-EM, where the use of direct detectors has improved the resolution limits of single particle reconstruction and is quickly becoming a standard tool in cryo-EM.

Chapter 2

Theory

2.1 Introduction

The process of designing, fabricating and testing an experimental detector is a long and expensive process, therefore it is a useful exercise to be able to simulate detectors to inform subsequent design choices. Moldovan et al. [8] have used a Monte Carlo simulation based on earlier work [58] to calculate the theoretical MTF for different types of detector. The MTF together with other detection parameters are described more fully in Section 2.3. Three different detectors were modelled in this manner, with each detector having a 20μm sensitive layer and a pixel size of 20μm. The three detectors modelled were a monolithic active pixel sensor, a hybrid active pixel sensor and a double sided strip detector (DSSD).

The simulation uses Joy's model of straight trajectories between Rutherford scattering events. Inelastic scattering is assumed along the trajectories, with the energy lost continuously along the length, at a rate calculated from the Bethe stopping power. Any deviations to the trajectory due to inelastic scattering are ignored, as these deviations are small. However, carrier diffusion is not accounted for so the MTF will be better than that achieved in practice. It is commented on that as the detectors are thin, so there is only limited diffusion during charge collection, but omitting it will introduce errors at high spatial frequency where the effects of carrier diffusion are most noticeable.

The results of these calculations are shown in Figure 2.1. This shows that all the direct detection methods perform much better than the CCD, the DSSD has the best MTF, close to the theoretical limit, while the MAPS detector also performs well with a MTF of 0.35 at the Nyquist limit. The HAPS performs slightly worse than the CCD at low spatial frequency, however at higher spatial frequencies it outperforms the CCD. The DSSD has nearly ideal performance, as the counting method used means that each electron is associated with a single pixel which prevents an electron contributing to the pixel count of any pixel away from the seed pixel, reducing the width of the PSF.

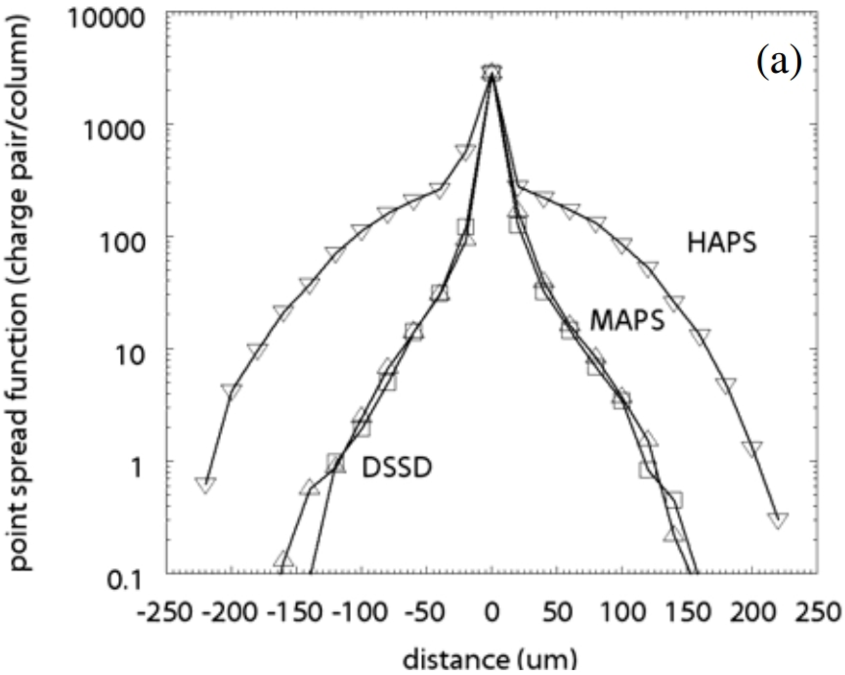

(a)

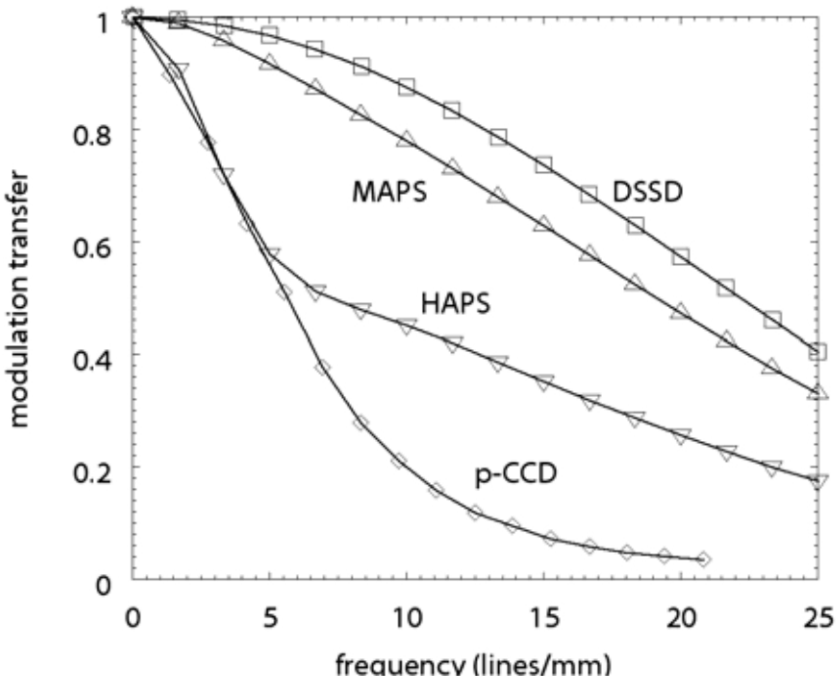

(b)

Figure 2.1: (a) Point spread function and (b) Modulation Transfer Function of modelled direct detectors compared to experimental data from a CCD. Reproduced from [8].

2.2 Electron Scattering Theory for Detector Simulation

Chapter 3 presents simulated data generated for various detectors. This section describes the fundamental models on which these simulations are based. The programme used for simulating detectors was developed by Meyer [59]. The basis of this programme is a Monte Carlo model for electron scattering initially proposed by Joy [60]. In this model the electron trajectories are modelled as continuous energy loss along straight trajectories due to inelastic scattering events described by Bethe [61, 62] between discrete elastic Rutherford scattering events [63] which lead to a change in direction. In Meyer's code, a number of modifications to Joy's model were made to improve accuracy. These modifications are; relativistic corrections to Rutherford's original formula for elastic scattering, the use of the relativistic Bethe formula to describe inelastic scattering, and the effects due to the generation of fast secondary electrons.

The distance between elastic scattering events is based on equation 2.1;

$$l = -\lambda \ln(R) \tag{2.1}$$

Where l, is the distance between events, λ, is the mean free path and R, is a random number between 0 and 1 to model the stochastic nature of the scattering process. The mean free path is found using equation 2.2, where A, is the atomic mass, N_a, is Avogadro's number, ρ, is the density of the material, M_u, is the molar mass constant, 0.001kg/mol and σ, is the total scattering cross section.

$$\lambda = \frac{AM_u}{N_a \rho \sigma} \tag{2.2}$$

The scattering cross section of a material describes the area in which an electron is scattered and for an isolated nucleus this area would be infinite as scattering is due to a coulomb interaction which has infinite range. However orbital electrons screen the nucleus giving a finite cross section. The Rutherford cross section corrected for relativistic effects used in the simulation for elastic scattering is given by equation 2.3 [59,64].

$$\frac{d\sigma_{el}}{d\Omega} = \left(\frac{Ze^2}{8\pi\varepsilon_0 E}\right)^2 \left(\frac{E+E_0}{E+2E_0}\right)^2 \frac{1}{(\sin^2(\theta/2)+\alpha_s)^2} \quad (\mathrm{m}^2) \tag{2.3}$$

Where σ_{el}, is the elastic scattering cross section, Z, is the atomic number of the scattering atom, e, is the electronic charge, E, is the kinetic energy accounting for relativistic effects, ε_0, is the permittivity of free space, $E_0 = m_0c^2$, the rest energy and θ, is the scattering angle. The screening parameter, α_s has been evaluated analytically by Bishop [65], and is given in equation 2.4, where E, is the energy in joules.

$$\alpha_s = \frac{5.44 \times 10^{-19} Z^{0.67}}{E} \tag{2.4}$$

By integrating equation 2.3 over all solid angles the total scattering cross section for elastic scattering can be evaluated and substituted into equation 2.2 to give the mean free path used in the simulation.

This total scattering cross section is given by equation 2.5 [66] as,

$$\sigma_{el} = \left(\frac{Ze^2}{8\pi\varepsilon_0 E}\right)^2 \left(\frac{E+E_0}{E+2E_0}\right)^2 \frac{4\pi}{\alpha_s(1+\alpha_s)} \quad (\mathrm{m}^2) \tag{2.5}$$

Newbury and Myklebust [66] have shown that scattering angles can be generated using a random number between 0 and 1, with the correct probability distribution by solving equation 2.6.

$$R(\theta) = \int_{\Omega} \frac{\sigma_{el}(\theta)}{\sigma_{el}} d\Omega \tag{2.6}$$

Where $R(\theta)$, is the random number which generates an angle θ and Ω, is a solid angle. The solution to equation 2.6 is given by equation 2.7.

$$\cos(\theta) = 1 - \frac{2\alpha R}{1+\alpha-R} \tag{2.7}$$

The azimuthal angle of scattering can then be generated using a new random number using, $\phi = 2\pi R$.

It is also necessary to model the loss of energy along a trajectory and there are two mechanisms which contribute to energy loss. Bremsstrahlung radiation is radiation generated through the deceleration of an electron due to electron-electron coulomb interactions. The other mechanism is inelastic scattering events which cause electron transitions including electron hole pair generation. The ratio of energy loss from Bremsstrahlung radiation to that from inelastic scattering events is described by the relationship in equation 2.8.

$$\frac{(dE/dx)_{rad}}{(dE/dx)_{scatter}} = \frac{E_{eV}Z}{800MeV} \tag{2.8}$$

The simulations described ignore the effects of Bremsstrahlung radiation as only a small fraction of the total energy is lost by this mechanism; for example in a silicon detector for 300keV electrons, <0.5% of the total energy loss arises from Bremsstrahlung radiation. Although this is an appropriate assumption for this work, it can not be extrapolated to very high energies.

The original Bethe formula describes the rate of energy loss due to ionisation of atoms in a material from inelastic scattering by a charged particle. The original (non-relativistic) form of the Bethe formula [61, 62] converted from cgs to SI units is given by equation 2.9.

$$-\frac{dE}{dx} = \frac{2\pi N_A \rho Z}{A M_u E}\left(\frac{e^2}{4\pi\varepsilon_0}\right)^2 \log\left(\frac{E}{I}\right) \quad \text{(J/m)} \tag{2.9}$$

Where N_a, is Avogadro's constant, ρ, is the density, Z, is the relative charge on the nucleus, M_u, is the molar mass constant; 0.001kg/mol, E, is the kinetic energy of the electron (in joules), A, is the relative atomic mass, ε_0, is the permittivity of free space and I, is the average excitation potential.

The simulations described also include the generation of "fast" secondary electrons. These are generated where sufficient energy is transferred in a scattering event to generate a secondary electron which travels through the material, scattering in a similar way to the primary electron, leading to a cascade effect. These secondary electrons are particularly important in detector systems when they are ejected at angles close to 90° to the trajectory of the primary electron as this means they are travelling in the plane of the detector. This implies that they undergo large lateral scattering, which as will be shown later is detrimental to detector performance. The model used for generation of secondary electrons in the simulations described is the relativistic form derived by Gauvin and L'Esprance [64] given by equation 2.10.

$$\frac{d\sigma}{d\varepsilon} = \frac{2\pi}{m_0 v^2 E}\left(\frac{e^2}{4\pi\varepsilon_0}\right)^2 \left[\frac{1}{\varepsilon^2} + \frac{1}{(1-\varepsilon)^2} + \left(\frac{\tau}{\tau+1}\right)^2 + \frac{2\tau+1}{(\tau+1)^2}\cdot\frac{1}{\varepsilon(1-\varepsilon)}\right] \tag{2.10}$$

where ε, is the fraction of energy transferred to the secondary electron, $\varepsilon = \Delta E/E$, e, is the electron charge, ε_0, is the permittivity of free space and $\tau = E/m_0c^2$. Integration of equation 2.10 with respect to ε, gives the total scattering cross section for secondary electrons. The boundary conditions for the integration are 1, corresponding to total energy transfer to the generated secondary electron and ε_c which is a lower bound corresponding to an energy transfer which produces a secondary electron with sufficient energy to have a noticeable effect, which in Gauvin and L'Esprance's model is ε_c = 0.01. The equation for the total scattering cross section is hence given by equation 2.11.

$$\begin{aligned}\sigma = \frac{4\pi}{m_0 v^2 E}\left(\frac{e^2}{4\pi\varepsilon_0}\right)^2 &\left[\frac{1}{\varepsilon_c} - \frac{1}{(1-\varepsilon_c)} - \left(\frac{\tau}{\tau+1}\right)^2 \varepsilon_c\right. \\ &\left. - \frac{2\tau+1}{(\tau+1)^2}\ln\left(\frac{1-\varepsilon_c}{\varepsilon_c}\right) + \frac{1}{2}\left(\frac{\tau}{\tau+1}\right)^2\right]\end{aligned} \tag{2.11}$$

The total scattering cross section for fast secondary electrons can be used to determine the mean free path between events which generate fast secondary electrons using equation 2.2, which can then be combined with equation 2.1 to give the distance between secondary electron generation events. When a generation event occurs, the amount of energy transferred to the secondary electron and the direction of both the primary and secondary electron need to be determined. The amount of energy transferred can be found by solving equation 2.12, where R is a random number between 0 and 1 and $\frac{d\sigma}{d\varepsilon}$ is given by equation 2.10.

$$R = \frac{\int_{\varepsilon_c}^{\varepsilon} \left(\frac{d\sigma}{d\varepsilon}\right) d\varepsilon}{\int_{\varepsilon c}^{0.5} \left(\frac{d\sigma}{d\varepsilon}\right) d\varepsilon} \tag{2.12}$$

An integration limit of 0.5 is used as it is not possible to distinguish between the primary and secondary electrons, so that by convention it is assumed that the electron with higher energy after the event is the primary electron, implying that the maximum energy transfer is half the initial energy. An approximate solution to equation 2.12 has been provided by by Gauvin and L'Esprance [64] using the first two terms in a Taylor series expansion. This is required as a solution cannot be found analytically. The first two terms are sufficient to describe the full function and the approximate result is given in equation 2.13.

$$\varepsilon = \frac{\Omega - 2 - \beta + \sqrt{(\Omega - 2 - \beta)^2 + 4(\Omega + \eta - 2\beta)}}{2(\Omega + \eta - 2\beta)} \tag{2.13}$$

where

$$\eta = \left(\frac{\tau}{\tau + 1}\right)^2$$

$$\beta = \frac{2\tau + 1}{(\tau + 1)^2}$$

$$\gamma = \frac{1}{\varepsilon_c} - \frac{1}{(1 - \varepsilon_c)} - \eta\varepsilon_c - \beta \ln\left(\frac{1 - \varepsilon_c}{\varepsilon_c}\right)$$

$$\Omega = R(\gamma + \eta/2) - \gamma$$

Once the amount of energy transferred to the secondary electron has been fixed, the angle between the trajectory of both the primary and secondary electrons and the original trajectory can be found by the conservation of momentum. The results of this calculation give a polar angle for the primary (equation 2.14) and secondary (equation 2.15) electrons. To conserve momentum all three trajectories must be in the same plane, so only a single azimuthal angle is required to completely describe the generation of a secondary electron using $\phi = 2\pi R$.

$$\sin^2\theta = \frac{2\varepsilon}{(2+\tau-\tau\varepsilon)} \tag{2.14}$$

$$\sin^2\theta = \frac{2(1-\varepsilon)}{(2+\tau\varepsilon)} \tag{2.15}$$

The treatment of inelastic scattering as continuous loss along a straight trajectory also includes the effects of secondary electron generation. However incorporating this more complete treatment of secondary electron generation, the effects need to be removed from the generic inelastic scattering model.

The rate of energy loss of the primary electron due to secondary electron generation can be found using equation 2.16 as;

$$\begin{aligned} -\left(\frac{dE}{dx}\right)_{moller} &= \frac{\rho N_a Z}{A}\int_{\varepsilon_c}^{0.5} \varepsilon E \frac{d\sigma}{d\varepsilon} d\varepsilon \\ &= -\frac{2\pi\rho N_a Z}{m_0 v^2 A}\left(\frac{e^2}{4\pi\varepsilon_0}\right)^2 \left[3\ln 2 - \frac{1}{8}\eta + \beta\ln 2 + \ln\varepsilon_c \right. \\ &\left. + \frac{\ln(1-\varepsilon_c)}{1-\varepsilon_c} + \frac{1}{2}\varepsilon_c^2\eta + \beta\ln(1-\varepsilon_c)\right] \end{aligned} \tag{2.16}$$

The next step in the simulation is to model points where electron hole pairs are generated. As it has been established that electronic transitions are the primary form of inelastic scattering, it is reasonable to assume that electron-hole pairs are generated along the straight parts of the trajectory. To determine the number of electron hole pairs generated for a given segment of the trajectory equation 2.17 can be used;

$$n = \frac{\Delta E}{E_T} \tag{2.17}$$

Where n, is the number of pairs generated, E_T, is the pair generation energy and ΔE, is the kinetic energy lost over the segment, found by solving equation 2.18.

$$\Delta E = \int_0^l \left(\left(\frac{dE}{dx} \right)_{bethe} - \left(\frac{dE}{dx} \right)_{moller} \right) dx \tag{2.18}$$

Once the number of generation events along a given section has been identified, the signal generation positions are also identified, and the key detector parameters can be modelled. This latter process is described in Section 2.3.

One problem with the Monte Carlo model used here is that it was originally designed for modelling indirect detectors. The model works in such a way that it is possible to have perfect coupling, so generation events are detected at exactly the same lateral positions at which they occur. However, there is one effect from the indirect case which is not removed. In the indirect case only photons which are travelling in a direction such that they enter the optical coupling system will be detected, whereas in the direct case, events are detected when the charge carriers enter the electric field associated with the collection diode of the pixel. The difference between these two cases depends on the collection aperture of the optical system and the simulation requires an aperture semi-angle to be defined. The fraction of the signal the system will collect can be found by comparing the surface area of a spherical cap formed with the aperture semi-angle, with the surface area of a sphere. For the simulations in Chapter 3 a semi-angle of 10° was used and the conversion factor is calculated using equation 2.19, which for this case yield a factor of 132.

$$C = \frac{4\pi}{2\pi(1-\cos(\theta))} \tag{2.19}$$

There are valid reasons for continuing to use an aperture for the direct case, mainly arising from the memory used by the application. It is favourable to describe a larger number of electron trajectories with an effectively random subset of generation events, than to model a much smaller number of trajectories in full, given that the approximation still leads to an effective description of the cluster created by any given trajectory.

2.3 Detector Parameters

Section 2.2 described how Monte Carlo modelling can be used to simulate the physical process of an electron that generates signal in a detector. This section will describe how these processes are related to the common parameters used to quantify detector performance.

Modulation Transfer Function

The Modulation Transfer Function (MTF) describes how signal is affected by the detection process and is defined by equation 2.20.

$$\mathrm{MTF} = \frac{\mathscr{F}(I_{out})}{\mathscr{F}(I_{in})} \tag{2.20}$$

I_{out}, is the image output from the detector, while I_{in}, is the image projected onto the detector. The loss in strength of signal is related to two effects. The first is due to sampling effects that arise from pixelation of the image and the second arises from the point spread function of signal in the detector. Mathematically a pixelated image can be described as a convolution of the image function with the Point Spread Function (PSF) and a 2D Π function determined by the size of a pixel (equation 2.21).

$$I_p(x,y) = I_0(x,y) \otimes \mathrm{PSF}(x,y) \otimes \Pi(x,y) \tag{2.21}$$

Where

$$\Pi(x,y) = \begin{cases} 1 & \text{if } |x|,|y| < 0.5 \\ 0 & \text{else} \end{cases}$$

Using the fact that the $\mathscr{F}(f(x) \otimes g(x)) = \mathscr{F}(f(x)) \cdot \mathscr{F}(g(x))$, it can be shown that;

$$\mathscr{F}(I_p(x,y)) = \mathscr{F}(I_0(x,y)) \cdot \mathscr{F}(\mathrm{PSF}(x,y)) \cdot \mathscr{F}(\Pi(x,y)) \tag{2.22}$$

$$\mathrm{MTF}(u,v) = |\mathscr{F}(\mathrm{PSF}(x,y))| \cdot |\mathscr{F}(\Pi(x,y))| \tag{2.23}$$

The Fourier transform of the Π function can be derived as shown in equations 2.24-2.28.

$$\Pi(x,y) = \Pi(x) \cdot \Pi(y) \tag{2.24}$$

$$\mathscr{F}(\Pi(x,y)) = \iint\limits_{-\infty}^{\infty} \Pi(x)\Pi(y)\mathrm{e}^{-\mathrm{i}2\pi(ux+vy)}dxdy \tag{2.25}$$

$$\hat{\Pi}(u,v) = \int\limits_{-\infty}^{\infty} \Pi(y)\mathrm{e}^{-\mathrm{i}2\pi(vy)} \left[\int\limits_{-\infty}^{\infty} \Pi(x)\mathrm{e}^{-\mathrm{i}2\pi(ux)}dx \right] dy \tag{2.26}$$

Using the standard result for the Fourier transform of the Π function, gives

$$\hat{\Pi}(u,v) = \mathrm{sinc}(u) \int\limits_{-\infty}^{\infty} \Pi(y)\mathrm{e}^{-\mathrm{i}2\pi(vy)}dy \tag{2.27}$$

$$\hat{\Pi}(u,v) = \mathrm{sinc}(u)\mathrm{sinc}(v) \tag{2.28}$$

Section 2.2 showed how Monte Carlo modelling of signal generation can be performed. However as signal generation is a stochastic process there are an infinite number of different results. The total signal generated from a signal electron trajectory is described by equation 2.29.

$$g_j(x,y) = \sum_{i=0}^{n} \delta(x - m_i, y - n_i) \tag{2.29}$$

Where $\delta(x - m_i, y - n_i)$ is a Dirac delta function centred at (m_i, n_i), where (m_i, n_i) is the location of the signal generation event. It is necessary to find the total signal generated by an electron by summing over all individual generation events, where the probability of a given trajectory occurring is dμ. Thus the PSF of the detector can be found using equation 2.30, where G is the average signal generated per primary electron.

$$\text{PSF}(x,y) = \int \frac{g_j(x,y)}{G} d\mu \tag{2.30}$$

Equation 2.30 is difficult to solve analytically due to the effectively infinite number of unique trajectories, but a good approximation can be made by summing contributions from a large number of trajectories modelled using a Monte Carlo simulation. The number of trajectories needs to be sufficiently high such that the function is smoothly varying when sampled at a frequency orders of magnitude above the intended Nyquist frequency (i.e. For a pixel size of 20μm, the Nyquist frequency is 0.025(μm)$^{-1}$, while the approximate PSF may use a sampling of 1000(μm)$^{-1}$). As the scattering in the model is isotropic, the PSF expressed in polar coordinates has no azimuthal dependence. The Fourier transform can be found by evaluating the Discrete Fourier Transform (DFT) of the approximate function. Methods involving the fitting of standard functions to the data will be described subsequently.

One method for the experimental measurement of the MTF is the knife edge method as described by Meyer et al. [67]. In this method a knife edge or similar object is used to produce a shadow with a sharp transition on the detector which gives a deterministic input that includes spatial frequencies above the Nyquist limit. The knife edge can be easily introduced using an Al insert positioned above the CCD. Other methods for producing this sharp transition include using a beam stop, a wire mounted across the detector or by partial retraction of another camera further up the column, casting a shadow on the camera below and obscuring part of the lower detector. When using the edge method, the edge should be inclined at an angle to the pixel rows and an oversampled line profile of the transition should be acquired by combining information from different rows. This is required to eliminate aliasing effects from frequencies above the Nyquist limit. When the edge is positioned across the centre of a pixel contributions from frequencies above the Nyquist limit interact destructively giving no transfer of signal at the Nyquist frequency. However when the edge is positioned between two pixels the interference from the high spatial frequencies enhance the transfer, doubling the measured MTF at the Nyquist limit. This effect in real space is illustrated in Figure 2.2, where a transition aligned with a pixel centre appears much more gradual.

The line profile or edge spread function (ESF) is related to the point spread function (PSF) *via* the line spread function (LSF). A line can be treated as a series of points infinitely close together, and hence as the point spread function describes how a point source is represented by the detector, the line spread function describes how a continuous line would be represented and is related to the point spread function by equation 2.31, for the specific case where the line is parallel to the y-axis.

$$\mathrm{LSF}(x) = \int_{-\infty}^{\infty} \mathrm{PSF}(x,y)dy \tag{2.31}$$

Since the MTF only requires the magnitude of the Fourier transform, this implies that

$$|\mathscr{F}(\mathrm{LSF}(x))| = \mathrm{MTF}(u,0) \tag{2.32}$$

The ESF can now be treated as a series of parallel lines infinitely close together terminating at an edge, as described by equation 2.33

$$\mathrm{ESF}(x) = \int_{-\infty}^{0} \mathrm{LSF}(x)dx \tag{2.33}$$

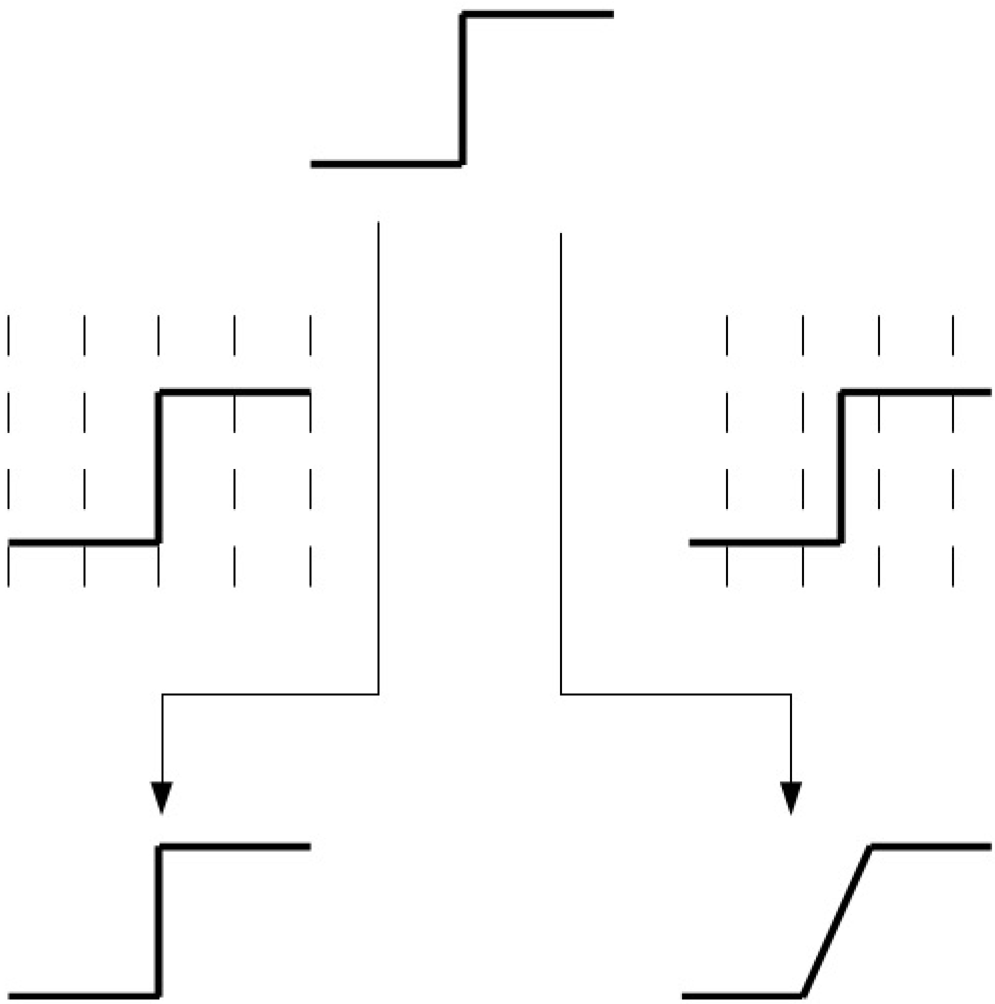

Figure 2.2: The effect of sampling position on the result of sampling a step function.

Therefore, differentiation of the ESF gives the LSF, which can then be Fourier transformed to obtain MTF(x,0).

A common modification to the knife edge method, approximates the initial profile to a function, or a linear combination of functions. A suitable line profile can be fitted to the function shown in equation 2.34.

$$f(x) = y_0 - \frac{g_1}{2}\mathrm{erf}\frac{a-x}{s_1\sqrt{2}} - \frac{g_2}{2}\mathrm{erf}\frac{a-x}{s_2\sqrt{2}} \tag{2.34}$$

where a, g_i and s_i, are fitting parameters, Deptuch et al. [1] have found that two erf terms were sufficient to accurately describe the function. Similarly references [2] and [40] show that fitting functions using this method only requires one or two terms to accurately describe the experimental data. The primary reason for approximating experimental data in this way, is that noise in the images will introduce unwanted noise in the measured MTF, particularly at high spatial frequencies. The edge method is one deterministic approach based on a step function and other deterministic inputs have been used, such as sinusoidal fringes produced in the image plane by an electrostatic biprism used in electron holography [68].

The above deterministic approach is one where a known input is compared to a measured output and the function which converts one into the other is calculated. An alternative approach is a stochastic one, where the input is random, such as in the case of white noise where pixel intensities show a Poisson distribution. The MTF using this noise method is calculated from the Fourier Transform of a white noise input signal. For random white noise the intensity of a pixel $I(m,n)$ is given by $I(m,n) = \eta(m,n) \otimes P(m,n)$, where $\eta(m,n)$ is a stochastic input, and $P(m,n)$ is the point spread function of the detector. Taking the Fourier Transform of the image gives the detector MTF as $\mathscr{F}(\eta(m,n))$ is also white noise, giving a constant background, leaving $\mathscr{F}(P(m,n))$ which is the MTF [68]. The biggest issue with the stochastic approach is that there is a tendency to overestimate the MTF, due to this method not taking into consideration transfer of noise across different spatial frequencies, as described by the Noise Power

Spectrum (NPS) (see subsequent section). Under conditions where the NPS is large, using a stochastic produces inaccurate results [67]. For this reason deterministic inputs are most commonly used for calculating the MTF, despite being more complex to implement.

Wouter et al. [69] have proposed a new method for the measurement of the MTF where the MTF is calculated from analysis of an arbitrary shadow image through estimation of the original image and minimisation of a transformation matrix. The shadow image is up-sampled by a factor of four using bicubic interpolation, then the Fourier transform is calculated and the information beyond twice the original Nyquist Frequency is discarded, to remove aliasing effects. This method has the advantage of not requiring a straight edge, implying that the calculation can be done using a larger number of data points reducing error. This method should produce the same results as the knife edge method used in this work. However, this newer method was not used in the work described in this thesis as it was very prone to noise being introduced from shot noise in the illuminated region.

Noise Power Spectrum

The Noise Power Spectrum (NPS) and Normalised Noise Power Spectrum (NNPS) describe the noise transferred across different spatial frequencies. The definitions of the NPS and NNPS are given by equations 2.35 and 2.36.

$$\mathrm{NPS}(u,v) = \mathrm{Var}_{out}(u,v) \tag{2.35}$$

$$\mathrm{NNPS}(u,v) = \frac{\mathrm{NPS}(u,v)}{N} \tag{2.36}$$

For the output image a spatial frequency dependence is expected from equations 2.35 and 2.36. Firstly, there will be the same finite sampling effects as those present in the MTF, so the same correction needs to be applied as given by equation 2.28. Additionally, it is expected that pixels with statistically above average signal will be clustered together, as the MTF implies pixels influence adjacent pixels.

To find the output variance a series of images with uniform illumination and equal dose are recorded, with a dark correction applied by subtracting the average of a number of images taken with the beam blanked and gain normalisation applied by dividing by the average of the whole series dark corrected and normalised by the mean pixel value and converting from ADC units to electrons.

Equation 2.37 describes how a gain normalised, dark correct image where pixel values refer to an electron dose can be calculated.

$$I_i' = C_{ADC}\left(I_i - \frac{1}{n}\sum D_i\right) \cdot \frac{\overline{(\frac{1}{n}\sum I_i - \frac{1}{n}\sum D_i)}}{(\frac{1}{n}\sum I_i - \frac{1}{n}\sum D_i)} \tag{2.37}$$

I, is an image with uniform illumination and D, is an image where the beam has been blanked. To calculate the conversion factor and be able to normalise for dose, requires an accurate measurement of the dose. The standard method for calculating dose employed here is to first measure the beam current by focusing the entire beam into a Faraday cup. Next a series of images are taken of the entire beam focused onto the detector. The average of the series is taken and the same dark correction and gain normalisation corrections are applied to the image of the beam. Next the sum of all pixels is taken to acquire the total count in ADC units and from this value the dose measured as electrons/pixel and the conversion factor calculated using equations 2.38-2.39.

$$C_{ADC} = \frac{I_{beam}T_{exposure}}{eS_{pixel}} \tag{2.38}$$

$$N = C_{ADC} \cdot \frac{S_{pixel}}{n} \tag{2.39}$$

where I_{beam}, is the beam current, $T_{exposure}$, is the exposure time, e, is the electron charge, S_{pixel}, is the sum over all pixels in the corrected images of the entire beam, N, is the Dose/pixel and n, is the number of pixels in the image.

Milazzo et al. [5] have proposed a method for the conversion from ADC to energy deposited. In this method the detector is illuminated with 5.9keV X-rays from an Fe^{55} source. The ADC pixel values for a 3x3 matrix around the impact pixel are equated to the photon energy and the conversion factor is found. This method eliminates the need to accurately measure the beam current and take images with a high intensity beam focused on the detector. However it relies on the assumption that the proportion of energy deposited by mechanisms that produce signal is the same for electrons and X-Ray photons. Given that the energy of a photon is absorbed in a single absorption event, whereas the energy of an electron is dissipated by a sequence of inelastic events along the electron trajectory [8], the validity of this assumption is questionable. It is also an inappropriate method for the characterisation of thin detectors, as in this situation electrons pass through the detector before all their energy is deposited.

In the measurement of the NPS for each image within a series of images, the average of the next and previous images are subtracted resulting in a series of images which have an expectation value of 0 and hence a variance of $I^2(x,y)$. The Fourier Transform of this images yields the output variance as a function of spatial frequency, and generally the azimuthal average is calculated to return the 1D NPS, followed by division by the dose to yield the NNPS.

This method leads to artefacts arising from effects due to the edge of the image and to overcome this either the image is wrapped around the edge, which is the method that is employed here, or a suitable, smooth windowing function [70] is used.

Typically it is assumed that the NNPS is independent of dose. However this assumption only holds for images recorded at a dose where Poisson noise is dominant. In very low dose images and very high frame rates, the noise from the detector readout can dominate to form an appreciable proportion of the total noise. The spatial frequency dependence of the background noise arises solely from pixel sampling effects, and is independent of dose and can be estimated from the NPS of a dark image.

Detective Quantum Efficiency

The Detective Quantum Efficiency is a measure of how effective the detector is at recording all spatial frequencies in the image. A perfect detection device has a DQE of 1 across all spatial frequencies. This corresponds to every electron being recorded with equal weight, with perfect positional accuracy and no readout noise [71]. However, none of these conditions is met for realistic detectors, the DQE can be defined by equation 2.41.

$$DQE = \left(\frac{SNR_{out}}{SNR_{in}}\right)^2 \tag{2.40}$$

$$DQE = \left(\frac{S_{out}N_{in}}{S_{in}N_{out}}\right)^2 \tag{2.41}$$

Where SNR, is the signal to noise ratio in the image, S, is the signal and N, is the noise; "in" denotes the image projected onto the detector and "out" the image output of the detector. As both the Signal and Noise are frequency dependent, the DQE is also frequency dependent.

Equation 2.20 showed that $S_{out}(u,v) = \mathrm{MTF(u,v)} \cdot S_{in}(u,v)$, and that the NPS describes the noise in the output image. When defining the SNR of an image, it is the amplitude of the noise that is of interest, which in the case of uniform illumination equals σ, the standard deviation. The NPS records the power of the noise, as $E \propto A^2$, NPS= σ^2, hence $\mathrm{NPS}(u,v) = N_{out}^2$. This is consistent with our method of finding the NPS through finding the variance, σ^2.

An input image with uniform illumination has a Poisson distribution of signal and it is an established property of a Poisson distribution that the variance is equal to the mean, which for an electron image is the dose in electrons/pixel, $N_{in} = N$. Using this result the DQE can be expressed in terms of the other measured properties of the detector, as given by equation 2.42.

$$DQE(u,v) = \frac{N \cdot \mathrm{MTF}^2(u,v)}{\mathrm{NPS}(u,v)} \tag{2.42}$$

As already discussed it is generally assumed that the NNPS is independent of dose so the DQE is also independent of dose. However this assumption is not true at low dose, due to noise in the readout, and implies that at low dose the DQE is reduced. In addition at very high dose decreasing quantum efficiency is observed, due to saturation of the detector, such that additional signal at the input does not lead to an increase in signal at the output.

Other Parameters

The gain of a detector is the signal generated by each electron. A high gain generally leads to a better signal to noise ratio as more signal is generated with the same noise level. A high gain is particularly important in lose dose microscopy as it maximises the signal for a given dose. An important contribution to the gain is the energy deposited in the sensitive layer of the detector. Formally the gain of the detector is $\frac{1}{C}$ where C is the conversion factor given by equation 2.38.

The dynamic range of a detector describes the range of values that a pixel can take and how many electrons a pixel can detect before it saturates. The dynamic range is important for high signal in images which leads to a good signal to noise ratio and better data for quantitative analysis. The dynamic range is dependent on two factors: firstly the saturation point of a pixel, which is the total amount of signal the pixel can hold. In a direct detector this would be determined by the capacitance of the pixel and the gain. Saturation of a pixel can be defined in two different ways; absolute saturation is the dose above which there is no observable increase in the pixel response and the limit of linearity is the dose at which the pixel response becomes non-linear. There is not typically a sharp transition between these but rather a smooth transition from linear gain to absolute saturation. The limit of linearity is an appropriate measure in applications where knowledge about the dose is important, as when gain becomes non linear, it is much harder to analyse the dose present in an image without a model for the non linearity. In this approach the dynamic range is defined by equation 2.43 [72].

$$R = 20\log_{10}(\frac{\bar{I}_{Max}}{\bar{I}_{Dark}}) \tag{2.43}$$

where $\bar{I}_{Max}$, is the average pixel value in a saturated image and $\bar{I}_{Dark}$, is the average pixel value in a dark image.

Another definition of dynamic rage relates to the bit depth of the image. Typically pixels values are recorded as 16-bit integers, therefore the maximum value achievable is 65,536. If the analogue signal from the sensor exceeds this value, the signal will become clipped when digitising.

Chapter 3

Modelling Direct Detectors

3.1 Introduction

This chapter explains the results of Monte Carlo simulations of direct detectors, the implementations of which were described in Section 2.2. The program which implements the model returns a number of different results: the MTF and DQE, as described in Section 2.3; the pulse height distribution, a histogram of the signal generated by a primary electron; the trajectories of each electron through the detector and the positions of detected signal generating events. The three areas investigated in detail are; the effects of detector thickness and operating voltage on conventional silicon based direct detectors; the effects of accelerating voltage and surface dead layers for low voltage ($<$20kV) performance and the effects of not having the electric field associated with the charge collection diode of the pixel extending through the entire sensitive layer thickness.

3.2 Detector Thickness and Voltage Effects

3.2.1 Simulation Details and Methods

Using the Monte Carlo model described in the previous chapter, Si detectors were modelled for a range of energies from 20-300keV, at three different detector thicknesses, 20μm, 25μm and 50μm and with a maximum spatial frequency of 25mm^{-1} at the detector plane which corresponds to a pixel size of 20μm. For each energy-thickness set 20,000 electrons were included in the simulations.

To compare the MTF and DQE across the whole dataset of differing thicknesses and energies, scripts were written in the *Bash* shell script to extract the MTF and DQE values at 0.25 and 0.5 pixel^{-1}. The MTF and DQE were then corrected for the sampling effect of a pixelated image as described in Section 2.2. Similar scripts were used to retrieve values for the mean pulse height from the pulse height data. Signal generation positions were loaded as tables into a *MySQL* database for analysis of point spread functions and saturation effects. Point spread functions were calculated with all electrons entering at the same point. The generated electrons were then counted into bins organised by distance from the input position rounded to the nearest micron. The azimuthal average was then evaluated, where the total count, at a given distance from the input was corrected for the area, $psf(x) = \frac{count}{2\pi x}$. From this, the distance at which the signal falls to a given fraction of its starting value can be calculated.

The second problem tackled using the database is the problem of pixel saturation. As saturation occurs at relatively small numbers of electrons, averages do not give an accurate prediction of saturated pixels. To solve this an alternative detector was simulated by choosing a random primary electron and randomising its input position on a 16 by 16 pixel array. A schematic of this is shown in Figure 3.1. This process was repeated until a desired electron dose was achieved. The number of electron hole pairs generated in each pixel was then counted and this value compared to a saturation threshold. The number of pixels which exceed this threshold were then counted. In this

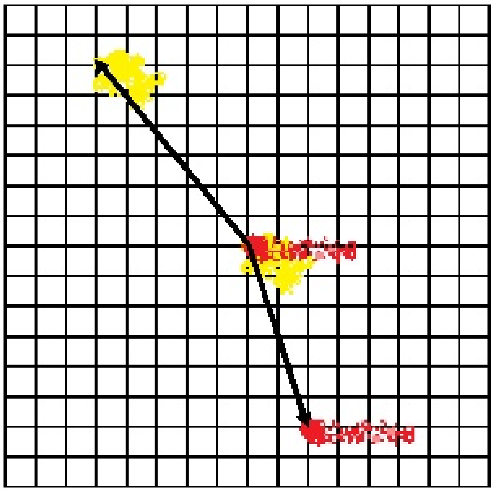

Figure 3.1: The simulations shifts all signal generating events associated with a single electron trajectory through a random translation vector within a 16 by 16 pixel array.

thesis saturation calculations were carried out for doses of 1, 10 and 100 electrons/pixel for a 50μm thick detector over a 20-300keV energy range in 20keV increments.

3.2.2 Results

MTF

Figure 3.2 shows the variation in the MTF with energy at 2 different spatial frequencies for different detector thicknesses.

There are a number of observations that can be made from this data. At very low energies there is no variation in the MTF between the different thicknesses and each thickness exhibits a minima in the 20-300kV range. For thinner detectors this minima occurs at a lower energy and for thicker detectors the MTF at the minima is smaller. As the spatial frequency increases the minima shifts to lower energies. Above the minima, the MTF improves, rapidly at first before gradually trending towards a limit. The location of the minima are summarised in Table 3.1.

Figure 3.3 shows the MTF of the 25μm detector over a range of energies, which shows that the detector at higher energies performs better at higher spatial frequencies but worse at lower spatial frequencies, while at lower energy the opposite is true.

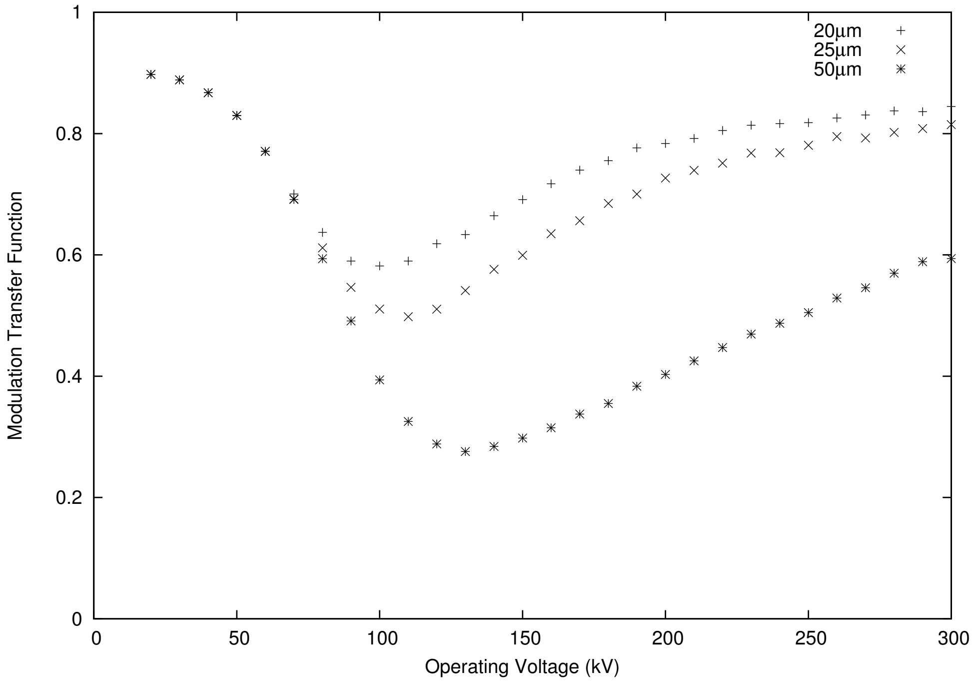

(a)

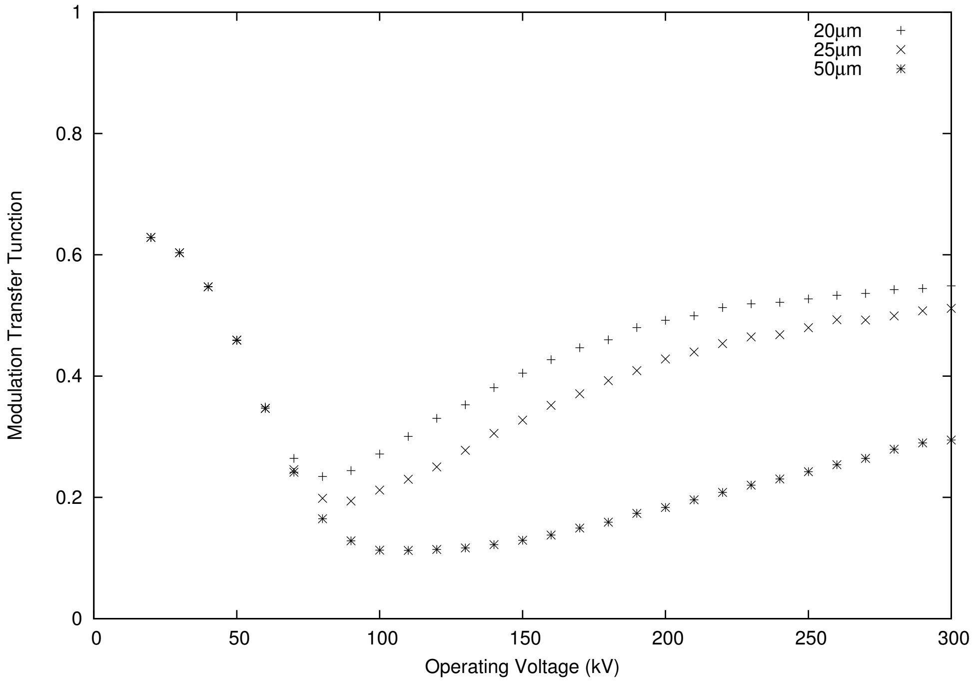

(b)

Figure 3.2: The dependence of the MTF on detector thickness and operating voltage. Variation of the MTF at (a) 0.25 $pixel^{-1}$ and (b) 0.5 $pixel^{-1}$, with respect to energy and detector thickness for a detector with a 20μm pixel size.

Thickness	Spatial Frequency (pixel^{-1})	Operating Voltage (kV)	Modulation Transfer
20μm	0.25	100	0.58
	0.5	80	0.23
25μm	0.25	110	0.50
	0.5	90	0.19
50μm	0.25	130	0.28
	0.5	110	0.11

Table 3.1: Position of minima in the MTF as a function of operating voltage.

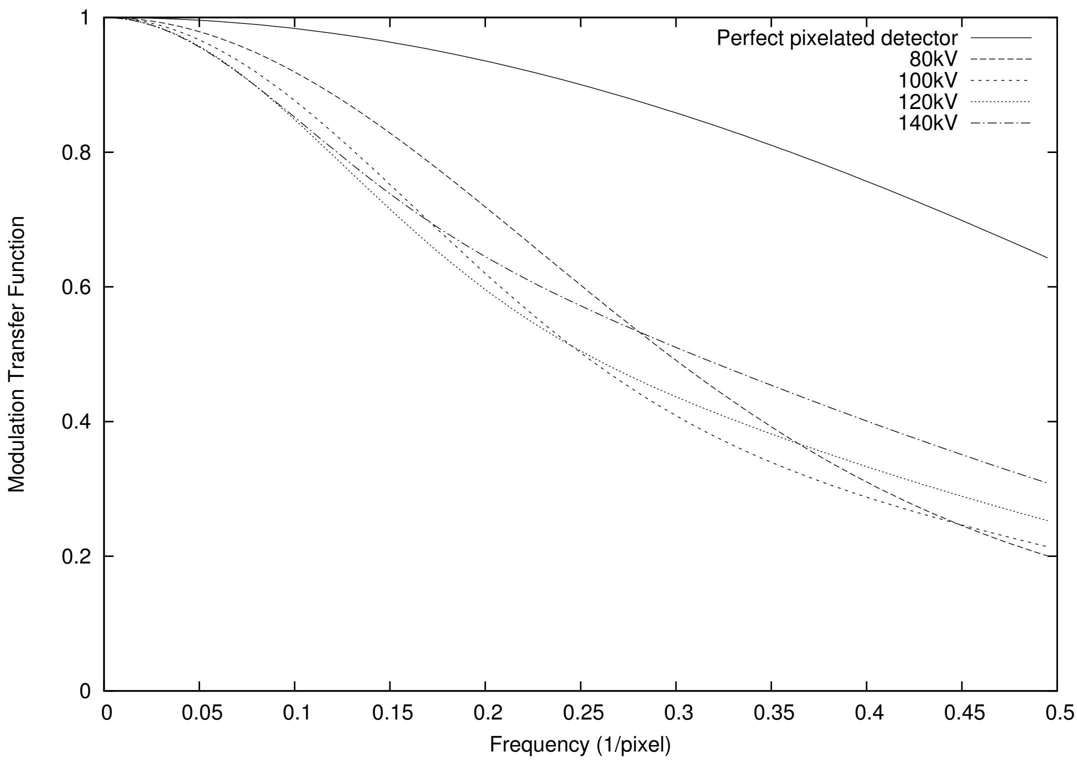

Figure 3.3: MTF of a 25μm detector for a range of energies.

Thickness	Spatial Frequency (pixels^{-1})	Operating Voltage (kV)	DQE
20μm	0.25	100	0.27
	0.5	80	0.072
25μm	0.25	110	0.23
	0.5	90	0.059
50μm	0.25	130	0.12
	0.5	100	0.033

Table 3.2: Position of minima in the DQE as a function of operating voltage.

DQE

The results for the operating voltage dependence of the DQE are shown in Figure 3.4 with many features similar to those of the MTF, which is to be expected given the relationship between the MTF and DQE. At low voltages there is no variation with detector thickness. There is a local minima which occurs at higher energies, which is more pronounced as the thickness of the detector increases and shifts to lower energies at higher spatial frequencies. The location of the minima are summarised is Table 3.2. There are some differences between the DQE and MTF, for the MTF a thinner detector always exceeds the performance of a thicker detector at voltages above the minima. However for the DQE at high voltage thicker detectors can outperform thinner detectors. For example at 0.25 pixel^{-1} and 300kV the 25μm detector outperforms the 20μm one. There is also a region between 60kV and 90kV accelerating voltage where the thicker detectors outperform the thinner ones.

Pulse Height Distribution

The pulse height is the amount of detectable energy deposited in the detector; some energy goes undetected by being deposited in dead layers such as CMOS metalisation and damaged surface layers with a high concentration of recombination centres. Some energy is not deposited at all as the electron escapes the detector, either through the top surface after going through a very high angle scattering event, or passing through a thin detector. It was measured by tracking the number of signal generation events as-

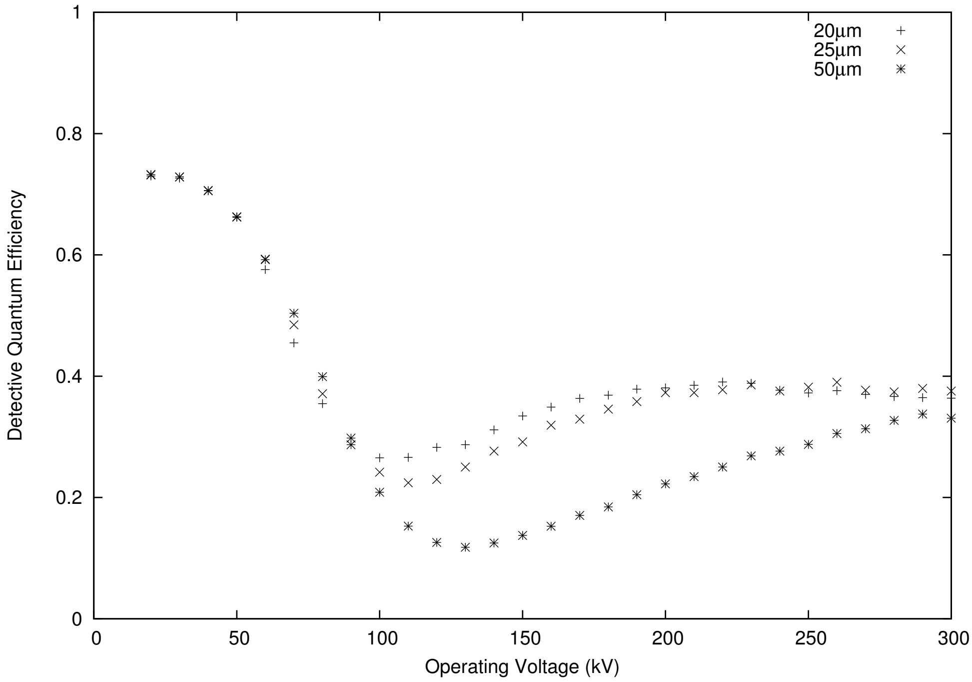

(a)

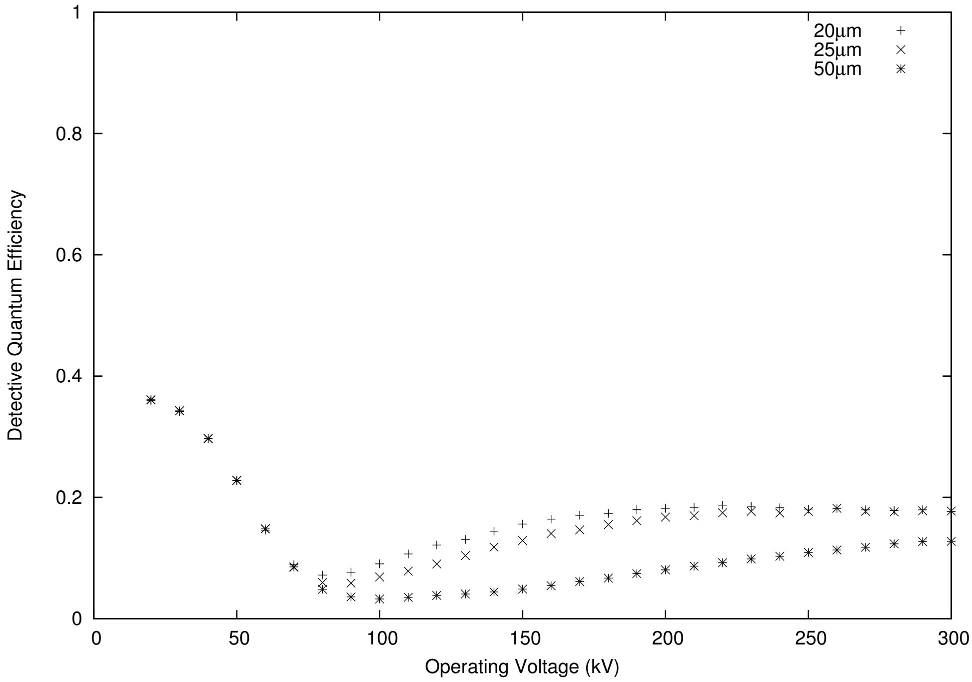

(b)

Figure 3.4: The dependence of DQE on the detector thickness and operating voltage. Variation of DQE at (a) 0.25 $pixel^{-1}$ and (b) 0.5 $pixel^{-1}$, with respect to energy and detector thickness for a detector with a 20μm pixel size.

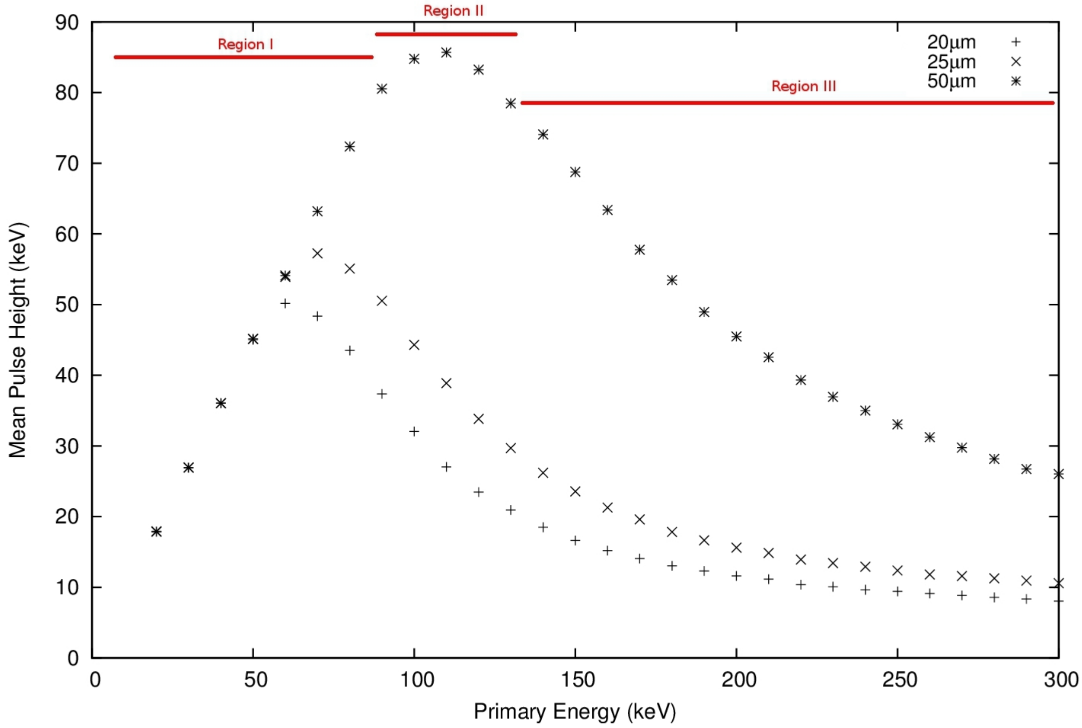

Figure 3.5: Mean pulse height variation with Energy. The regions marked are those described in the text for the 50μm thick detector.

sociated with a given primary electron and converting this to an energy *via* the energy associated with the signal generating transition, *i.e.* the band-gap of the material and then multiplied to remove the sampling effect of the aperture, for these simulations a factor of 132. This correction is necessary because the simulation program was originally designed to model indirect detectors. While other effects of indirect detection can be removed from the model, the aperture of the coupling system cannot. A full explanation of where the factor of 132 comes from and the implications of this sampling was discussed at the end of Section 2.2.

Figure 3.5 shows how the mean energy deposited in the detector is affected by the primary energy and detector thickness. In Region I there is a linear relationship between primary energy and the deposited energy, with around 90% of the primary energy being deposited. In this region the dependence is independent of detector thickness. The next region is defined by a turning point which occurs at lower energies for thinner detectors (Region II). At higher energies the mean energy falls rapidly before tailing off with thinner detectors having a lower limiting mean pulse height (Region III).

Figure 3.6 shows that at low energy there is a main peak in the pulse height distribution close to the primary energy, with a smaller secondary peak at lower energy. As the energy is increased the peaks move apart and the lower energy peak grows in intensity at the expense of the higher energy peak.

The distributions in Figure 3.7 show the differences in the pulse height distribution for different detector thicknesses. It is clear that the higher energy peak occurs at 90keV regardless of thickness and that this peak is less intense for thinner detectors. There is a lower energy peak which increases in height for thinner detectors and the position of this peak varies with thickness, shifting to lower energies for increasingly thin detectors.

Point Spread Function

Figure 3.8 shows the point spread functions for a 25μm thick detector over a range of energies. The full-width-half-maximum (FWHM) (the distance required to drop to half the initial signal) of the PSF is much larger for the low energy case. However the high energy functions have much longer tails which extend to large lateral displacements.

Figure 3.9 shows the point spread functions calculated for the three different detector thicknesses at 80, 100, 120 and 140kV accelerating voltages. It is clear that the PSFs are similar at low energies but show clear differences at high energies. There are two regions in the curves, an initial sharp drop close to zero displacement, becoming more pronounced with increasing energy and reduced thickness and a region which is initially flatter before transitioning into a sharp drop trending towards a common maximum distance.

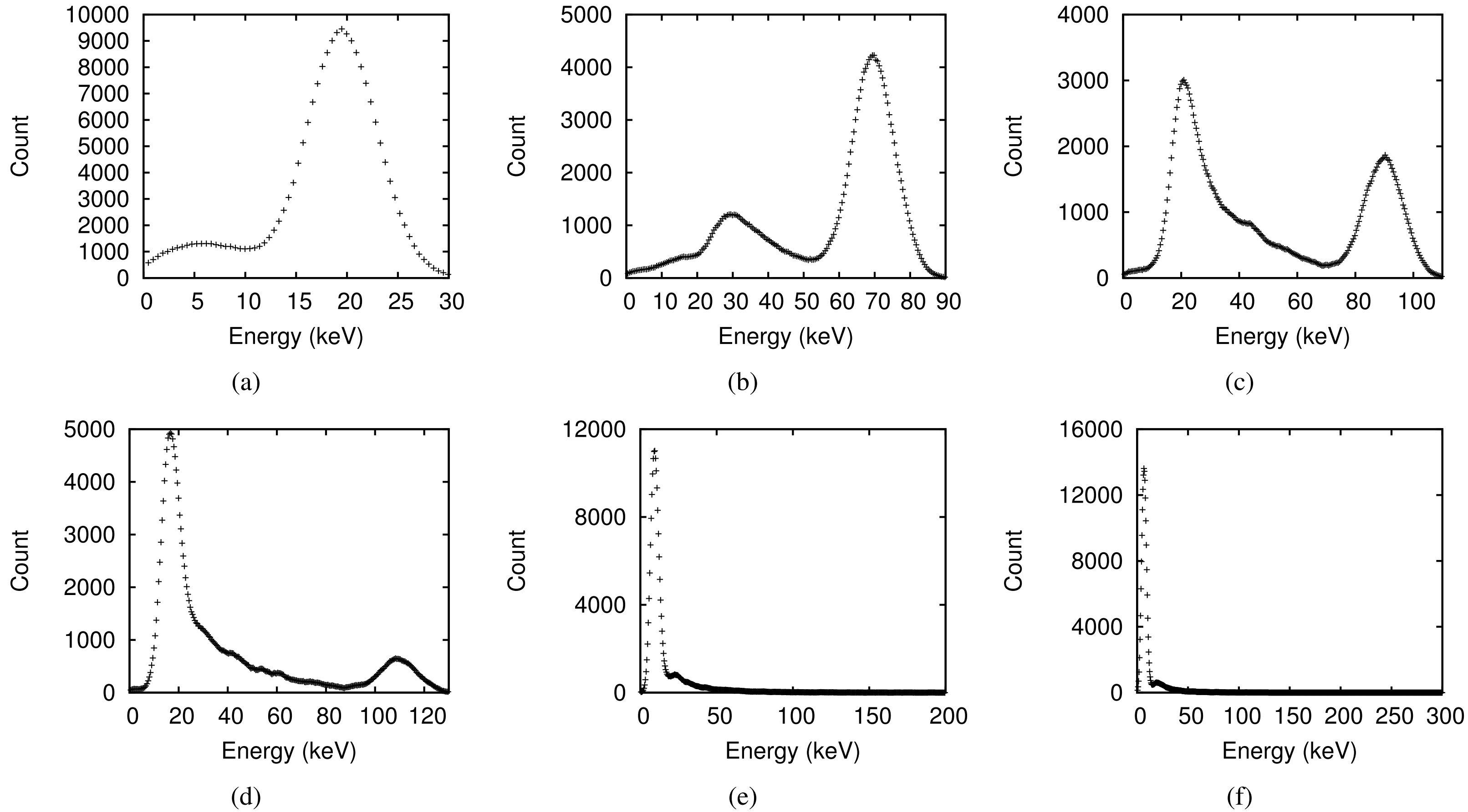

Figure 3.6: The dependence of pulse height distribution on the detector thickness and operating voltage. Figures show the Pulse Height Distribution for a a 25μm thick detector at (a) 20kV, (b) 70kV, (c) 90kV, (d) 110kV, (e) 200kV and (f) 300kV.

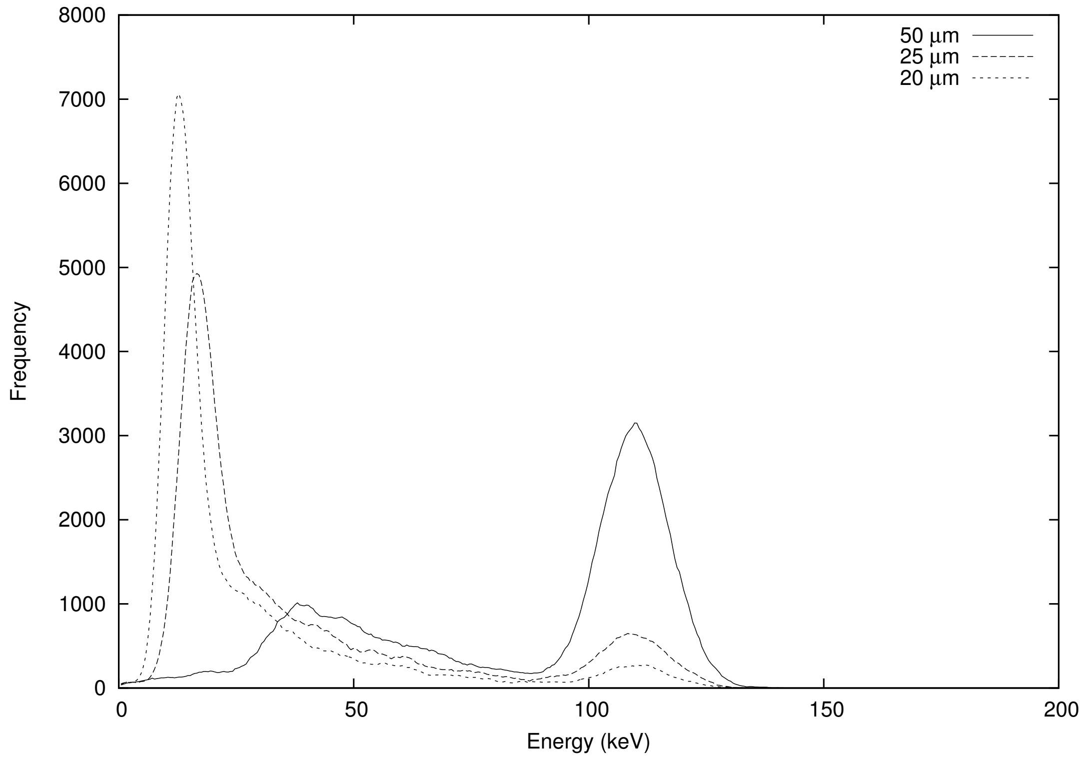

Figure 3.7: Pulse Height Distributions for the three detector thicknesses at 90kV accelerating voltage.

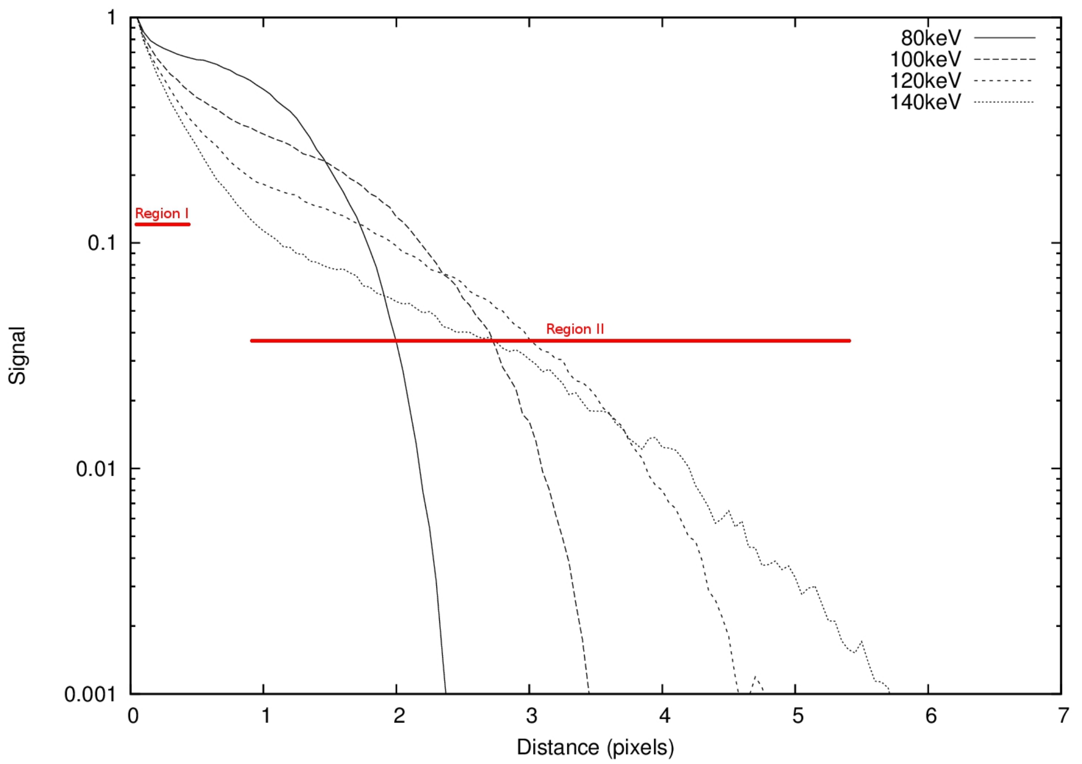

Figure 3.8: Normalised point spread function for a 25μm detector at a range of energies. The regions marked are those described in the text.

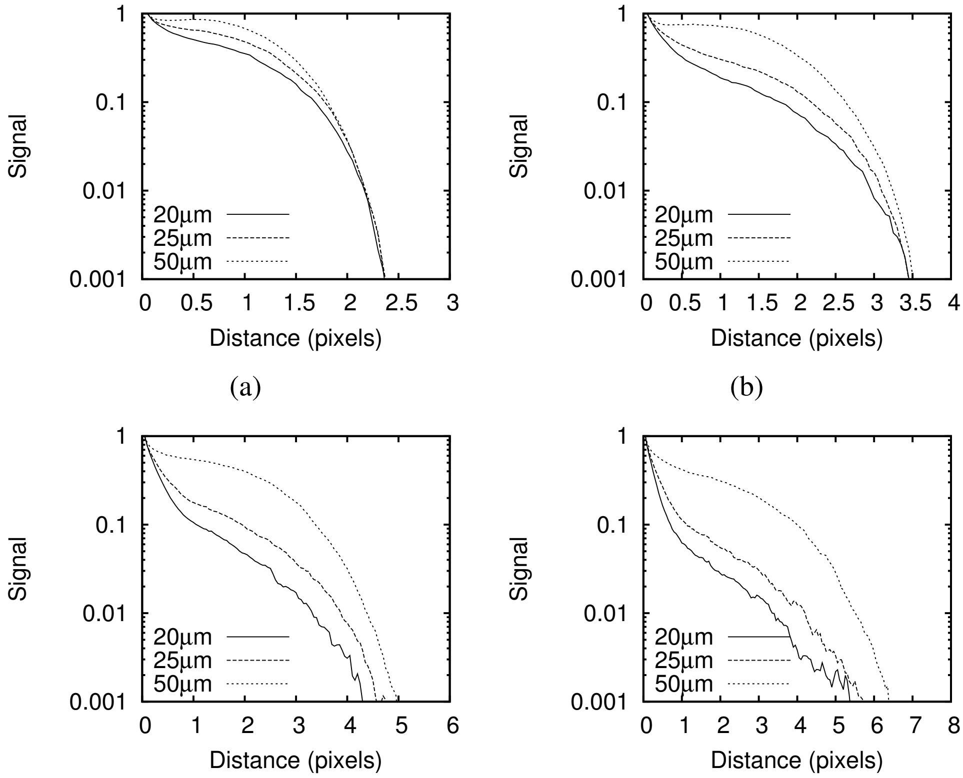

(a) (b)

(c) (d)

Figure 3.9: The dependence of PSF on detector thickness at operating voltages of (a) 80kV, (b) 100kV, (c) 120kV and (d) 140kV.

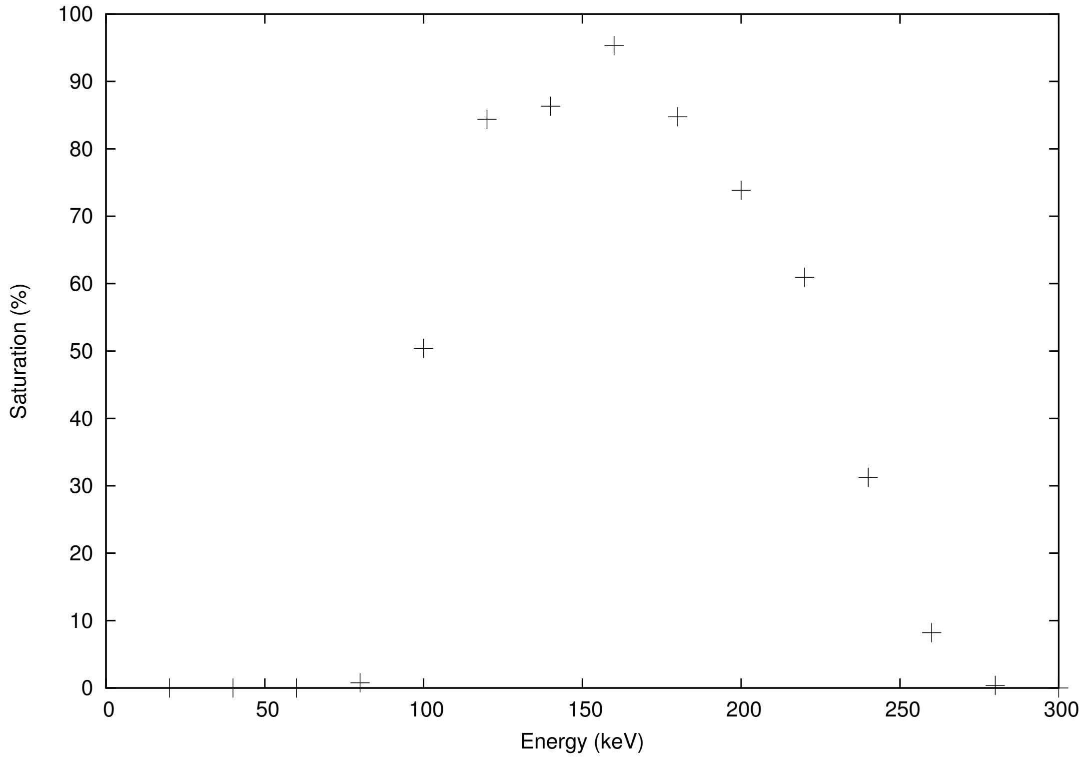

Figure 3.10: % of pixels which saturate at an average dose of 100 primary electrons/pixel for a 50μm detector.

Saturation

Figure 3.10 shows the results from the saturation analysis. Between 80keV and 280keV significant numbers of pixels saturate at a dose of 100 electrons/pixel, implying a lower dose is required for recording at these energies. It is important to note that the energy with the highest % saturation at this dose, is different to the energy which has the highest mean pulse height. Figure 3.11 shows the pulse height distribution for a 50μm detector at 140kV accelerating voltage, the voltage where there are the maximum number of saturated pixels. However this analysis will underestimate the number of saturated pixels due to the higher proportion of edge pixels arising from the smaller detector area modelled.

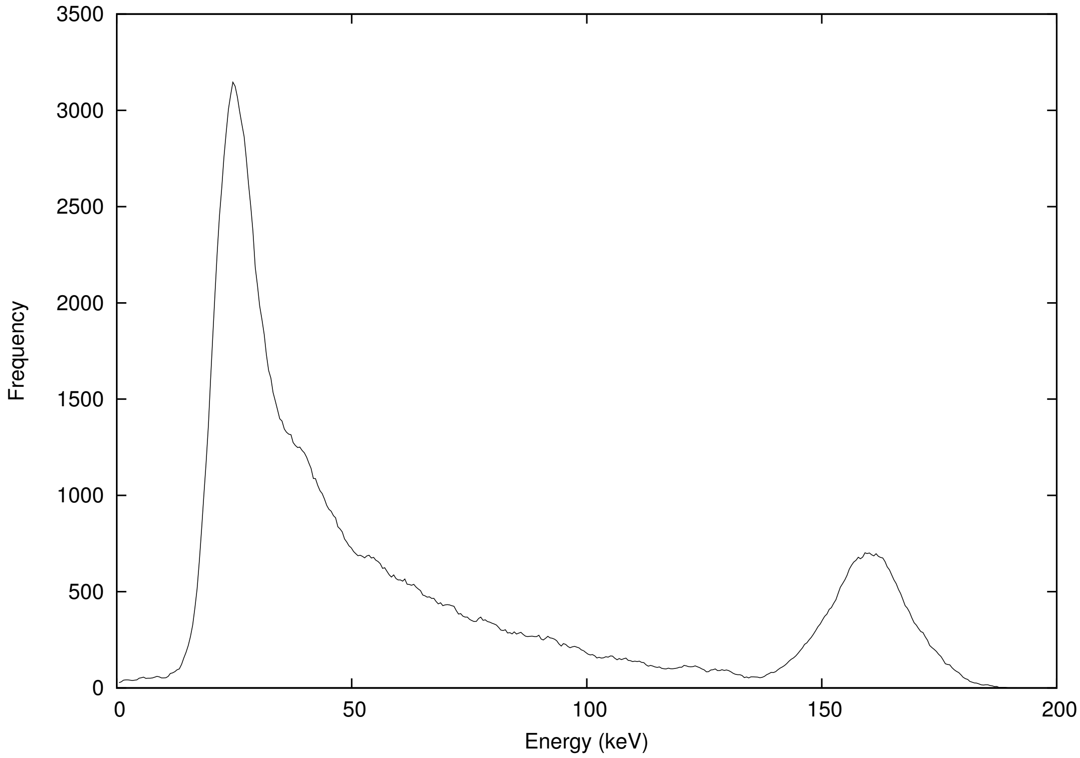

Figure 3.11: Pulse height distribution of a 50μm detector at 160kV accelerating voltage.

3.2.3 Discussion

From the results described in the previous sections it is clear that there are a number of factors that can be identified which affect detector performance. The core reason is that as the accelerating voltage is increased, increasing the energy of the primary electrons, the penetration depth of the electrons increases. When this penetration depth exceeds the detector thickness electrons will pass through the detector before all their energy is deposited. This is confirmed by the pulse height distributions in Figure 3.6, where the high energy peak is close to the incident electron energy. As the energy increases over a relatively narrow energy range the lower energy peak becomes more pronounced before dominating the distribution at high energies. The progression of distributions in Figure 3.6 is also consistent with the mean pulse heights shown in Figure 3.5. Initially these show only the energy deposited in the detector, before reaching a turning point due to electrons passing through the detector and depositing less energy in the detector.

Finally the mean energy tails off when virtually all electrons pass through the detector. Equation 2.9 shows that the stopping power of the material will be reduced as the energy is increased, which implies that less signal is generated along any trajectory. The trajectories of higher energy electrons also tend to be straighter and therefore shorter, as the combination of equations 2.4 and 2.7 show that significant changes in direction are less likely at higher energy.

Intuitively, the deposited energy and the mean lateral displacement of the signal which affect the MTF are correlated. The more energy deposited, the longer the trajectory will need to be to dissipate it, which statistically will lead to larger displacements. Comparing the mean pulse height and MTF results it can be seen that the turning point in mean energy deposited occurs at a lower energy than than the turning points in the MTF data. This is due to the fact that initially electrons which pass through the detector (not depositing all their energy), causing the mean energy to drop, are those electrons which follow a straighter trajectory through the material. These are also the electrons which have the smallest detrimental effect on the MTF as they do not generate signal at large lateral distances.

Figure 3.3 shows the MTF over a range of energies, the interesting result here is that higher operating voltages perform worse at low spatial frequencies compared to lower voltages, but outperform the lower operating voltage cases closer to the Nyquist limit. The reasons for this can be understood by examining the point spread functions in Figure 3.8. Equation 2.23 shows that the point spread function is related to the MTF by a Fourier Transform so physical mechanisms which affect the PSF also affect the MTF. Figure 3.8 shows that in the high energy case there is a larger amount of signal generated at large lateral displacements. This is due to the fact although high energy electrons are less likely to deposit all their energy in the detector, those which do reach larger lateral displacements, due to longer trajectories being associated with higher energies. In addition, more energy is deposited as the electron energy decreases at the end of a trajectory. The overall effect of these are that for high energies, while the magnitude of the effect is smaller, the reach is longer, thus affecting lower spatial frequencies. Conversely, at high spatial frequencies corresponding to low lateral displacements, the range of energies which can have an effect is larger, so the high energy case performs better due to a smaller fraction of the signal being generated away from the initial incident position.

Figure 3.9 shows the effects of thickness on the point spread functions. Comparing the regions marked in Figure 3.8 with the corresponding regions in Figure 3.9, in the first region marked, the initial sharp drop arises from electrons with straight trajectories passing through the detector, depositing energy in a very narrow cone around the initial position. As the energy is increased or the thickness reduced, the proportion of electrons which exhibit this behaviour is increased. Thinner detectors imply a shorter distance over which the electron has to travel to escape the detector, which leads to fewer scattering events. This means that there is a lower chance of large angle scattering occurring. Hence, for a given energy a higher proportion of electrons pass through the detector making the initial drop which characterises the first region larger. In addition there are fewer small angle scattering events implying that the mean lateral displacement is reduced making this initial drop in signal sharper. In the second region identified in Figure 3.9, the response in the PSF arises from electrons which deposit more energy in the sensitive layer due to trajectories not being straight. In Figure 3.9 the PSF of the 50μm thick detectors are initially quite flat, with larger amounts of signal being retained at greater distances compared to the thinner versions. This indicates a high probability that electrons will be scattered as they pass through the detector. However the probability of an electron reaching a larger displacement become increasing unlikely and a transition into a sharp drop in the amount of signal being generated occurs. As the detector thickness decreases there is a significant reduction in the probability of a electron reaching a given displacement, as there is a much narrower range in the direction of travel which does not result in the electron escaping the detector before reaching a given displacement. The maximum displacement is the same for all thickness for a given energy since the theoretical maximum displacement arises when an electron immediately undergoes a 90°scattering event and then travels straight in the plane of the sensitive layer. In this situation the distance to the opposite side of the detector is not relevant, so thickness does not effect the maximum displacement.

In the previous section, regions were identified where in terms of the DQE, thicker detectors perform better, namely the 60-90keV energy range and very high energies (Figure 3.4). As these regions do not have an improved MTF, the improvements must arise from a reduction in noise. At high energy, for a thinner detector the amount of energy deposited in the detector is reduced, meaning that the SNR is degraded, while a thicker detector generates a larger signal. At high energy there is a diminishing return in MTF improvement from thinning of the detector, so a thick detector can produce a better DQE. Similarly it was shown that thicker detectors have better DQE just before the turning points in the energy dependent performance. This is due to the fact that just before the turning point some electrons pass through the detector, not depositing all their energy. The loss of this signal does not improve the MTF as only electrons with straight trajectories pass through the detector, but does reduces the SNR due to a lowering of the gain. It was shown in Figure 3.5 that for a 25μm thick detector an increase from 150keV to 200keV primary energy results in a 25% reduction in the amount of energy detected and hence a 25% reduction in overall signal.

The last area of discussion relates to saturation of detectors. From Figure 3.10 it is clear that saturation of pixels occurs when the mean energy deposited is high. However, it is also clear that the level of saturation is not simply linked to the amount of energy deposited; for a 50μm thick detector the energy of peak saturation is 160keV, whereas the highest mean energy occurs at 110keV. The turning point in the mean energy is attributed to the declining influence of electrons which deposit all their energy within the detector and the corresponding rise in the number that pass through the detector. The fact that the turning point in the amount of saturation occurs at a higher energy indicates that fully absorbed electrons are more important to saturation than raising the mean deposited energy. For saturation the key parameter is how much energy is deposited in any given pixel and an electron which is fully absorbed deposits more energy in a small cluster, particularly near the end of a trajectory. This implies that these types of electrons are more efficient at bringing pixels to their saturation point.

3.2.4 Conclusions

In this section I have looked at the effects on detector performance of changing operating voltages and detector thicknesses. Significant improvements arising from thinning have been identified and attributed to the effects of electrons passing through a thin detector. This hypothesis is supported by data relating to pulse height distributions and how these develop as parameters are changed. The energy dependence of the MTF and the DQE has been shown to exhibit a minima at mid-range energies, close to those associated with low voltage transmission electron microscopy. Finally, the effects of high gain are investigated to illustrate the problem of pixel saturation at relatively low dose emphasising the requirement for the formation of images through summation of multiple individual frames.

3.3 Dead Layer Effects

3.3.1 Introduction

Direct detectors also have interesting applications in the detection of low energy electrons, such as those generated in electron backscatter diffraction (EBSD), due to the higher gain associated with direct detection and of particular interest is in the use of thin back illuminated detectors. In this configuration the detector is thinned such that electrons pass directly into the sensitive layer, rather than dissipating energy and losing signal in the metalisation layer of the CMOS readout electronics. The method of thinning is very important. Thinning is normally carried out through a mechanical process of grinding and polishing, which is a destructive process that creates many crystal defects in the surface region. These crystal defects act as very efficient recombination centres, resulting in a large drop in carrier lifetime in the damaged region, which in turn means that much of the signal is not collected and the surface layer is effectively electrically dead. By changing the thinning process it is possible to reduce surface damage. This section will examine how the thickness of surface dead layer affects the detector performance.

3.3.2 Experimental Details and Results

There have been a number of investigations into sub-surface damage from mechanical thinning, which has shown that the damage layers are of the order of 1μm [73]. As such this was used as the starting point for a series of models, with thinner layers being investigated to model possible improvements to performance arising from improved thinning processes. The effects of the dead layer on the MTF and DQE were modelled for a 50μm thick, back illuminated detector. The model was simplified into three distinct layers; a Si surface layer which is assumed to be electrically dead, such that any inelastic events in this layer do not lead to signal generation; a 50μm thick sensitive Si layer and a supporting 1μm thick Cu layer representing the CMOS metalisation. The detector was modelled across a 2-20keV energy range at 2keV intervals for dead layer thicknesses of 10, 100 and 1000nm.

Figure 3.12 shows the energy dependence of the detector performance for various dead layer thicknesses. What is immediately clear is the dead layer has little effect on the MTF, with the exception being the lowest energy for the thickest dead layers where no signal is measured. The DQE performance is more interesting and it is clear that as the energy of electrons is reduced, the DQE falls. The dependence is non-linear, starting at 20kV and reducing the energy there is initially only a slight fall in efficiency with reducing energy, before experiencing a much more rapid drop in efficiency as the energy is reduced. For example, for the case of a 100nm dead layer there is a reduction

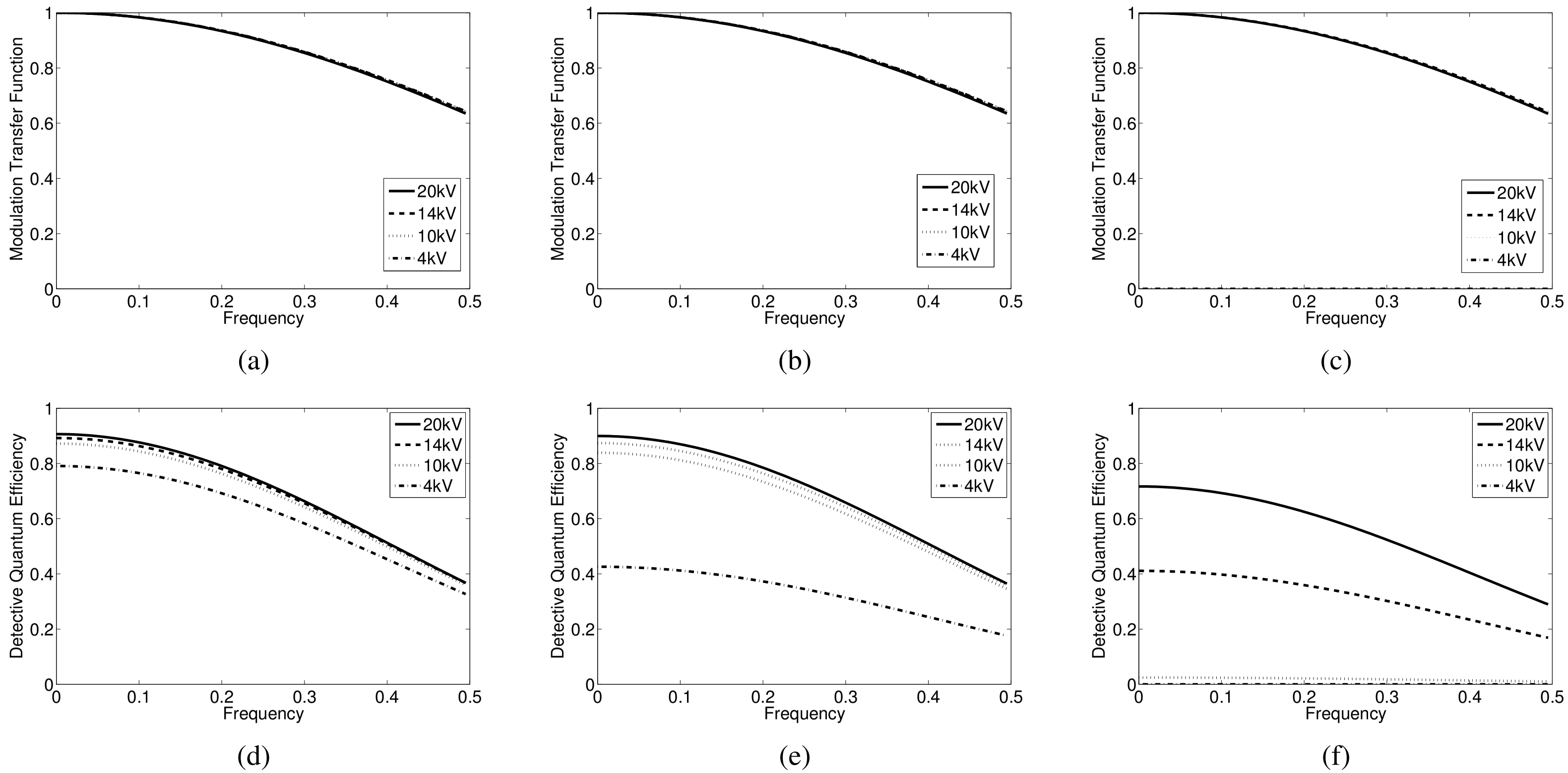

Figure 3.12: The energy dependence of detector performance with varying dead layer thickness. (a)-(c) show the MTF for 10nm, 100nm and 1000nm thick dead layers respectively. (d)-(f) show the DQE for a 10nm, 100nm and 1000nm thick dead layers.

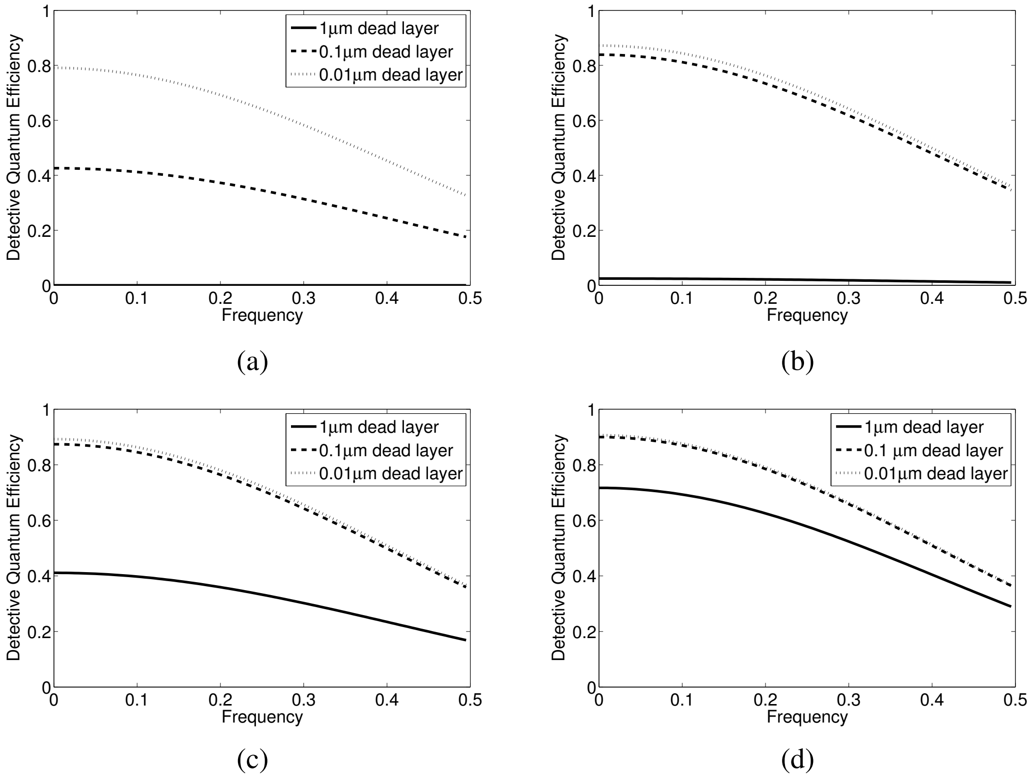

Figure 3.13: The dependence of the DQE on detector thickness with a primary electron energy of (a) 2keV, (b) 10keV, (c) 14keV and (d) 20keV.

of 0.05 in DQE(0), by reducing the energy from 20kV to 10kV, while reducing from 10kV to 4kV results in a reduction of 0.4 in DQE(0). Figure 3.13 shows the thickness dependence of detector performance at various different operating voltages is is clear that the detrimental effects of a dead layer are more apparent at lower voltages and when the dead layer is thicker.

Figure 3.14 shows the effects of dead layer on the DQE at half the Nysquist Frequency and the Nyquist Frequency, for a larger number of energies. It can seen that as energy increases the DQE performance trends towards the values seen for the case with no dead layer. For 10nm dead layer the effects of dead layer have ceased to be noticeable at 10keV, while the 100nm layer has been overcome by 20keV. The effect of a 1000nm dead layer are significant across the whole of the energy range investigated. At lower energies there is a loss of efficiency, that is more severe with increasing dead layer thickness. There is also little difference between the two different spatial frequencies shown other than a scaling factor, indicating that the dead layer effects are frequency independent.

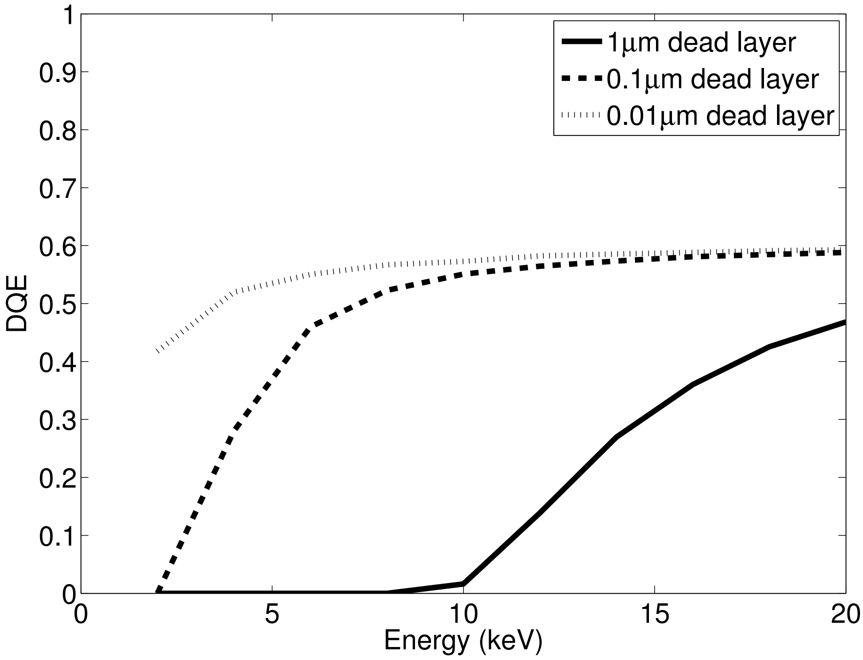

(a)

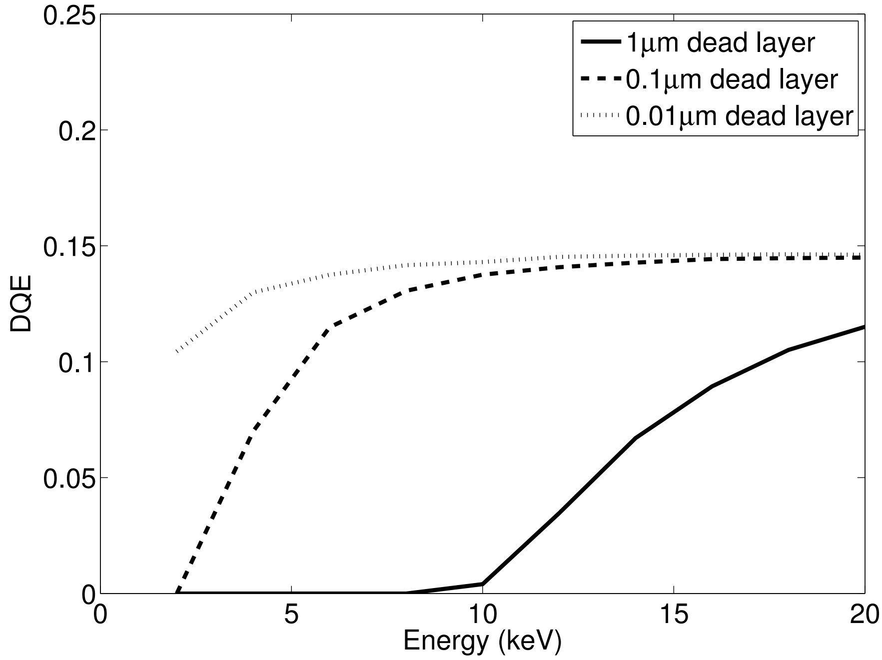

(b)

Figure 3.14: Variation of DQE with operating voltage for three differnt thicknesses of dead layer at (a) $0.25 pixel^{-1}$, (b) $0.5 pixel^{-1}$.

3.3.3 Discussion

The first observation is that the MTF shows little variation across the range of energies considered regardless of the dead layer thickness. From Figure 3.2 it has already been established that in this low energy regime there should be no MTF dependence on energy. This is due to the cluster size associated with these energies being much smaller than the pixel size, as illustrated in Figure 3.15, implying that there is only a minimal effect on the MTF below the Nyquist frequency. This lack of dependence on energy indicates that any differences observed are due to dead layer effects. As Figure 3.12 shows no change in the MTF, this implies that the dead layer does not effect the MTF. The exception to this is when the dead layer is sufficiently thick that no electrons can reach the sensitive layer.

Figure 3.4 shows that over this energy range that DQE should be independent of energy, so differences in this parameter can be attributed to the dead layer. From the calculations two main features can be identified; firstly that increasing energy reduces the detrimental effect of the dead layer and secondly that thicker dead layers have a more significant effect that is harder to overcome at all energies considered. Both of these properties can be related to the effective gain of the detector. When a dead layer is comparable to the penetration depth of an electron at a given energy it leads to a reduced gain as a proportion of the energy is deposited in the dead layer and does not give rise to any signal. When the amount of signal collected is reduced, this leads to a poorer signal to noise ratio. Furthermore as the energy is increased or the dead layer thickness is reduced, the ratio of dead layer thickness to penetration depth is also reduced leading to increased efficiency.

From the data in Figure 3.14 a generalised formula for the minimum operating voltage for a given dead layer can be estimated. The results show that the minimum voltage for a 0.1μm dead layer is approximately 2kV, while for a 1μm dead layer the voltage is approximately 10kV. An empirical approximation of the penetration depth is $x = \frac{0.1E^{1.5}}{\rho}$ [74]. This empirical formula slightly overestimates the penetration

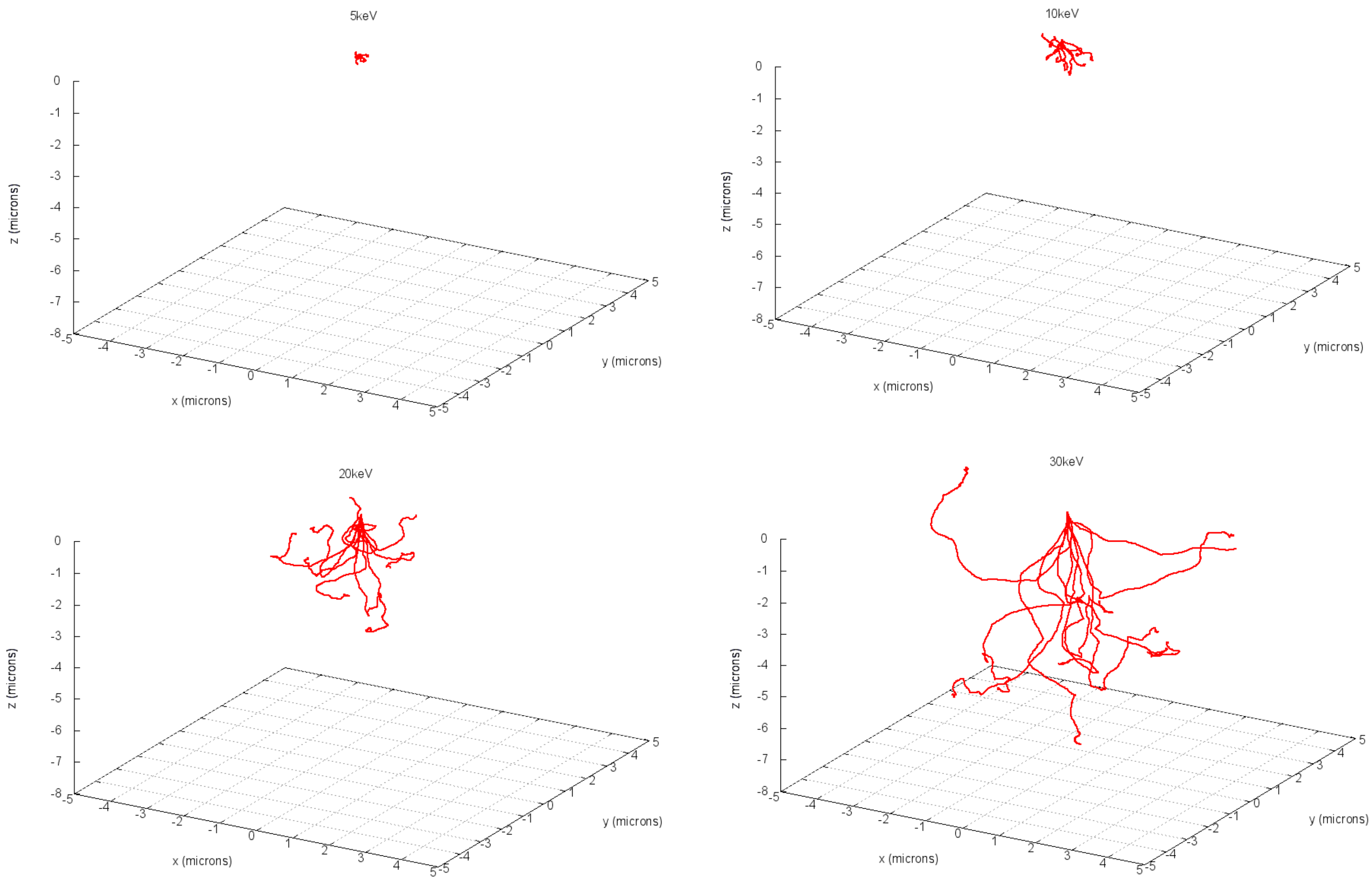

Figure 3.15: Trajectories of electrons though a Si detector, for (a) 5keV, (b) 10keV, (c) 20keV and (d) 30keV primary electron energy.

depth compared to our observations, as the factor of 0.1 is an approximation. However assuming the $E^{1.5}$ dependence and substituting in the density of Si, the formula $x = 0.035E^{1.5}$ fits the calculated data well. Making the assumption that the minimum operating voltage where some signal is detected is the point at which the penetration depth equals the dead layer thickness, gives $E_{min} = 9.8T^{\frac{2}{3}}$. While this estimates a minimum working energy, it is clear that the dead layer effects still have an important effect at many times this energy.

3.3.4 Conclusions

This section has examined the importance of dead layers for low energy direct detection of electrons. It has been shown that a dead layer can significantly alter the detection performance at low energies. The results show that dead layer effects are critically important in the <20keV region used for EBSD and that dead layers with a thickness typical of those found in traditional mechanically thinned devices have a significant effect. This suggests that reducing the dead layer thickness through improved thinning techniques will result in noticeable improvements, as will be shown in the experimental data presented in Section 4.3.

3.4 Diode Depth Effects

3.4.1 Introduction

In the previous sections it was assumed that the entire thickness of the detector experiences the electric field of the collection diode. In this situation all electron hole pairs generated will undergo drift under the influence of the field leading to efficient charge collection. However fabrication of deep diodes in CMOS processing is prohibitively expensive due to the high cost of fabricating non-standard CMOS structures. Standard structures can be used, however this means using diodes which do not fully penetrate the detector thickness. Standard structures reduce the cost of fabrication as the behaviour and process is understood, removing a substantial number of design and testing steps. However, this means that for many detectors the assumption of full well depth is not valid. In regions where there is no electric field, there is no drift, however electrons can still diffuse through the material and if they subsequently enter a region with an electric field then signal can be collected.

3.4.2 Theory

To model this effect the detector was treated as having two layers, a layer where drift is the dominant mechanism and electrons are always detected in the pixel in which they are generated and a diffusion layer where there is no drift. This is an oversimplification of the problem as the electric field in the pixel has a complex form dependent on the dopant profile. However this simplification makes the problem solvable and provides useful general insights. The first thing to consider is the diffusion length of an electron within the diffusion layer. This movement of an electron in the diffusion layer can be described as a 3D random walk with variable step size, for which the root mean squared displacement of a random walk is given by equation 3.1.

$$x_{rms} = \sqrt{6Dt} \tag{3.1}$$

D, is the diffusivity of electrons in silicon, and t, is the time elapsed following the generation event. The electrons of interest are those which reach the drift layer before a recombination event. The mean time to a recombination event is set by the minority carrier lifetime of electrons, τ. The lifetime of minority carriers depends on the concentration of majority carriers, which in turn depends upon the dopant concentration. At normal detector operating temperatures dopant atoms are fully activated so the majority carrier concentration is equivalent to the dopant concentration. For the wafers used to produce the direct detector studied (described in Chapter 5), the resistivity

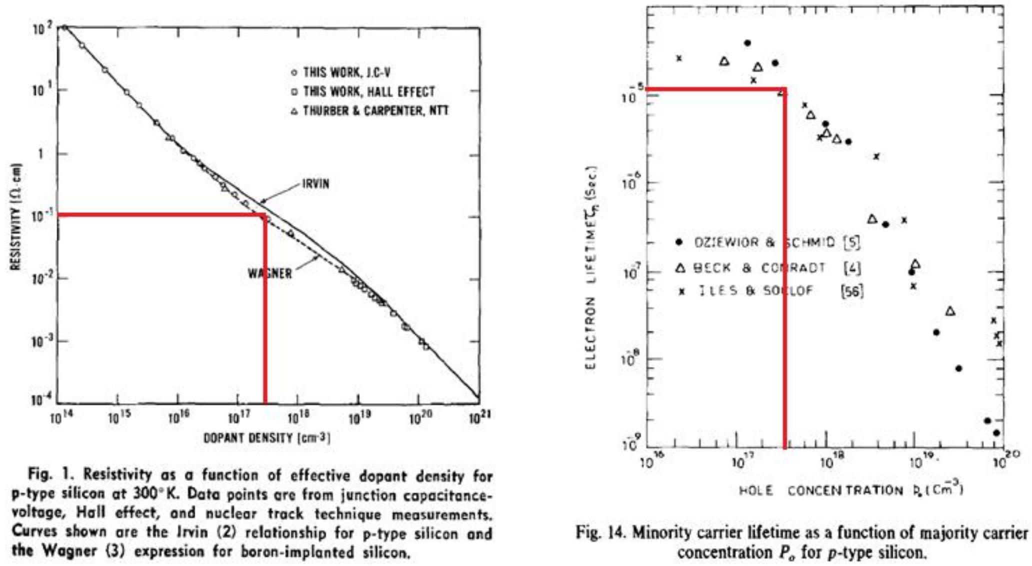

Figure 3.16: Relationship between resistivity and dopant density, and majority carrier concentration and minority carrier lifetime of p-type, boron doped silicon. Reproduced from [75] and [76] respectively.

of the substrate is $0.1\Omega m$, which corresponds to a dopant concentration of approximately $2\times10^{17}\text{cm}^{-3}$ [75], which in turn corresponds to a minority carrier lifetime of 10^{-5}s [76]. Graphs giving these conversions are shown in figure 3.16. Substituting into equation 3.1 gives a diffusion length of 424μm, which is much larger than both the pixel size and the detector thickness of interest.

Initially the assumption will be made that the diffusion length is much larger than the distance required to reach the sensitive layer. It is also assumed that as long as the

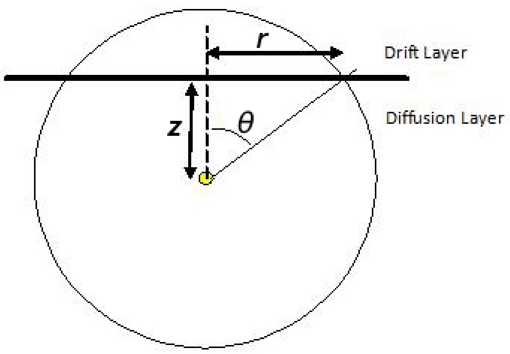

Figure 3.17: Schematic showing the parameters z, the generation event depth, r, the lateral displacement of detection and θ, the angle between the normal and the detection position.

net direction of travel is towards the sensitive layer then the electron will be detected. This assumption makes it possible to derive a probability density function of detection for a given lateral displacement, r. Figure 3.17 shows schematically the definitions of the parameters r, z and θ. The probability of detecting an event within a lateral distance r, of the impact point can be calculated by finding the surface area of the spherical cap at an angle θ, as a proportion of the total surface area. Expressing θ in terms of r and z and differentiating the function with respect to r gives the probability density with respect to r, at a depth of z.

This derivation is shown in equations 3.2-3.6,

$$T = \frac{2\pi\big(1-\cos(\theta)\big)}{4\pi} \tag{3.2}$$

$$\theta = \arctan\left(\frac{r}{z}\right) \tag{3.3}$$

$$T = \frac{1-\cos\big(\arctan(\frac{r}{z})\big)}{2} \tag{3.4}$$

$$T = \frac{1}{2}\left(1-\frac{1}{\sqrt{1+(\frac{r}{z})^2}}\right) \tag{3.5}$$

$$P(r;z) = \frac{dT}{dr} = \frac{r}{2z^2(1+(\frac{r}{z})^2)^{3/2}} \tag{3.6}$$

Using simple geometry it is trivial to show that the distance from the generation position to the detection position is given by $s = \sqrt{(r^2+z^2)}$. This implies that the finite diffusion length can be accounted for, as given in equation 3.7;

$$P(r;z) = \mathrm{F}\left(\sqrt{r^2+z^2}\right)\frac{r}{2z^2(1+(\frac{r}{z})^2)^{3/2}} \tag{3.7}$$

Where $F(x)$, is the Cumulative Distribution Function (CDF) of the fraction of electrons which diffuse further than a distance x, in this case the diffusion length to reach the drift layer at a displacement of r. To evaluate F, the diffusion distance, S, defined as $S = \sqrt{x_1^2+x_2^2+x_3^2}$ is considered where x_i are the displacements in Cartesian coordinates. This implies that the total displacement is the root of the quadrature sum of three independent variables. Extrapolating the expression for a 1D random walk, it can be shown [77] that the probability density function of the displacement of a diffusing particle at time t, $p(x;t)$, is a Gaussian with $\mu = 0$ and $\sigma = \sqrt{2Dt}$, which shows that S is the root of the quadrature sum of 3 independent variables with normal distributions. Therefore S exhibits a Chi distribution with three degrees of freedom (χ_3), which is a Maxwell distribution with a scale parameter $\sqrt{2D\tau}$. Using the standard result for the CDF of this distribution and given that the proportion of electrons which exceed S is required, shows that $F(x)$ is the function described by equation 3.8.

$$F(X;\sqrt{2D\tau}) = 1 - \left(\mathrm{erf}\left(\frac{X}{\sqrt{4D\tau}} \right) - \sqrt{\frac{2}{\pi}} \frac{X \exp\left(\frac{-X^2}{4D\tau} \right)}{\sqrt{2D\tau}} \right) \tag{3.8}$$

The difference between this full treatment of the problem and the thin detector assumption is shown in Figure 3.18, which shows the probability density function for electrons generated at 50μm and 250μm. This result shows that the simplifying assumption is valid for thin detectors, with only a very small difference. However as the thickness increases the distance factor becomes extremely important.

Applying the thin detector assumption is useful as it makes it easier to find the mixture distribution of the system, defined by equation 3.9.

$$P(x) = \int_A w(a) P(x;a) da \tag{3.9}$$

This equation describes the probability distribution for system which has a probability density dependent on a parameter, a, which itself is a random variable with a probability distribution, $w(a)$. The thin detector assumption makes the integration much simpler, meaning that the probability distribution for a given detector can be found. I now consider the simplest electron trajectory (a straight trajectory, with an equal generation probability at all depths). This type of trajectory is close to that for a high energy electron passing through a thin detector where the trajectories are relatively straight and where the electron only loses a fraction of its energy meaning the

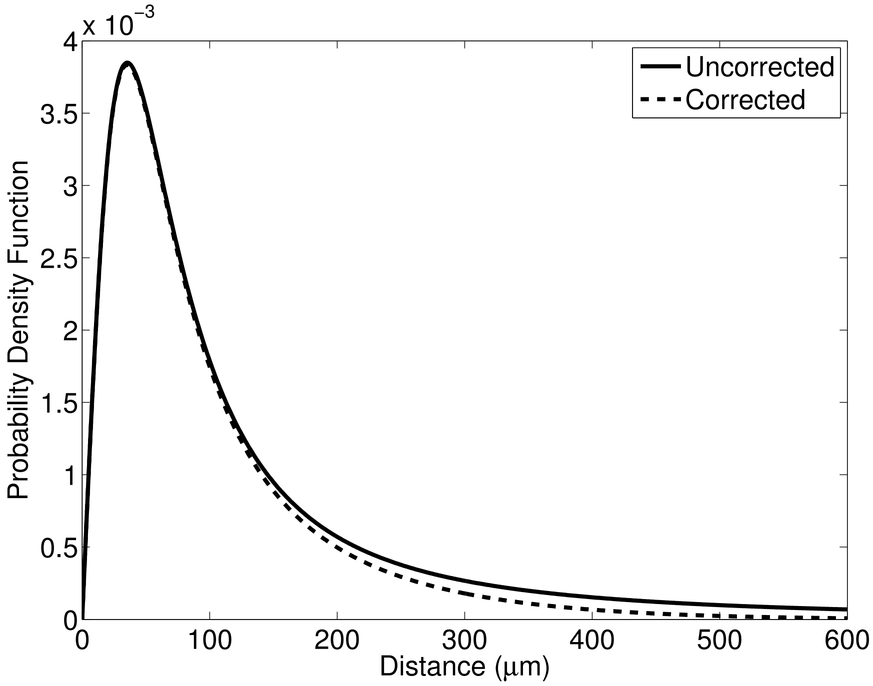

(a)

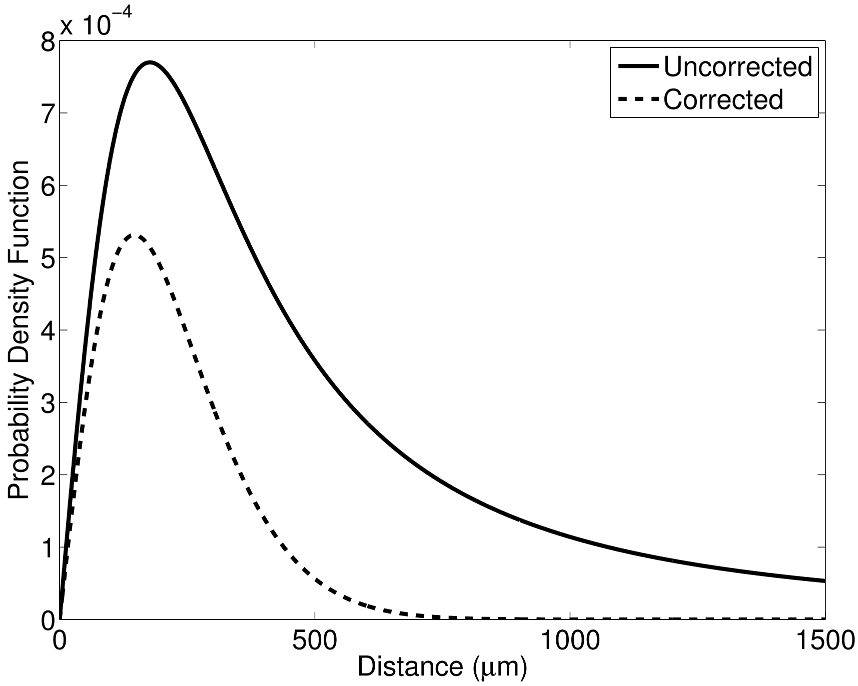

(b)

Figure 3.18: Probability density function for detection positions of diffusing electrons generated at (a) 50μm and (b) 250μm below the drift layer.

rate of signal generation is almost constant.

In this situation the full probability distribution is described by equations 3.10-3.13 which deal with signal generated entirely in a diffusion dominated layer.

$$w(a) = \frac{1}{T} \tag{3.10}$$

$$P(r) = \int_0^T \frac{1}{T} \frac{r}{2z^2(1+(\frac{r}{z})^2)^{3/2}} dz \tag{3.11}$$

$$P(r) = [-\frac{1}{T}\frac{r}{2}(z^2+r^2)^{-\frac{1}{2}}]_0^T \tag{3.12}$$

$$P(r) = \frac{1}{2T} - \frac{r}{2T\sqrt{T^2+r^2}} \tag{3.13}$$

To model a detector as a sensitive layer with both diffusion and drift regions an equivalent set of equation as given in 3.14-3.18 can be derived.

Initially the probability distributions at a given depth for the two different layers is identified as;

$$P(r;z) = \begin{cases} \delta(r), & \text{if } z \leq D \\ \frac{r}{2(z-D)^2(1+(\frac{r}{(z-D)})^2)^{3/2}}, & \text{if } z > D \end{cases} \tag{3.14}$$

Subsequently the mixture distribution is set up to yield the probability distribution for the whole detector;

$$P(r) = \int_0^T \frac{1}{T} P(x;z) dz \tag{3.15}$$

$$P(r) = \frac{1}{T}\left(\int_0^D \delta(r) dz + \int_D^T \frac{r}{2(z-D)^2(1+(\frac{r}{(z-D)})^2)^{3/2}} dz\right) \tag{3.16}$$

Using the substitution $x = z - D$, gives;

$$P(r) = \frac{1}{T}\left(D\delta(r) + \int_0^{(T-D)} \frac{r}{2x^2(1+(\frac{r}{x})^2)^{3/2}} dx\right) \tag{3.17}$$

which evaluates to;

$$P(r) = \frac{1}{T}\left(D\delta(r) + \frac{1}{2}\left(1 - \frac{r}{2\sqrt{(T-D)^2 + r^2}}\right)\right) \tag{3.18}$$

Where δ is the Dirac delta function, T is the full thickness of the detector and D is the thickness of the drift layer.

3.4.3 Results and Discussion

The solution to equation 3.18 for different thicknesses of detector with different depths of electrical field clearly shows the detrimental effect of not having the electric field extending throughout the detector thickness. The spreading effect due to diffusion can be incorporated into the model as a convolution of the diffusion spread function with the zero diffusion case, in which case the MTF dependence of a detector as a function of the diode depth is simply given by multiplication of two Fourier transforms, as described by equations 3.19 - 3.20.

$$I_p(x,y) = I_0(x,y) \otimes \mathrm{PSF}(x,y) \otimes \Pi(x,y) \otimes P(x,y) \tag{3.19}$$

$$\mathrm{MTF}(u,v) = |\mathscr{F}(\mathrm{PSF}(x,y))| \cdot |\mathscr{F}(\Pi(x,y))| \cdot |\mathscr{F}(P(x,y))| \tag{3.20}$$

Figure 3.19 shows the results for a 20μm and 50μm sensitive layer. The MTF was modelled at 300kV to show how the diode depth affects the MTF, as this voltage most closely resembles the assumptions made about signal deposition in the detector being equally distributed along a straight trajectory.

These results confirm that the diode depth is an important factor in detector performance and that the effects due to diode depth are non-linear. When the diode depth is close to the detector thickness, the performance remains unchanged. However, when the diode depth is 60% of the full thickness of a 50μm detector, there is a 10% reduction in the MTF at the Nyquist Frequency. As the diode depth is further reduced the rate at which the MTF is reduced becomes faster; when the diode depth is 10% of the detector thickness there is a 70% reduction in the MTF at the Nyquist frequency compared to the zero diffusion case. This is due to two factors which become important as the diode depth is reduced. The first is that as the diode depth is reduced, a larger proportion of the signal generated is dependent on diffusion effects. Secondly as the diode depth is reduced the effect of diffusion becomes more severe, as the distance to the drift layer is longer and hence more lateral displacement will occur.

There are some limitations to this model, particularly when dealing with lower energy detection where electrons do not pass through the detector and the assumption of uniformly deposited signal along a straight trajectory is invalid. To improve the model a more accurate treatment of both of these assumptions is required. To tackle the problem of non-uniform deposition the Bethe equation (Equation 2.9) could be used to

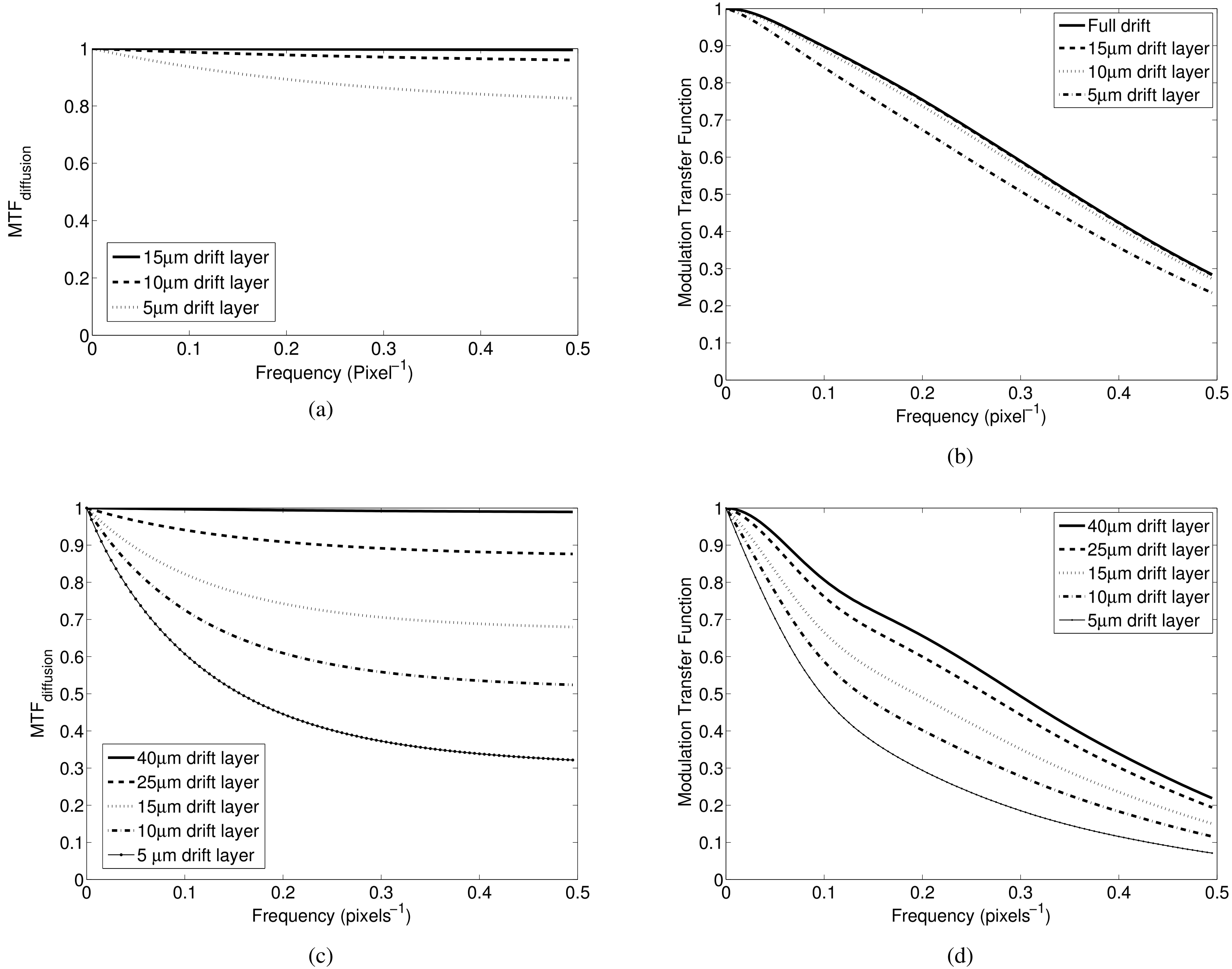

Figure 3.19: The effects of diode depth on detection performance. Fourier Transforms of the diffusion spread functions are shown for (a) 20μm and (c) 50μm thick detector with a range of drift layer thicknesses for 300keV electrons. (b) and (d)show the corresponding resulting MTFs.

calculate the rate of energy disposition as a function of depth and this used to calculate the weighting function. The problem with this approach is that it still assumes straight trajectories. A more complete treatment would require the addition of steps to model diffusion within a Monte Carlo process, finding a direction and a diffusion length according to appropriate distributions and using the detection position, if an event is detected in the calculation of the MTF. A full Monte Carlo treatment would also solve problems with the assumption that the combined effect of diffusion and other blurring processes can be evaluated as a convolution of the two individual effects. Whilst this model is a useful first step to understanding the process, the validity of the assumption must be questioned due to the fact that signal generated at large depth is responsible for blurring in both effects. At large depths the trajectory of the electrons are longer meaning there has been more lateral scattering and hence the diffusing electrons will reach higher displacements for a given net direction of travel. This interdependence of the two effects would suggest that a convolution is a simplification.

3.4.4 Conclusions

In this section I have developed theoretical models to account for the effects of the electric field of pixel diodes not fully penetrating the sensitive layer of the detector and the resulting effects of minority carriers diffusing through lightly doped material into charge collection diodes to generate signal. This treatment indicates that this can have a significant effect on detection performance. I have also identified a number of assumptions that need to be improved to produce a more complete treatment of the problem. Specific areas of further development that require attention are the depth profile of charge generation, the integration of diffusion effects within the model and a more accurate model for the electric field rather than simply splitting the detector into two distinct regions, one fully dependent on drift and one fully dependent on diffusion.

Chapter 4

The DUOS Sensor

4.1 Introduction

The DUOS sensor is a prototype directly illuminated electron detector originally designed for optical applications [78]. The sensor consists of 1024 x 1024 pixels with each pixel measuring 20μm x 20μm with a maximum readout speed of 28 frames/s at full field. This chapter introduces the different post CMOS processing routes by which different thicknesses of sensor have been produced and the two different sensor orientations that can be used. Results from the use of the detector for EBSD applications are also described, that examine how damaged layers arising from the mechanical thinning process effect detection efficiency and how a RIE process can be used to reduce the thickness of the damaged layer to improve efficiency.

4.2 Post CMOS Processing of the DUOS Sensor

4.2.1 Introduction

The DUOS sensors were received as wafers which had been mechanically thinned to 50μm using a commercial process. The wafers contain multiple sensors and different processing routes can be carried out on different sensors to produce different thicknesses and orientations. As received from the CMOS foundry there are two different wafer types. One batch of sensors was produced on epi silicon wafers consisting of a p-type wafer with the CMOS elements fabricated in an epitaxial layer of silicon. These sensors were primarily used in the mechanically thinned process. The other batch of sensors were fabricated on SOI (silicon on insulator) wafers. SOI wafers have three layers, a thick supporting silicon layer (handle wafer) and a thinner device layer of silicon separated by a thin silicon oxide layer. These wafers were used to produce chemically thinned sensors, as described in detail later in this section. Once thinned to the desired thickness the sensors were sent for die attachment and wire bonding to make chip on board assemblies (COB). Two PCB designs were used for imaging sensors. The front side illuminated geometry is one where the side of the sensor with the CMOS metalisation faces the source and back side illuminated geometry where the substrate side of the sensor faces the source. For a traditional thick sensor only front side illumination would be viable as a thick substrate effectively shields the sensitive layer from the radiation. However with a suitably thin detector, radiation can pass directly into the sensitive layer rather than having to pass through the various CMOS process layers improving low energy performance. Figure 4.1 summarises the processing route from wafer to device. In this work the two processing routes are referred to as mechanically thinned and chemically thinned respectively according to the method of thinning by which the sensitive layer is reached.

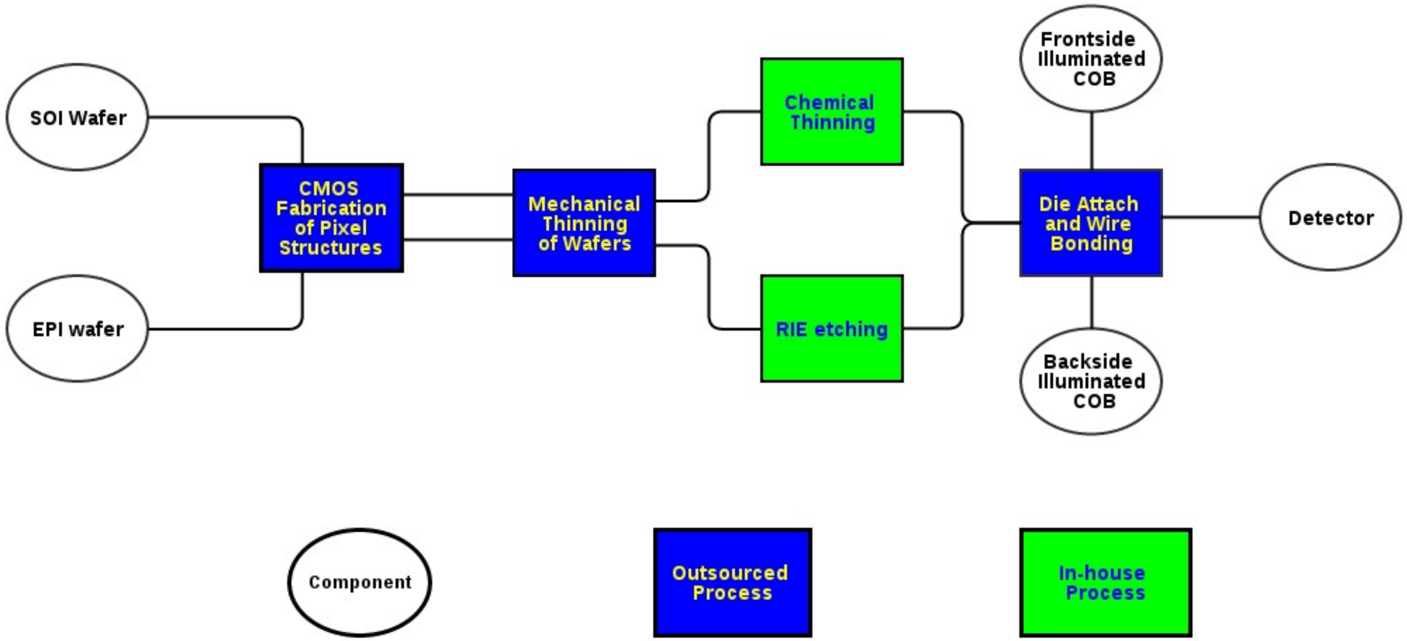

Figure 4.1: Processing route for the DUOS sensor.

4.2.2 Mechanically Thinned

In Chapter 3 the effect of an electrically dead layer on low energy detector performance was investigated. Initially sensors from an epi wafer were fabricated into detectors directly after mechanical thinning to 50μm. Sensors were mounted on both front illuminated and back illuminated COBs. The Front illuminated sensors were designed for use in TEM work while the back illuminated sensors were used for both TEM and EBSD work.

In low energy EBSD experiments, it was observed that the efficiency of mechanically thinned detectors was very poor, which was attributed to a thick layer of electrically damaged silicon. This is consistent with the prediction that the damage arising from mechanical thinning leads to an extremely high concentration of recombination centres and hence any signal generated in the surface region is not detected. Therefore, to improve the performance a process for reducing the thickness of the damaged layer is required. The method chosen was to use a reactive ion etch (RIE) to remove the damaged silicon. This leaves a much thinner damaged layer as the RIE affects a much shallower depth of material [79].

The RIE used a two step process, the first step removes the native oxide layer that forms due to the sensor being exposed to air for an extended period. Subsequently a high rate Si etch was used to remove the damage silicon. The conditions used for SiO_2 removal were a 5 minute process under an environment of 5:1 CHF_3 to C_2F_6 at 140Torr and 200V. To remove the damaged Si a 3 minute etch under an environment of 1:3 O_2 to SF_6 was used. The RIE process can be carried out before or after the die attach and wire bonding of the sensor to form a chip on board assembly (COB). However, if the RIE is carried out after die attach and wire bonding, steps must be taken to shield the PCB from the plasma. In this work scrap silicon was used, but this resulted in a shadowing at the edges of the sensor where no material was removed, reducing the usable sensor area.

4.2.3 Chemically Thinned

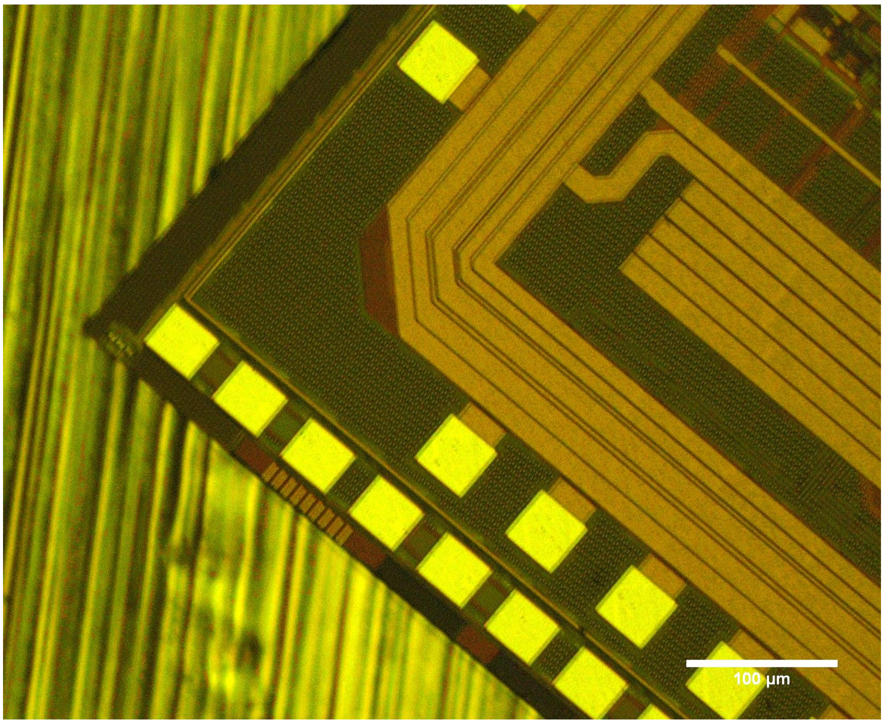

Figure 4.2: Optical image of the sensor prior to processing.

The rationale behind developing a chemical thinning process is that it can produce sensors with an improved surface finish due to this process being less destructive. However, it was also advantageous in producing a 20μm thick sensor. It was found that thinning directly to 20μm using a mechanical process gave sensors that were virtually impossible to remove from the film used to support the wafer during the thinning process. Recent advances in commercial mechanical thinning mean thicknesses of 20μm can be more easily achieved, however the chemical thinning process proved a convenient method for producing a 20μm thick detector for TEM and EBSD with less mechanical damage. For chemical thinning the sensors were fabricated on SOI wafers and the SOI wafer was selected such that the device layer equalled the final desired device thickness. After CMOS processing the support wafer was removed using chemical etching. The wet etch tetra-methyl ammonium hydroxide (TMAH) was selected as it has a good etch rate for Si but does not etch SiO_2. Hence when the etch reaches the insulator layer of the SOI wafer no further etching occurs. The insulating layer can then be removed using a selective RIE which only etches the oxide. For this process a means of protecting the metalisation layers of the CMOS is required so that they are not damaged during the chemical etching process.

ProTEK® B3 [80] was chosen as the protective coating for the CMOS layers. This coating is a polymeric compound designed to protect device layers even when the etch time is long. Typically it is applied using a spin coating process and then baked on a hot plate. However as the work described here was carried out on individual sensors rather than full wafers, alternative methods for application were used. Two methods were investigated for application of the coating. The first was to stick the side to be etched to a small piece of aluminium foil with a photoresist acting as glue. This allows the protective B3 coating to be applied to the front and edges of the sensor without getting any on the back side of the sensor. However both aluminium and the photoresist used as a glue are etched by TMAH. The second method used was to paint the edges of the sensor to ensure they are coated while trying to minimise the amount of coating on the back of the sensor. The sensor was etched in TMAH at approximately 80°C and etching continued until the embedded oxide layer was reached.

This process was initially tested using sensors that had been broken during mechanical thinning process. After two hours of etching the broken sensors were inspected. The sensor processed using the aluminium foil showed two problems; firstly the photoresist used as a glue for the foil had not been properly removed, providing protection to small areas of the sensor backside, which could not be removed by acetone and plasma cleaning. Secondly, inspection of the corners showed rounding (Figure 4.3), indicating that the B3 coating had not protected the sensor edges. It is believed that this was due to the photo resist “glue” penetrating the side of the wafer and the B3 coating allowing the TMAH to attack this layer and circumvent the protective coating.

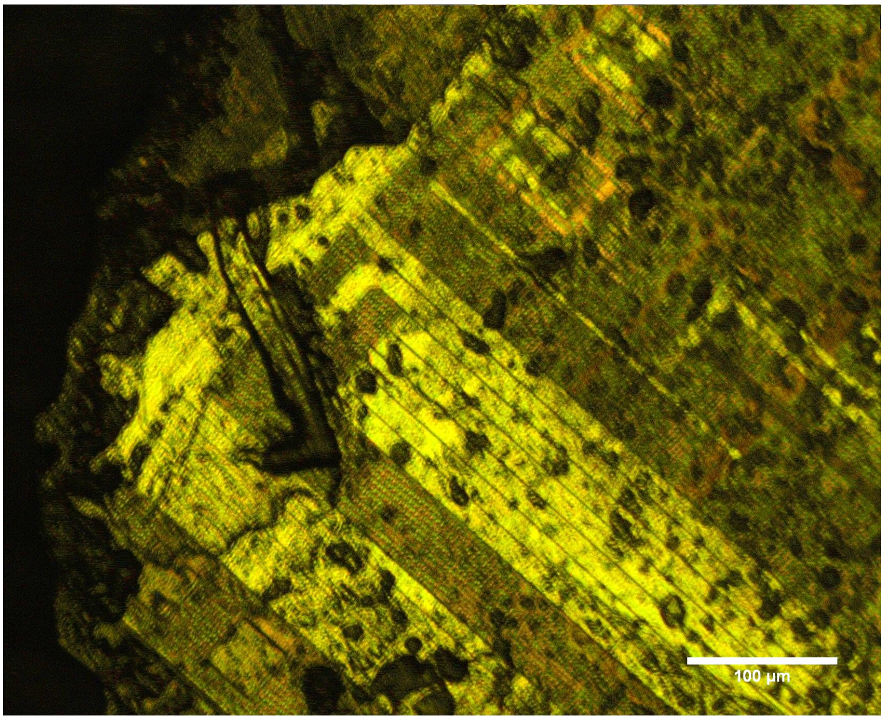

Figure 4.3: Optical images showing corner damage to the sensor using the Al foil protection route.

Painting the sensor edges also revealed problems. The first arose from curling of the sensor when it was removed from the hot etch and cooled. The process generates internal stresses in the pre-etched structure arising from both the lattice mismatch between the oxide and the Si and in ProTEK® B3 coating due to differences in thermal expansion coefficient as it cools down. When the supporting material is removed the Si becomes less rigid and the sensor curls to relieve these stresses. Initially removal of the oxide layer was attempted by dipping in hydrofluoric acid, as a RIE etch would have very different etch rates across the curled sensor. While this method successfully removed the oxide layer the HF caused the ProTEK® B3 coating to lift from the surface, most likely through rapid attack of the primer layer between the Si surface and the coating itself. This exposed the CMOS layers of the sensor to the acid causing damage, removing both the aluminium pads and copper tracks (Figure 4.4). While some of the coating attached to the back of the sensor during processing, this did not cause issues during the etching process, as the convex corners of an area protected by

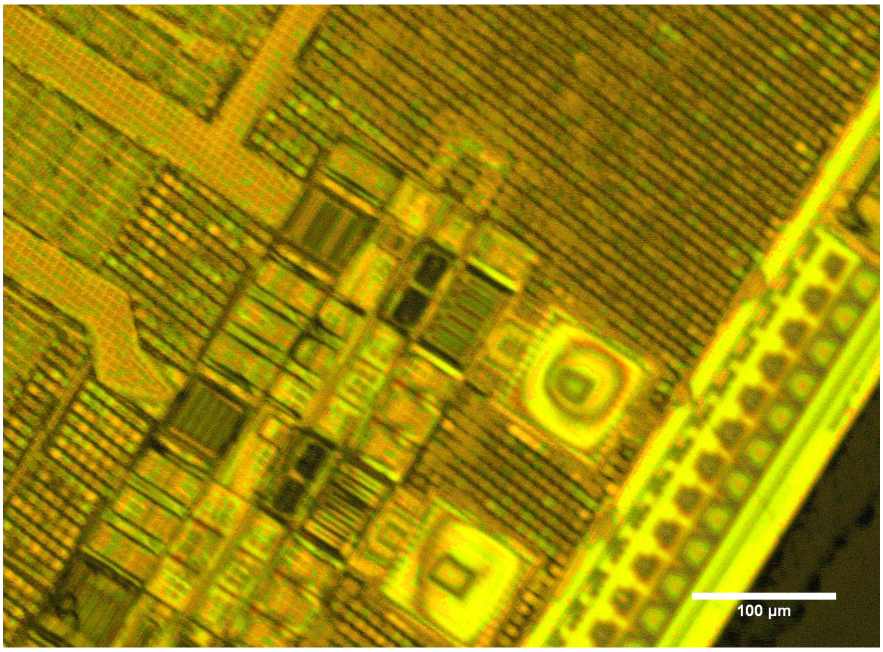

Figure 4.4: Optical image showing the sensor after being damaged by HF.

the coating were etched away quickly.

A second test sensor was processed by painting the edges and etching. After etching the ProTEK® B3 coating was removed using the commercial remover, a chemical bath which dissolves the coating. This reduced the curling of the sensor. The sensor was then inspected for damage and it was noted that there was a small area where a number of pixels had been damaged (Figure 4.5). This was attributed to a localised failure in the application of the B3 coating. This problem had also been observed in previous work using this chemical [81] and the solution proposed was to deposit the B3 coating twice to ensure a continuous coating with no imperfections.

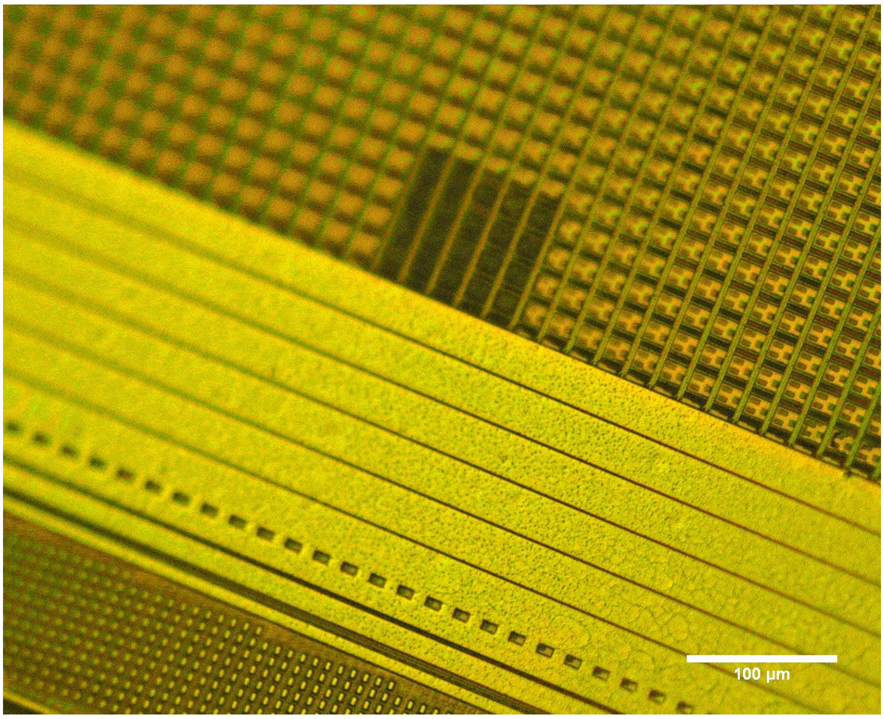

Figure 4.5: Optical image showing pixels damaged during the etching process.

The oxide was subsequently removed using a RIE process. A plasma of 5:1 CHF_3:C_2F_6 at 150V and a table temperature of 5°C was used to prevent excessive heating. The total etch time was around 90 minutes for the 1μm oxide layer. After 40 minutes the sensor was moved as there was still some curvature after removal of the B3 coating, preventing the sensor from lying flat and causing the corner closer to the plasma source to etch faster. The sensor was therefore moved such that the opposite corner was raised to balance the etch depth. Scrap silicon was used to hold down one corner to prevent the sensors being sucked into the vacuum system during evacuation and venting. After the etching process was complete the sensor was inspected and damage was observed on the surface near the corners that were raised due to the curling. The modification used to solve this was to remove the B3 coat after the oxide had been removed using a RIE. Due to the extra curling associated with a double B3 coating the protective coating was stripped and reapplied between the wet and dry etching steps. However, observation under an optical microscope after initial removal of the coating showed that there was still residue (Figure 4.6). A variety of methods were used in attempts to remove this, including argon plasma cleaning, oxygen plasma cleaning, 48 hours soaking in acetone and 48 hours soaking in the B3 removal agent. However, none of these methods removed the remaining residue and it is hypothesised that this was due to hardening of the B3 coating during the plasma etch of the oxide. To overcome this problem an AZ5214 [82] resist was used to protect the CMOS layers during RIE etching. Figure 4.7 summarises the final chemical thinning process used.

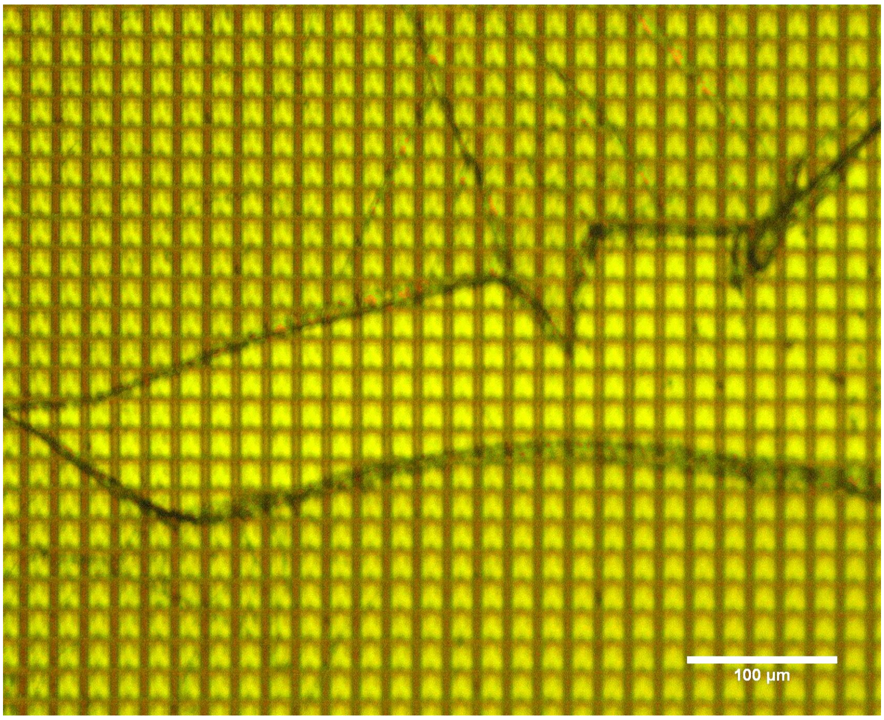

Figure 4.6: Optical image showing the front side of a sensor with residual coating following cleaning.

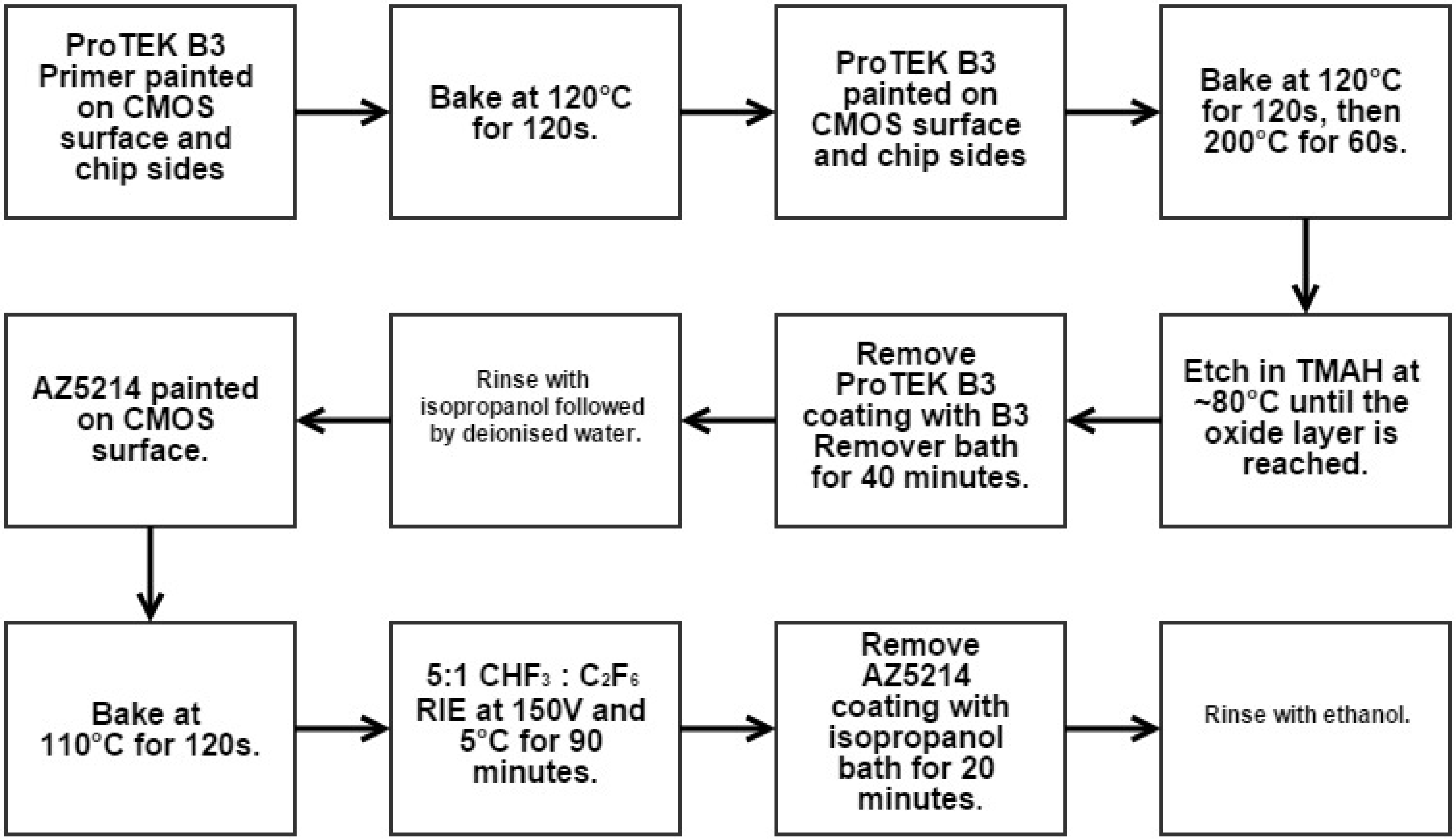

Figure 4.7: The final chemical thinning process.

4.3 Direct Detectors for Electron Backscattered Diffraction

4.3.1 Introduction

Electron Backscatter Diffraction (EBSD) uses signal collected in a scanning electron microscope (SEM) where the Kikuchi patterns from diffraction of secondary electrons leaving the sample are captured on a pixelated detector for each raster point. EBSD has a number of applications relating to crystal structure such as phase and orientation mapping [83]. More recent developments have widened the applications of EBSD to fields such as 3D reconstruction, where EBSD is used in conjunction with FIB sectioning to reconstruct orientation maps in 3D [84] and strain mapping, where strain is mapped through measurement of the changes to the EBSD pattern at different positions [85]. For this application higher precision in pattern recording gives a more accurate strain measurement. However, as research in EBSD has progressed, the detectors used have not changed and this has begun to limit performance. This section presents EBSD patterns taken from Si[001] on the DUOS detector before and after a RIE to reduce the dead layer thickness.

4.3.2 Experimental Details

The collection of the experimental data was done by Dr. Grigore Moldovan and the DUOS sensor used was mechanically thinned to 50μm thick and die attached in a back illuminated configuration making it suitable for low energy work. The detector was mounted vertically in the SEM column and EBSD patterns were collected from a Si[001] sample tilted at 70° from the incident beam towards the detector. Images were collected at 5kV, 10kV and 20kV and at each voltage 128 frames were collected so a range of exposure times could be explored by simply changing the number of frames used in a post-acquisition summation. Each individual frame had an integration time of 160ms giving a total exposure time of 20.5s. At 5kV the probe current was 8.9nA, at 10kV the probe current was 10.1nA and at 20kV the probe current was 9.2nA.

Initial inspection of the data showed poor efficiency at low operating voltages. This was consistent with expectations from the modelling of dead layers and hence the sensor was modified by using a RIE to remove the damaged surface layer of silicon, as described in section 4.2. The experiments were then repeated on the RIE treated sensor under the same conditions.

4.3.3 Results and Discussion

Figure 4.8 shows EBSD patterns generated at 5kV, 10kV and 20kV before and after the RIE process. While it is qualitatively clear that the use of the RIE improves performance, a quantitative measure of the SNR is desirable. To quantify the signal to noise ratio line profiles were taken across the regions marked in Figure 4.8. The line profiles were taken in the horizontal direction, averaging across the vertical direction and the resulting profiles are shown in Figure 4.9. The region was selected so that the profile crosses distinctive features in the pattern in this case the band associated with scattering from the (220) plane, which could be easily be identified on the different images at the same voltage. From the line profile the magnitude of the step associated with the edge of the (220) band is used as a measure of signal strength. This process cannot be carried out on the data collected at 5kV, recorded using the detector before etching, as no pattern is visible. To quantify the noise a dataset of values is generated by subtracting the pixel value from the value of the pixel above it i.e. $I'(i,j) = I(i,j+1) - I(i,j)$, and a Gaussian distribution is then fitted to the data. The rationale behind this method is that the changes between the underlying images are small, so that the differences which arise are primarily due to noise. The standard deviation of the normal distribution is hence used as a measure of the noise. Using this measurement the signal to noise ratio of the edge of the band was calculated and the results are summarised in Table 4.1. I note that this method for calculating the noise will tend to overestimate

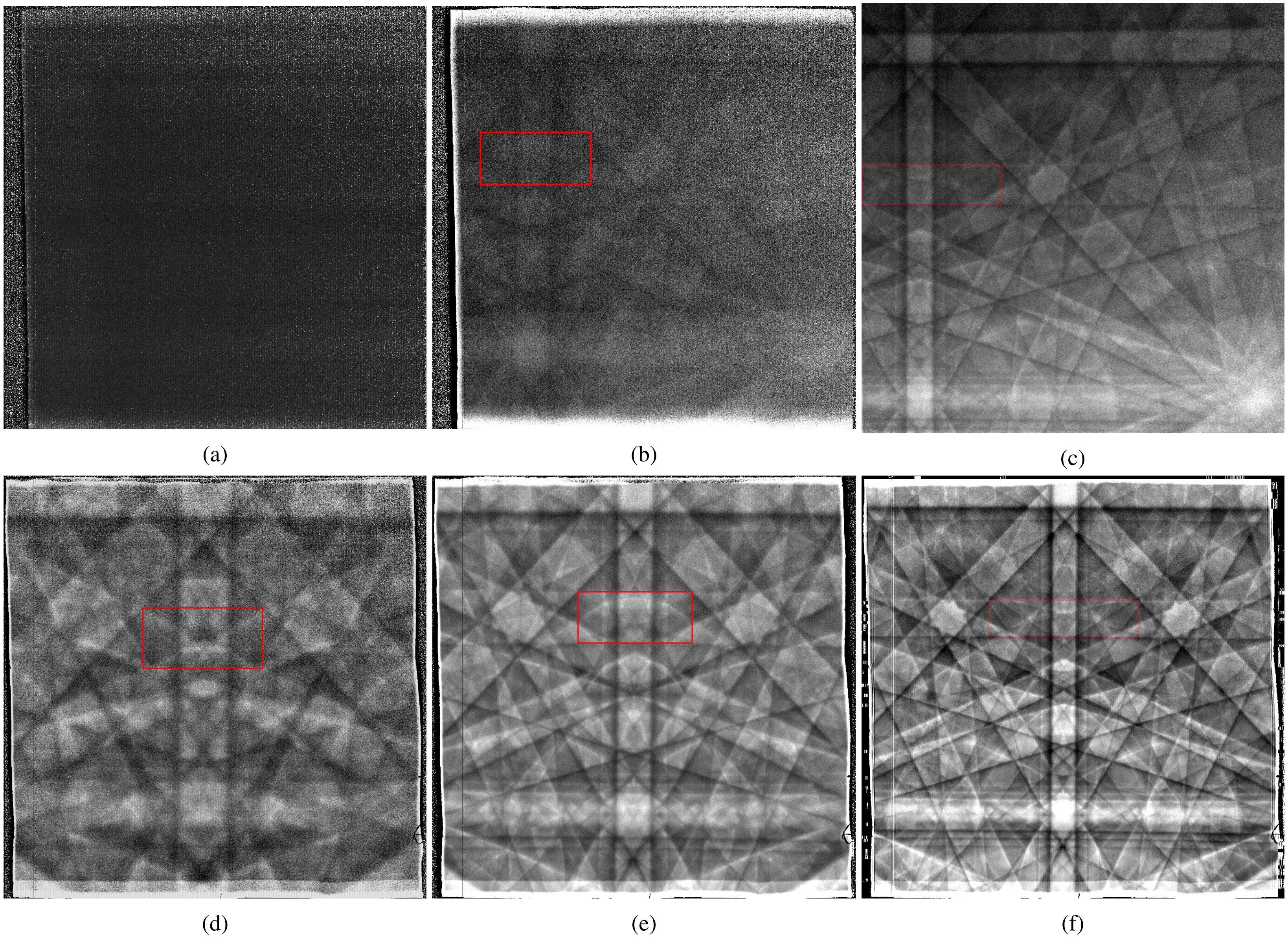

Figure 4.8: EBSD patterns of Si[001], (a) - (c) show EBSD patterns captured on the 50μm thick mechanically thinned detector at 5kV, 10kV and 20kV respectively. (d) - (f) show EBSD patterns captured on the mechanically thinned and RIE treated detector. Boxes indicate regions used to build line profiles.

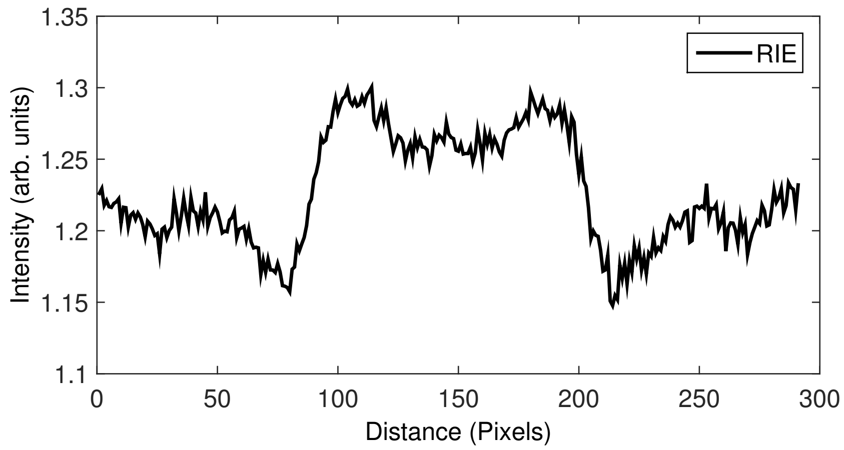

(a)

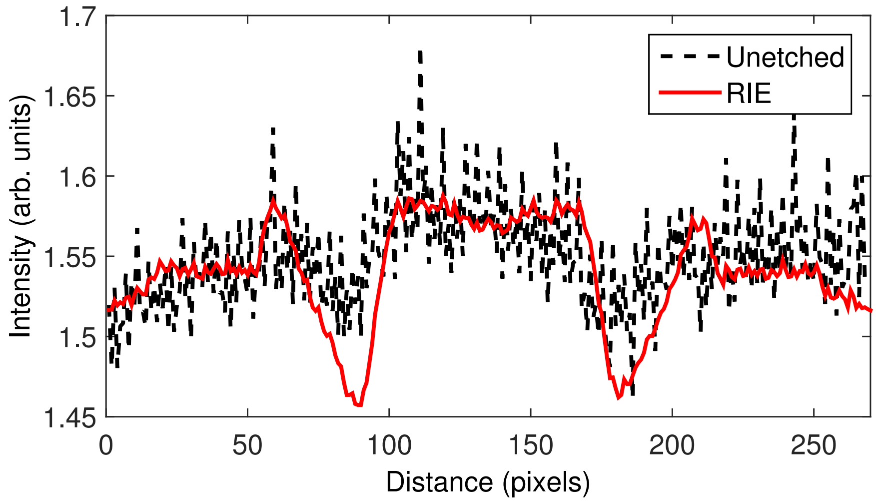

(b)

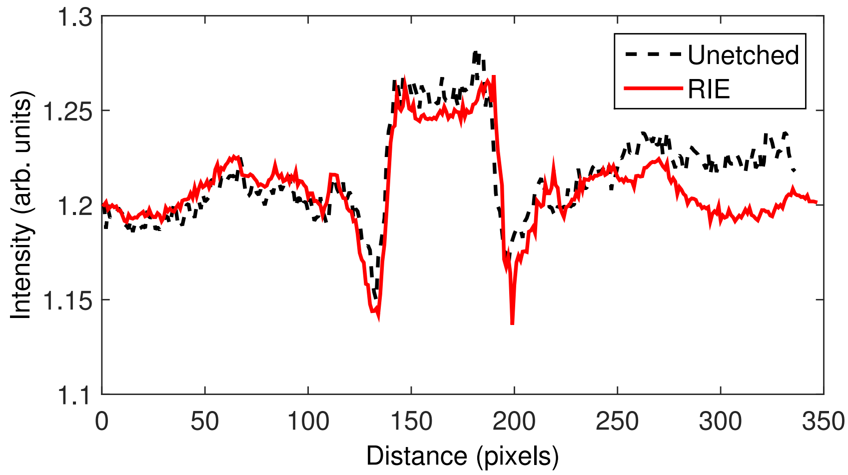

(c)

Figure 4.9: Line profiles extracted from the regions marked in Figure 4.8 at (a) 5kV, (b) 10kV and (c) 20kV operating voltage. The unetched sensor gives no measurable signal at 5kV.

Dataset	Signal	Noise	SNR
5kev unetched	0	0.6799	0
5keV etched	0.14	0.0864	1.62
10kV unetched	0.14	0.2056	0.68
10kV etched	0.13	0.0287	4.53
20kV unetched	0.18	0.0865	2.08
20kV etched	0.11	0.0199	5.5

Table 4.1: Measured signal to noise ratio of the edge of the (220) band, for different detectors and accelerating voltages.

noise to due to differences in pixel values arising from a changing signal. However, very large changes arising from sharp features are excluded from the fitting of the distribution by only taking the central part of the histogram.

The results are consistent with the modelled DQEs of detectors with dead layers presented in Chapter 3 (Figure 3.14). For the RIE treated sensor the SNR increases as the operating voltage increases, with a large improvement between 5kV and 10kV and a much smaller improvement between 10kV and 20kV. This is consistent with models of a 0.1μm dead layer. Comparing the lower voltage results to the result at 20kV it can be seen that the level of improvement is less than that found for a modelled dead layer thickness of 0.1μm indicating that the damaged layer is slightly thicker than this. Examination of the unetched results and in particular the lack of any pattern at 5kV is consistent with models for dead layers arising from the polishing process. However at 10kV and 20kV differences can also be seen when compared to the simulated result. As expected the SNR is significantly lower for the unetched case compared to the etched case. However, at 10kV the performance is better than would be expected for a 1μm dead layer but at 20kV the performance is worse than would be expected for a 1μm dead layer. The explanation for this is the simplification used in the model, which assumes a two layer system consisting of a perfect detection layer and a dead layer. In reality a sharp interface is not expected, but a more gradual transition, as shown schematically in Figure 4.10. At lower energies where the majority of signal is deposited in the dead layer in the model it is expected there will be an improvement in efficiency for the experimental case as signal will be detected which is lost in the model. In the case of the unetched detector this suggests that there is some signal detected that is generated at depths less than 1μm, but recombination centres arising from the thinning process are present significantly deeper than this. Direct comparison between the modelled DQE and the experimentally measured SNR provides a simple means of comparison. However the SNR measured is affected by changes in the input image while the DQE is not. For example any changes to the pattern arising from interaction with the sample at the higher operating voltage will effect the SNR but not the DQE. This inability to distinguish between detector and sample effects on the SNR means that accurate measurement of the voltage dependent effects on detector performance is limited.

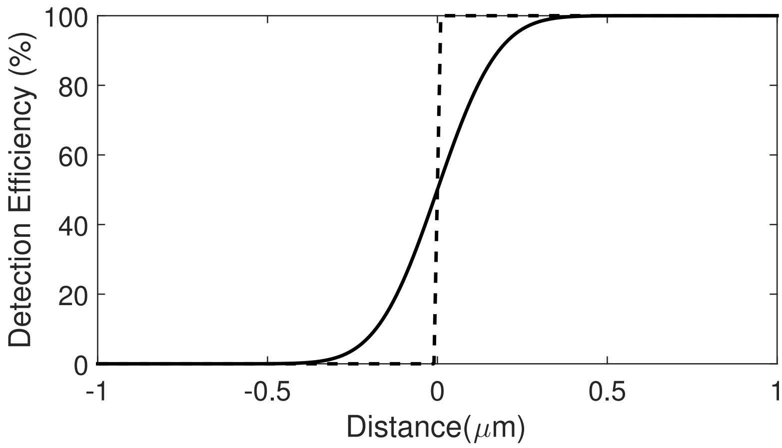

Figure 4.10: Schematic illustrating detection efficiency with depth for a diffuse interface.

4.3.4 Conclusions

In this section the improvement in efficiency of EBSD patterns recorded using RIE and mechanically thinned sensors has been described. This was carried out using measurement of the signal to noise ratio of the (220) band compared to simulated results for a detector with an electrical dead layer. The effects seen experimentally followed the patterns predicted from modelling, with thicknesses of dead layer consistent with those predicted.

Chapter 5

Direct Detectors for Transmission Electron Microscopy

5.1 Introduction

Direct detectors are of considerable interest for applications in Transmission Electron Microscopy due to their potential for higher resolution and improved sensitivity [56]. In this chapter I will examine a number of different aspects of the underlying technology. The effects of both thickness and operating voltage on detector performance will be presented. The DUOS direct detector (Chapter 4) used was characterised at 80kV and 200kV, with measurements of the MTF, NPS and DQE for sensor thicknesses of 20μm and 50μm. Images of gold nanoparticles on amorphous carbon show how the improvements in detector performance are translated to improvements in experimental data. I have also evaluated how these results match with detector simulations and discuss reasons for any differences. As direct detectors typically have a poor intrinsic dynamic range due to the large number of electron hole pairs generated by a primary electron, in integrating mode they are operated at a high frame rate so the dose/frame is low. Final images are then made from the summation of a large number of individual frames. The effect of registering the individual frames both rigidly and non rigidly before summation has also been investigated. Finally a characterisation of the commercially available DE-20 direct detector will be presented.

5.2 Effects of Detector Thickness and Operating Voltage on Performance

5.2.1 Introduction

Chapter 3 described how detector performance is affected by the thickness of the sensor and the microscope operating voltage using simulations of detector performance by Monte Carlo simulation of electron trajectories. In this section experimental data from detectors with different thicknesses, at different operating voltages demonstrates the practical improvement in detector performance using thin detectors.

5.2.2 Experimental Details

For the work described, the DUOS detector discussed in Chapter 4 was used. The detector was mounted on a JEOL 2200MCO TEM, a monochromated, double aberration corrected, omega filtered microscope [86]. Initial datasets were acquired by swapping the existing Gatan Ultrascan 4000 CCD [87] for the DUOS system. However subsequently a modification was made to the microscope by adding a second camera block below the Ultrascan 4000 block. This modification allowed switching between the two cameras without having to vent any part of the microscope. In this configuration the same part of a sample can easily be imaged by both detectors. In this prototype system, there was no shutter control in the detector software as the DUOS detector does not require a physical shutter. Instead, the microscope's physical shutter was controlled manually, by being opened shortly before the acquisition was initiated and using a longer shutter controlled exposure time than the acquisition time required for the dataset.

Experimental data was acquired using three different detectors, at two different microscope operating voltages. The three detectors were two different sensor thicknesses in the DUOS detector; a 50μm thick mechanically thinned sensor and a 20μm thick chemically thinned sensor. Production of these chips was described in Chapter 4. The third detector was the Gatan Ultrascan 4000 camera, a conventional indirectly coupled CCD detector used as a basis for comparison. Each detector was characterised at both 80kV and 200kV. The data for MTF, NPS and DQE measurements were collected using the following procedure;

- Images with the beam blanked were collected and averaged to generate a dark correction.
- Images with the beam stop inserted were collected for measurement of the MTF, with the beam stop acting as the edge required for MTF calculations described in Chapter 2.
- Images with uniform illumination were collected to apply a gain normalisation and for calculation of the NPS.
- Images of the full beam focused onto the detector were collected for calculation of the detector gain.

For each dataset 128 images were collected and the detector was operated at 30ms/frame, giving a total exposure of 3.9s. The detector was operated slightly below saturation by monitoring the live histogram of pixel values and spreading or condensing the beam until no saturated pixels were observed. To image the beam, steps had to be taken to reduce the intensity, as the detector easily saturates with a focused beam. In some cases it was sufficient to use the smallest condenser aperture available, however for the highest gain detectors this was insufficient and in these cases a slit in either the monochromator or omega filter was used to reduce the number of electrons in the beam. In theory the omega filter should not affect an image of vacuum as no electrons lose energy in the sample. However in practice it was found that with a 0.5eV slit, energy variations in the beam without monochromation were sufficiently large that the beam current was reduced to a useful level. For all measurements a Faraday cup was used to measure the absolute beam current.

To calculate the MTF, images with a beam stop had dark and gain correction applied, were cropped and rotated such that the straight edge was aligned from left to right across the whole width of the image. An unpublished plugin for ImageJ written by Grigore Moldovan (Appendix A.1) was used to produce a line profile across the edge. The edge profile was selected to be 30 pixels either side of the edge, with an oversampling of 8 achieved through combination of information from multiple rows. The length was chosen to ensure that any long range effects from electrons at a large lateral scattering are captured, while the oversampling ensures a good fit to the transitions. Three error functions of the form $a.\mathrm{erf}(bx+c)$, where c is the same in all three functions, were used to fit a function to the edge profile. It was observed that at least two error functions were required to accurately match the edge profile, which is more than was observed in previous work [2] due to some electrons passing through the detector in the case of thin detectors whereas in thick detectors all electrons deposit all their energy. Fitting three error functions using the curve fitting tool in Matlab [88], rather than by direct numerical manipulation of the data was preferable due to noise in the flat regions located away from the edge arising from Poisson noise in the bright region. This gave a noisy result and periodic “ADC noise” in the shadow region leading to false results, as the periodic noise gives a profile that is no longer a simple blurred step function. The “ADC noise” arises from the fact the DUOS sensor has four analogue to digital converters (ADCs), while in a normal image with low variation in pixel values the different gains of the individual ADCs can be corrected for by assuming each ADC has linear gain. However, in the case of an image used for calculation in MTF there is a very large difference in pixel values between those in the shadow region and those outside it. In this case the assumption of linear gain breaks down and the periodic noise between pixel columns can still be observed.

To calculate the NPS another ImageJ plugin (Appendix A.2) was used to implement the calculation detailed in Chapter 2. The results of the NPS are quite noisy particularly at low spatial frequencies due to the limited number of data points. To reduce noise when the NPS is used to calculated the DQE the curve fitting toolbox in Matlab [87] was used to fit a function as a summation of three Gaussians to the NPS data.

As all data was collected on the same microscope it was also possible to collect images which show how the different detector performances translate into differences in experimental data.

Images of gold particles on amorphous carbon were taken over a range of magnifications from 60kX to 250kX at doses of approximately 15 electrons/pixel and 80 electrons/pixel on the Ultrascan 4000 camera. A series of images were then captured using the DUOS detector. The exact dose was calculated using the Ultrascan images and for a single frame of the DUOS dataset. Finally a number of DUOS images were summed together such that the effective dose was the same as that in a single Ultrascan image. As the cameras were mounted on the microscope at the same time, the data for the 20μm thick DUOS detector and the Ultrascan 4000 camera were acquired at the same time, with the aberration correctors in the same state enabling direct comparison. However, the magnification of the DUOS camera had to be calibrated due to the different pixel size and camera length. Firstly, a particle was chosen such that it filled a high proportion of the DUOS detector's field of view. In the captured image two vertical lines were drawn such that one touched the left most part of the particle, while the other touched the right most part. The perpendicular distance between the two lines was then measured. The same distance was then measured on the Ultrascan camera, to give the change in distance represented by a pixel between the two detectors.

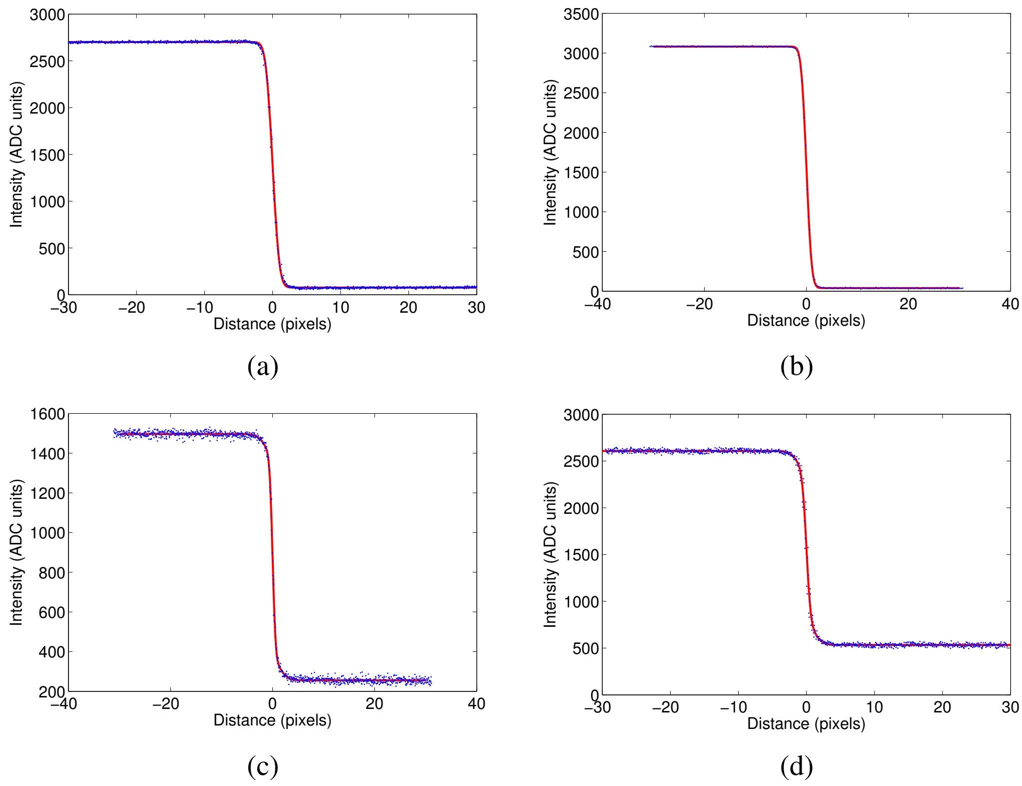

Figure 5.1: Line profiles and the fitted function used to calculate the MTF for the DUOS detector of a) 20μm at 80kV, b)50μm at 80kV, c) 20μm at 200kV and d) 50μm at 200kV.

5.2.3 Results

Table 5.1 shows the number of ADC counts generated by an individual electron for four different experimental configurations, in which there are significant variations in detector gain depending on the operating voltage and detector thickness. Figure 5.2a shows the MTF of the DUOS detector for the two different thicknesses at 80kV, and Figure 5.2b shows the MTF results at 200kV. In both figures the MTF of the Gatan Ultrascan 4000 camera has been included to offer a basis for comparison.

		Thickness	
		20μm	50μm
Voltage	200kV	112	283
	80kV	326	1290

Table 5.1: Average number of counts generated by a single electron for the set of DUOS detector thicknesses and microscope operating voltages investigated.

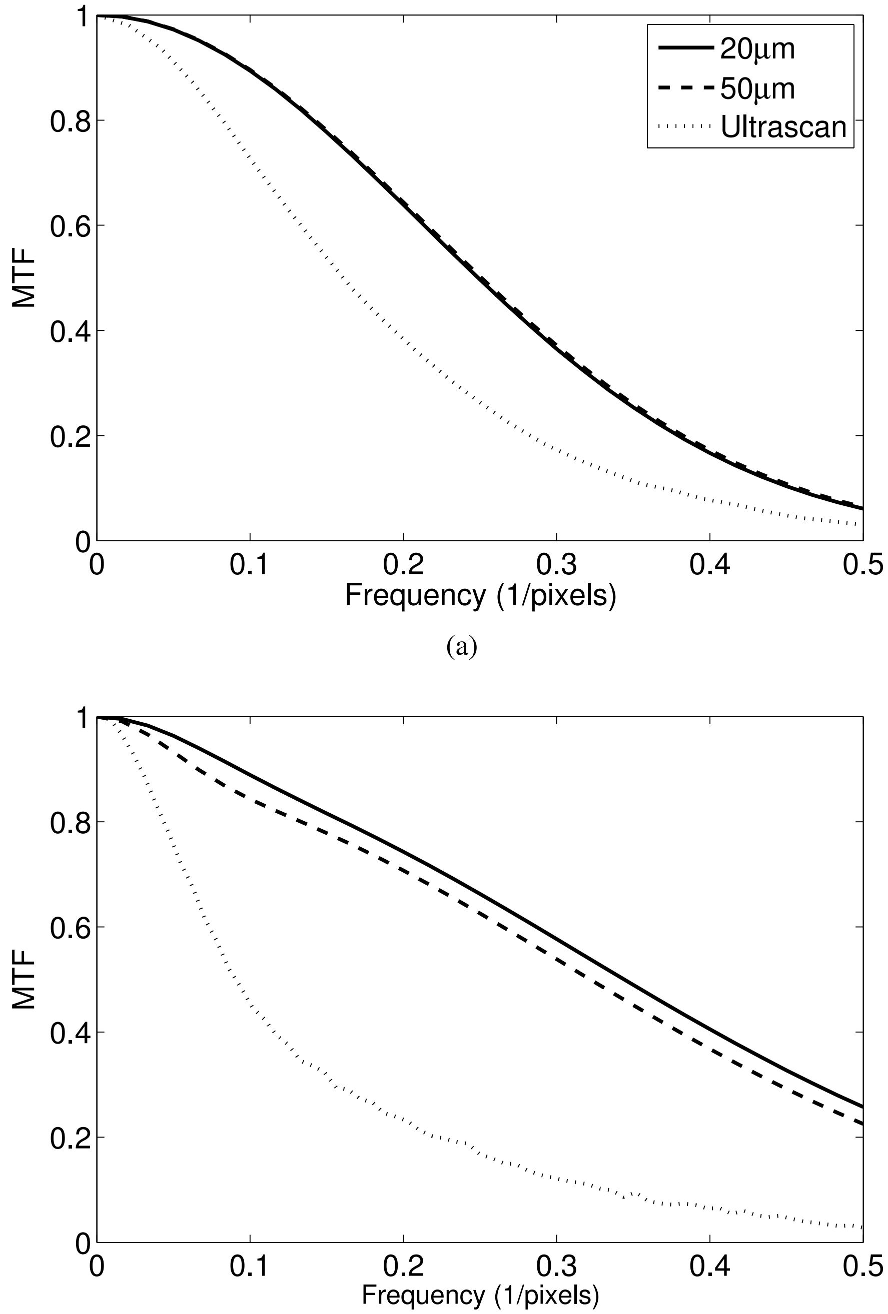

(a)

(b)

Figure 5.2: MTF for the two different sensor thicknesses of the DUOS sensor at operating voltages of (a) 80kV, (b)200kV. Corresponding results for the Gatan Ultrascan 4000 are included for comparison.

In Figure 5.2a the performance of the direct detector is improved relative to that of the indirect detector, but in this case there is no difference between the two thicknesses of DUOS detector. Figure 5.2b shows that the MTF for the 20μm thick DUOS detector outperforms the indirect detector across the full frequency range and the 50μm thick DUOS detector shows improved performance in the MTF up to spatial frequencies of 0.4pixels^{-1}. Comparison of the two different thicknesses shows that the thinner gives improved performance across the whole frequency range and at the Nyquist frequency the MTF of the thinner detector is approximately five times that of the thicker detector.

The DQEs shown in Figure 5.3a indicate that the thicker detector performs better, while Figure 5.3b indicate that the thinner detector outperforms the thicker detector. This general behaviour is expected given the dependence of the DQE on the MTF. However the other component of the DQE comes from noise. Figure 5.4 shows the normalised noise power spectrum (NNPS) for the four different direct detector experiments used to calculate the DQE. At 200kV, at lower spatial frequencies there is more noise in the thicker detector, but there is less noise above spatial frequencies of 0.4 pixels^{-1}. At 80kV the thicker detector is less noisy across all spatial frequencies.

Figure 5.5 shows the measured and simulated MTF and DQE for each thickness and voltage combination. Simulated results incorporating an additional Gaussian blur with a standard deviation of 10μm are also shown. The MTF results show a good match when the simulated result has been corrected with a Gaussian blur. However in the case of the thicker detector at 200kV there is a significant difference between the simulated and experimental results with the detector performing better than predicted at low spatial frequencies and worse at higher frequencies. The quality of the match is quantified in Figure 5.6 by plotting the function resulting from dividing the simulated MTF by the experimental MTF. It is clear with the exception of the 50μm thick detector at 200kV the deviation between the two functions is minimal. The DQE results at 80kV show poorer performance at low spatial frequencies, up to approximately 0.15pixels^{-1}. Above these frequencies the experimental performance is better

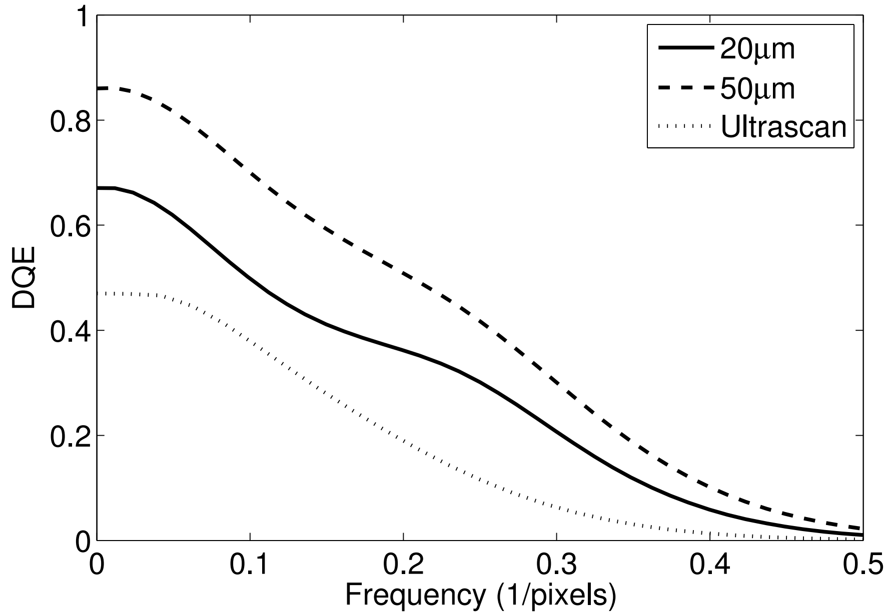

(a)

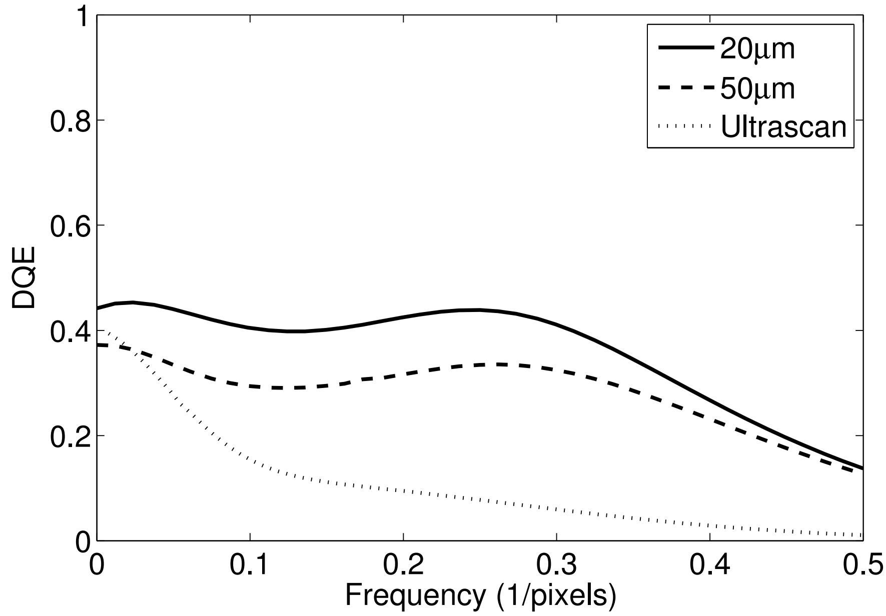

(b)

Figure 5.3: DQE for the two different detector thicknesses of the DUOS sensor at microscope operating voltages of (a) 80kV, (b)200kV. Corresponding results for the Gatan Ultrascan 4000 camera are included for comparison.

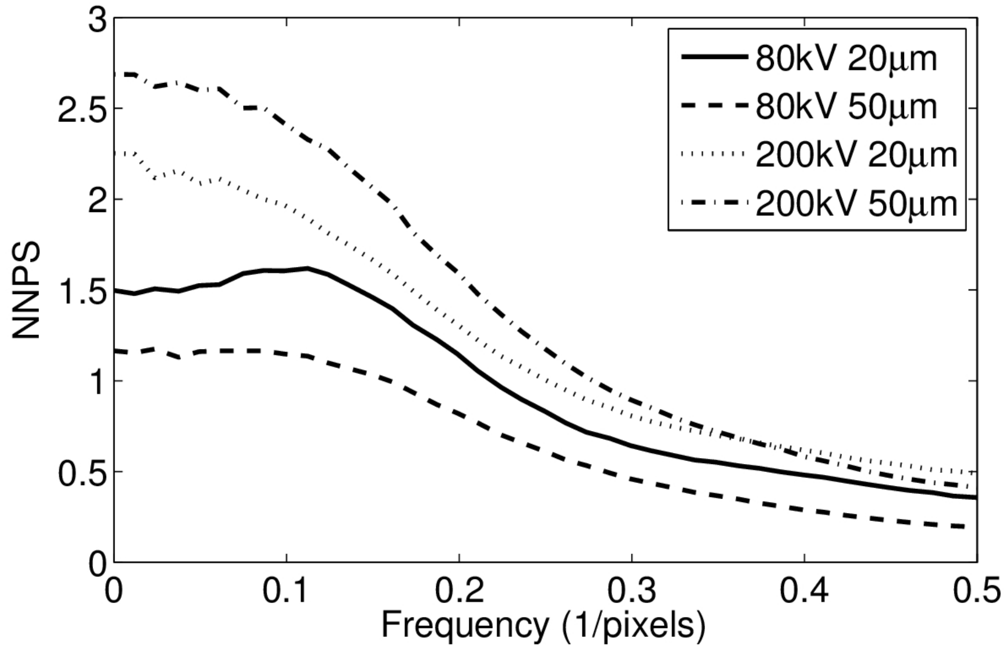

Figure 5.4: NNPS of the DUOS detector at 200kV and 80kV for two different sensor thicknesses.

than expected, but close to the Nyquist frequency there is a good match. At 200kV the thin detector shows a good match at the two ends of the frequency range, but with improved performance in the mid range frequencies from 0.05 to 0.45pixels^{-1}. At 200kV the thicker detector exhibits poorer performance up to 0.1pixels^{-1}, but a good match above this frequency. However, as the DQE has a MTF^2 dependence and given the poor match observed between the experimental and simulated MTF for the 50μm thick detector an operating voltage 200kV it is possible that the good match is by coincidence. Given the MTF dependence we would expect the simulations to underestimate performance at below 0.2pixels^{-1} and overestimate above this frequency. However, the other DQE results show that the simulations overestimate performance at low spatial frequencies and underestimate it at higher spatial frequencies, so it seems likely the two errors are compensating for each other resulting in a good overall match.

Figures 5.7 and 5.8 show images of gold particles on an amorphous carbon film at 80kV and 200kV respectively. The results from the Ultrascan 4000 camera have been cropped such that they show the same field of view as the results taken on the 20μm

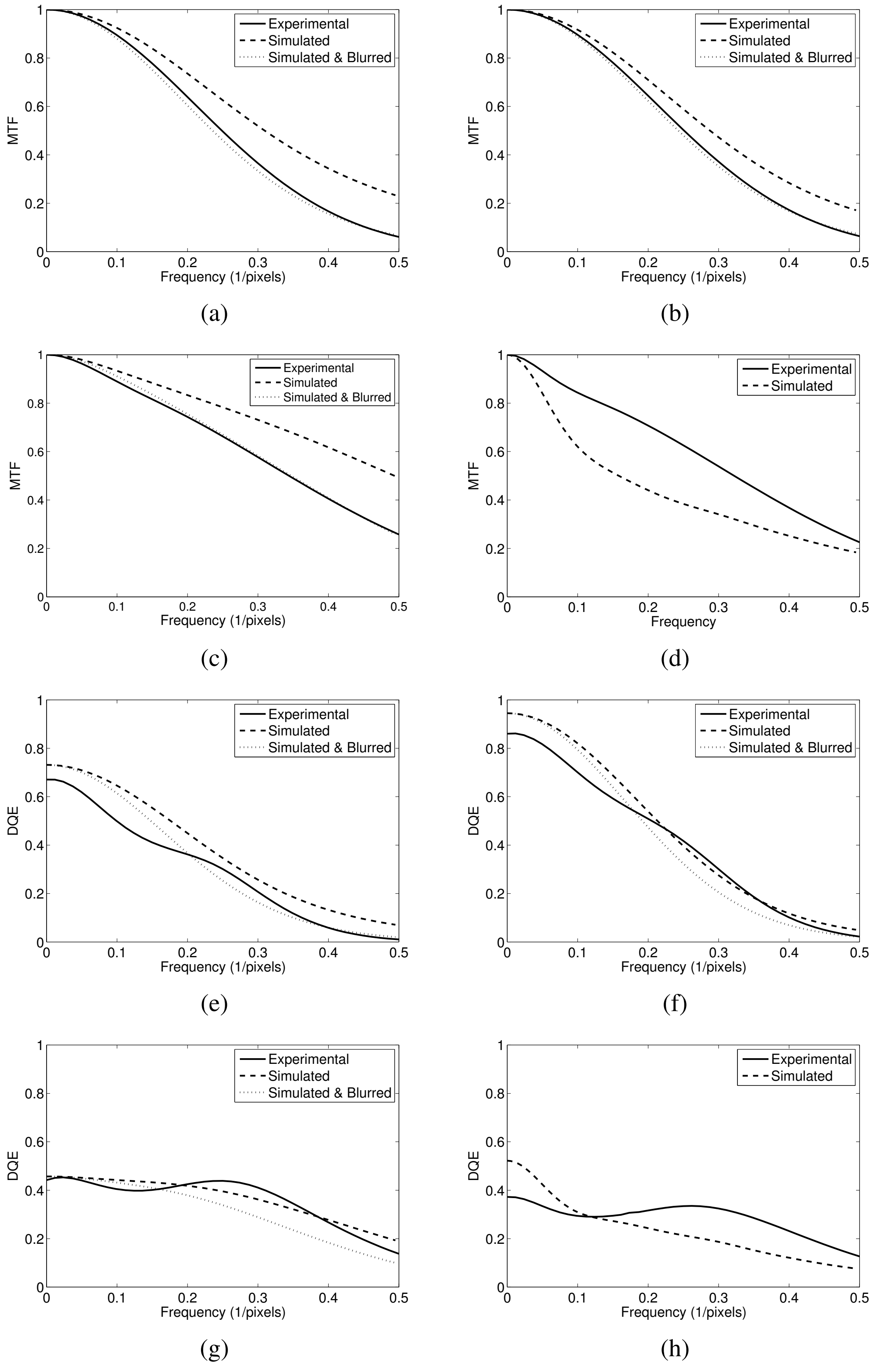

Figure 5.5: Experimentally measured data with simulations with and without an additional Gaussian blur of 10μm. MTF at (a) 80kV for a 20μm detector, (b) 80kV for a 50μm detector, (c) 200kV for a 20μm detector and (d) 200kV for a 50μm detector. DQE at (e) 80kV for a 20μm detector, (f) 80kV for a 50μm detector, (g) 200kV for a 20μm detector and (h) 200kV for a 50μm detector.

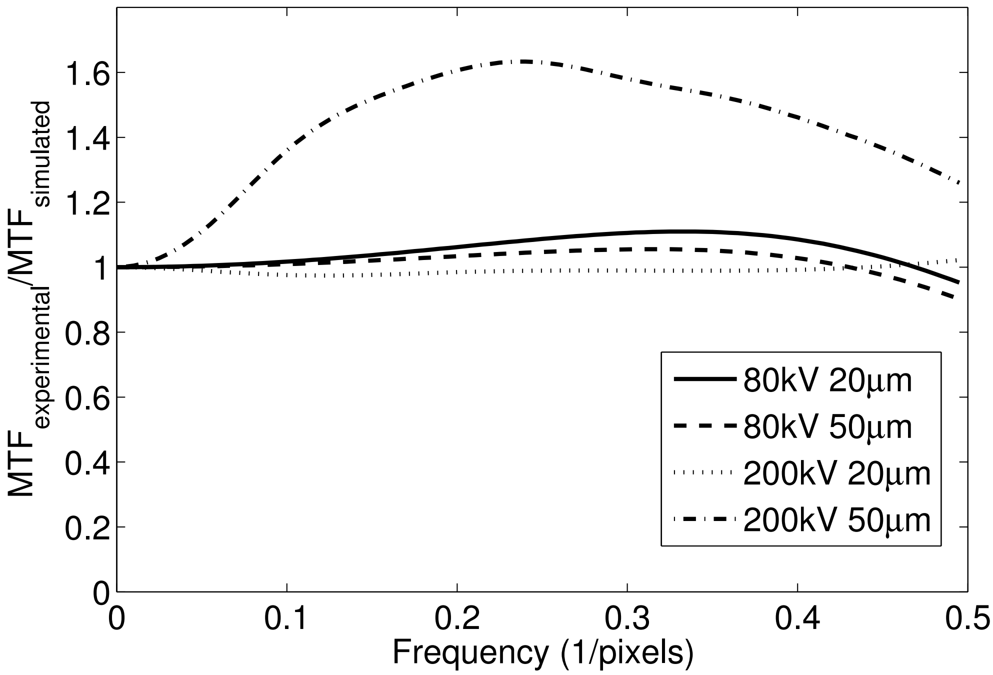

Figure 5.6: The quality of the match between simulated and experimental results shown by dividing the simulated MTF by the experimental MTF for each detector.

thick DUOS detector. In Figure 5.7 detector artefacts can be seen in the power spectra, in the 20μm thick DUOS detector the bright points in a regular array not associated with the particles arise from periodic readout noise, while vertical streaks in the power spectrum from the Ultrascan Camera is likely from differences in the characteristics of the separate quadrant readouts at the low doses being used.

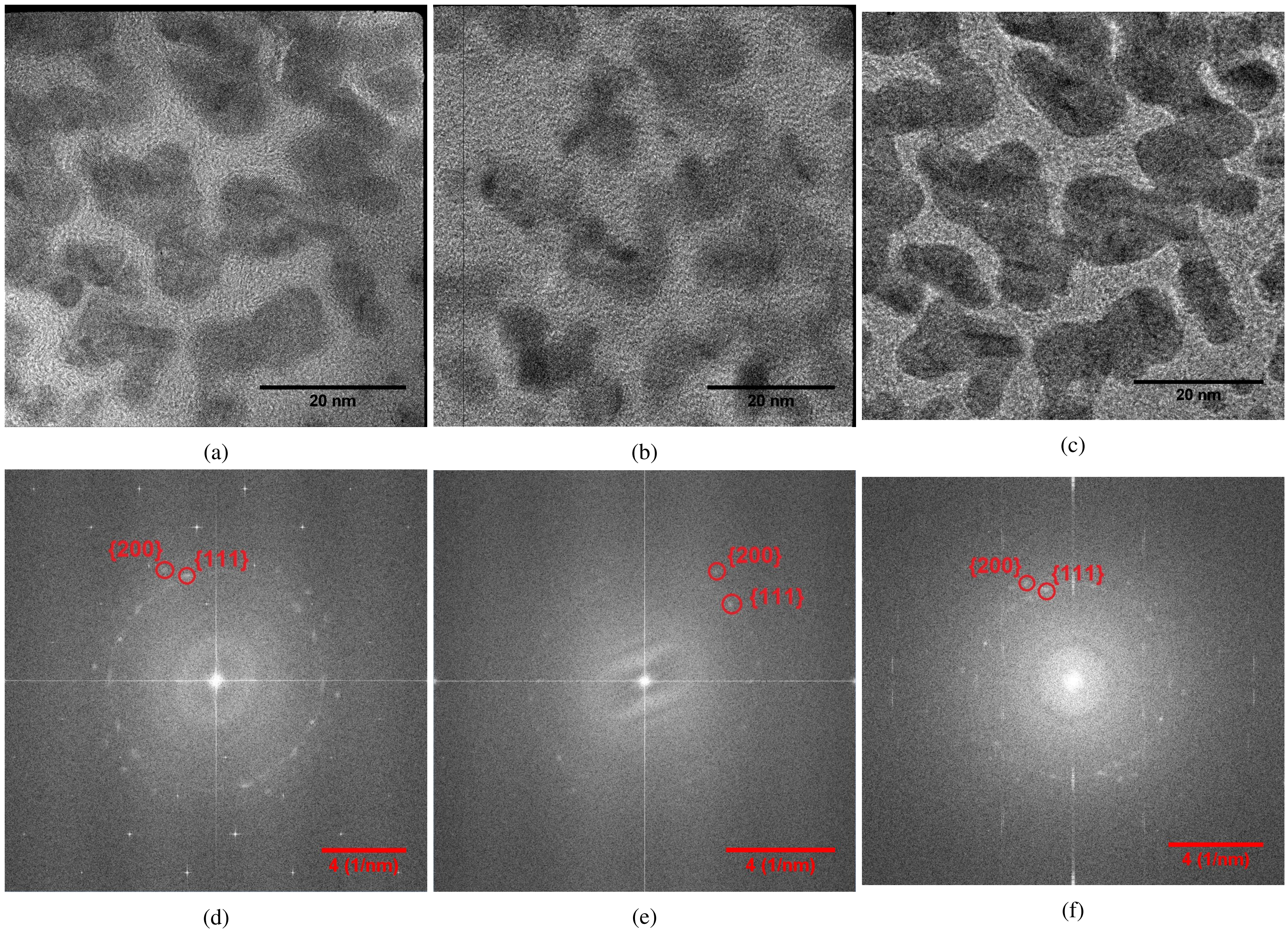

Figure 5.7: Images of Au particles on an amorphous carbon film at 150kX magnification and 80kV microscope operating voltage. Images were taken at a dose of (a) 14 electrons/pixel on a 20μm thick DUOS detector, (b) 13 electrons/pixel on a 50μm thick DUOS detector and (c) 13 electrons/pixel on the Ultrascan 4000 camera. (d)-(f) show the corresponding power spectra calculated from (a)-(c). Some residual astigmatism is present in image (b)

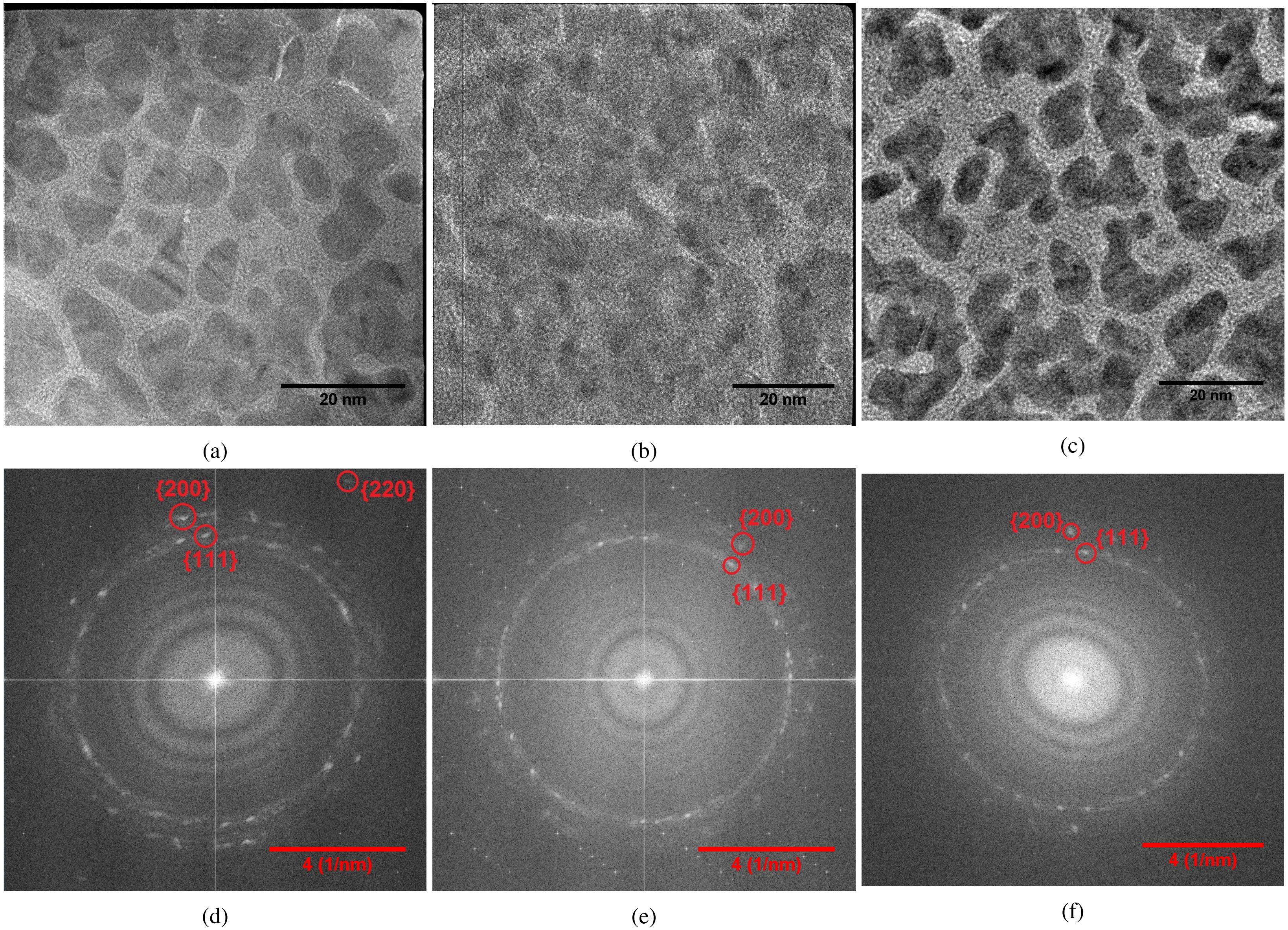

Figure 5.8: Images of Au particles on amorphous carbon at 150kX magnification and 200kV microscope operating voltage. Images were taken at a dose of (a) 89 electrons/pixel on a 20μm thick DUOS detector, (b) 81 electrons/pixel on a 50μm thick DUOS detector and (c) 80 electrons/pixel on the Ultrascan 4000 camera. (d)-(f) show the corresponding FFT calculated from (a)-(c).

5.2.4 Discussion

The results in Table 5.1 show good agreement with those in Figure 3.5, as expected since the signal generated is directly related to the energy deposited. At 80kV there is a significant difference in the mean pulse height arising from the fact in a 20μm thick detector an 80kV electron can pass through the detector, implying that only a proportion of the energy is lost, whilst at 50μm 80kV electrons deposit nearly all their energy in the detector. Similarly the gain at 200kV is consistent with the simulations, with the thinner detector having a much lower gain due to the shorter trajectories associated with those electrons passing through the thinner detector. However, it is more useful to compare the results for the same detector at different voltages, since the gain depends not only on the amount of energy deposited but also the characteristics of the ADC (analogue to digital converter) readout. The ADCs are the readout electronics responsible for converting well electrons generated by the primary electron into a digital pixel value. Each of these ADC converters generally has a slightly different characteristic so that different sensors will show variations in gain. For the 20μm thick detector the simulated mean pulse height suggests the gain at 80kV should be around three and half times that of the gain at 200kV. However the measured gains show a difference closer to three times. The difference is much larger for the thicker detector for which a difference in gain of around one and half times is expected from simulations but a much larger difference of four and half times is observed. Given these differences between the simulated and experimental results for a 50μm thick detector shown in figure 5.5d, it is reasonable to assume that this significant difference is due to effects that are only significant for the 200kV 50μm case. I will consider the causes of these difference later in this section.

The MTF results at 80kV show that there is little difference between the two thicknesses of detector. This is expected as at 80kV the electrons which have the most influence on the MTF, those which reach large lateral displacements, deposit all their energy within the detector in both cases. However, simulations show that for a 20μm thick detector some electrons pass through the detector meaning some energy is not deposited in the detector. This is supported by the lower gain for the thinner detector. While the simulated results suggest that a difference would be noticeable, once the blurring function applied in Figure 5.5 has been taken into account, the differences are very small, with both detectors closely matching the simulated results. The use of a Gaussian blur to match simulated results with experimental results was previously used by McMullan et al. [2]. This blurring factor accounts for pixel cross talk processes that occur post carrier generation, which are not accounted for in Joy's original model. McMullan et al. attribute post carrier generation blurring to the effects of epilayer diffusion, but other effects may also contribute to the cross talk, such as channel coupling in the readout electronics. The standard deviation of 10μm used to correct the data here is wider than the 1/e width of 8.1μm used in the work of McMullan et al. [2] and was selected by trial and improvement to find the optimal width to achieve the best match. The wider distribution required likely arises from differences in the sensitive layer thickness, pixel size and photodiode size between the DUOS detector and that described in [2].

The MTF data at 200kV are also consistent with expectations; the thin detector shows considerable improvement compared to the thicker variant due to a majority of electrons passing through the detector without significant lateral scattering. Applying the same blurring effects to the simulated data as those applied at 80kV show a good match for a 20μm detector at 200kV, although the detector performs slightly better than predicted up to approximately 0.3 pixels^{-1}, as seen in Figure 5.5.

The MTF data for a 50μm thick detector at 200kV show a poor match to the simulated results, with the main discrepancy below 0.25 pixels^{-1}. While the simulated results exhibit a sharp drop in this region, the experimental results do not exhibit this feature. As discussed in Chapter 3 this initial drop is associated with electrons which, at high energy undergo scattering such that they are travelling within the plane of the detector, depositing energy at large lateral displacements. As thick detectors exhibit

Configuration	“Straight”	“Scattered”
80kV 20μm	68%	32%
80kV 50μm	14%	86%
200kV 20μm	93%	7%
200kV 50μm	66%	34%

Table 5.2: Proportion of electrons with the two types of trajectory, as indicated by the two peaks in the pulse height distribution, for two different thicknesses of detector at two different operating voltages.

this drop [2], there must be an issue with Joy’s model. However, the model works at 80kV where the predominate type of trajectory is one that deposits all its energy within the detector and for the thinner detector at 200kV where it is expected that most electrons pass through the detector without significant scattering. This suggests that the issue arises in the transition region where both types of electron trajectories are present, with the probability of an electron passing through the detector being higher than that predicted by the model. Table 5.2 shows the percentage of the two different type of trajectory found by integrating the simulated pulse height distributions. The simulation predicts 34% of the trajectories are deflected significantly and because these trajectories deposit more energy they contribute a larger amount to the signal generated. It is these trajectories that the results suggest there are less of. Adjustments to the model are beyond the scope of this work, but it is believed the most likely mechanisms for the discrepancy are either the crystallography of the material and associated channelling effects arising from the incident beam aligning with the [001] direction of the silicon wafer or in the treatment of secondary electrons.

Examining the NNPS results in Figure 5.4 allows us to examine effects on the DQE which are not due to the effects in the MTF. It is clear that at 200kV the detector has more noise than at 80kV. This arises from the fact at 200kV, there is a wider variation in the amount of energy deposited by a primary electron, which changes the amount of signal generated. There are two factors that underlie this. The first is associated with the two types of trajectory taken by the primary electron, those which pass through the detector with minimal lateral scattering and those which undergo significant lateral scattering. As these two processes deposit different amounts of energy in the detector when there is a more even distributions of the two types there is a greater variation in the gain. The second factor is the variation in the amount of energy deposited by the subset of primary electrons which pass through the detector. As there can be a large variation in the length of the electron trajectory before it escapes the detector, there is a corresponding variation in the amount of energy deposited. For an electron which deposits all its energy within the detector, there is much less variation, apart from that due to the small number of electrons which scatter through nearly π radians and escape from the top surface of the detector. Hence, most electrons will deposit close to their primary energy in a detectable form. At 200kV these effects are more significant explaining the higher noise at higher voltage. At 80kV the thinner detector is noisier, arising from the fact that the detector is sufficiently thin for electrons to pass through, which as has been discussed for the 200kV case gives a larger variation in the amount of signal generated.

Figures 5.7 and 5.8 show lattice fringes in Au nanoparticles. Examining the data at 200kV for the thinnest detector we can clearly see spatial frequencies corresponding to the $\{111\}$ lattice spacings at 2.36Å and the $\{200\}$ spacings at 2.04Å. At 80kV comparing the 20μm thick DUOS detector with the Ultrascan 4000 there is a limited improvement, although the $\{200\}$ reflections appear slightly stronger. The improvements at 200kV are much more apparent as expected, given the MTF results. Using the DUOS sensor both the $\{111\}$ and $\{200\}$ planes are visible, being clearer for the 20μm thick detector. The image from the Ultrascan 4000 shows the $\{111\}$ spacing, but the $\{200\}$ is almost absent. In addition for the data from the 20μm thick DUOS detector there is some indication of even smaller spacings, with reflections in the power spectrum corresponding to the $\{220\}$ spacing at 1.43Å.

5.2.5 Conclusions

This section has described effects of operating voltage and detector thickness on detector performance. Measuring the performance of the DUOS detector at 80kV and 200kV for 20μm and 50μm thick detectors demonstrates an improvement when using thinner detectors at higher voltages. The experimentally measured results were compared to the simulations presented in Chapter 3, which showed good agreement when an additional Gaussian blur to account for pixel crosstalk was included. The exception to this was the 50μm detector at 200kV where matching to the simulations was poor. Under these conditions the detector performed much better at low spatial frequencies than expected, the lack of an initial sharp drop indicating a lack of electrons undergoing large lateral displacements. It is possible that this effect arises from the lack of any considerations of crystallography in Joys model, which could be important as the incident electrons will be very close to the [001] direction in Si. Finally images of Au particles on amorphous carbon are shown where the improved detector performances lead to improved ability to resolve lattice spacings, particularly at low magnification. At 200kV it was possible to identify signal from the $\{200\}$ planes and a much stronger response from the $\{220\}$ planes at 150kX magnification at an intermediate dose of 89 electrons/pixel, (130 electrons/Å^2).

5.3 Correcting Drift with High Frame Rate Detectors

5.3.1 Experimental Details

Sample drift is an issue in many situations; vibrations, sample charging, holder instability and many other effects can lead to sample drift. An inherent feature of direct detectors is that the final images recorded are generated from a summation of multiple frames to overcome the narrow dynamic range. This has required improved readout speeds, so that data can be acquired at higher rates. However, rather than using a simple summation of frames to acquire a final image, it is possible to register successive frames with respect to each other to limit the effects of drift. In the process of acquiring images of Au on amorphous germanium a number of datasets which exhibited sample drift were collected. In this section the improvement in final image quality arising from registration of a series of frames rather than a simple summation is described.

The dataset presented here is of Au on amorphous Ge. The dataset consists of 126 frames at a nominal magnification of 600kX, with each frame representing an exposure of 60ms giving a total exposure of approximately 7.5s. A single image was formed from the time series in three different ways; a simple summation, rigid registration of each frame or non-rigid registration of each frame. For rigid registration final images were formed using the previous frame in the series and the first frame in the series as the references and subsequently compared (Figure 5.9), additionally an image was formed by rigidly registering with respect to the first frame in the series but discarding the first 20 frames in the series when forming the final image. The non-rigid method used is based on the "gradient descent" technique [89], where the differences in the gradients of two image data are used to diagnose the position varying offsets between them. Specifically, the accelerated 'demons' method based on the work of Cachier et al. [90] and Wang et al. [91] were used. The code used here was developed and implemented in Matlab by Jones et al. [92].

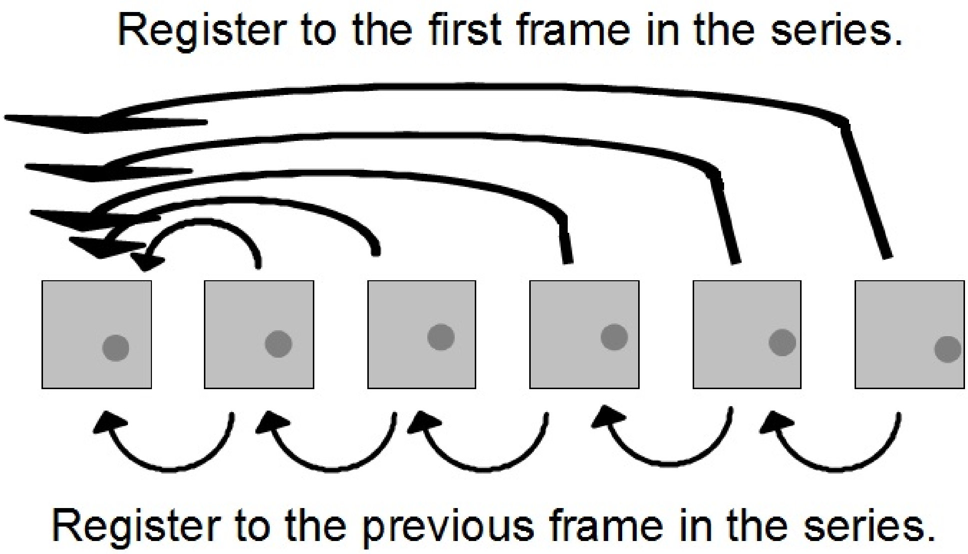

Figure 5.9: Schematic of the two different types of reference image that can be used in rigid registration.

5.3.2 Results

Figure 5.10 shows the results from rigid registration. The results from registration using the previous frame in the series as the reference, the first frame in the series used as the reference and the first frame used as the reference but with the first twenty frames excluded when building the average are shown. It is clear that switching from using the previous frame in the series as a reference to the first frame in the series as a reference improves the final image, as illustrated by a spot at a spatial frequency consistent with the spacing of the $\{331\}$ planes being visible in the latter case. Figure 5.11 shows the azimuthal average of the three power spectra, which shows that there is an improvement in signal transfer when the frames are registered to the first frame in the series as opposed to the previous frame. Excluding the first twenty frames has no effect. Figure 5.12 shows the offset of each frame relative to the first for the two reference frame types. When the first frame of the series is used as the reference shifts occur much more often and the total shift across the whole series is larger. These results indicate that using the first frame in the series produces better results, so the remaining examples of rigid registration presented have been registered with respect to the first

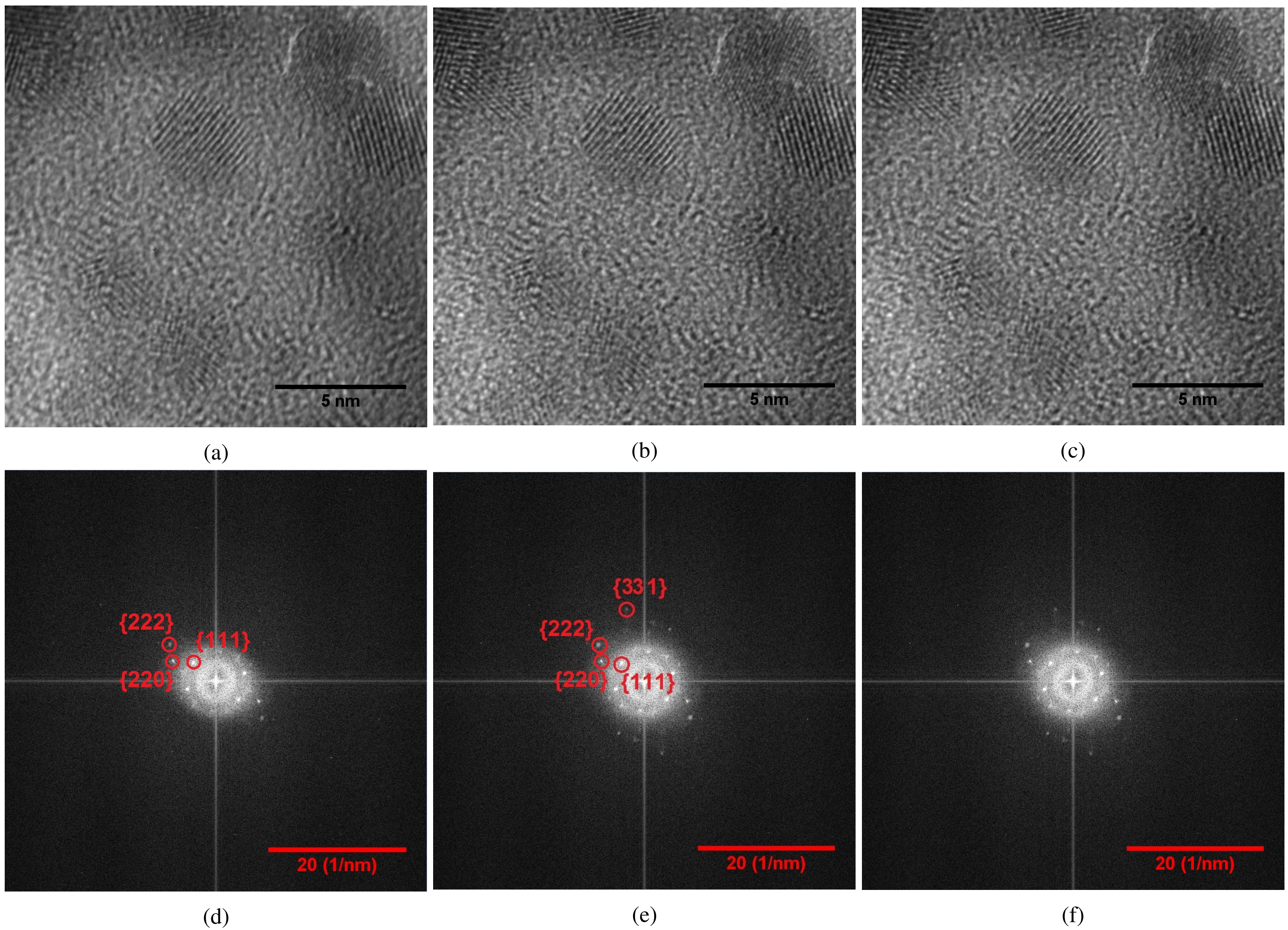

Figure 5.10: Images of Au particles on amorphous Ge, showing the effect of the choice of reference frame used for rigid registration on the resulting image. (a) Reference is the previous frame in the series, (b) Reference is the first frame in the series, (c) Reference is the first image in the series, but excluding the first 20 frames when building the average. The corresponding power spectra are shown in (d)-(f).

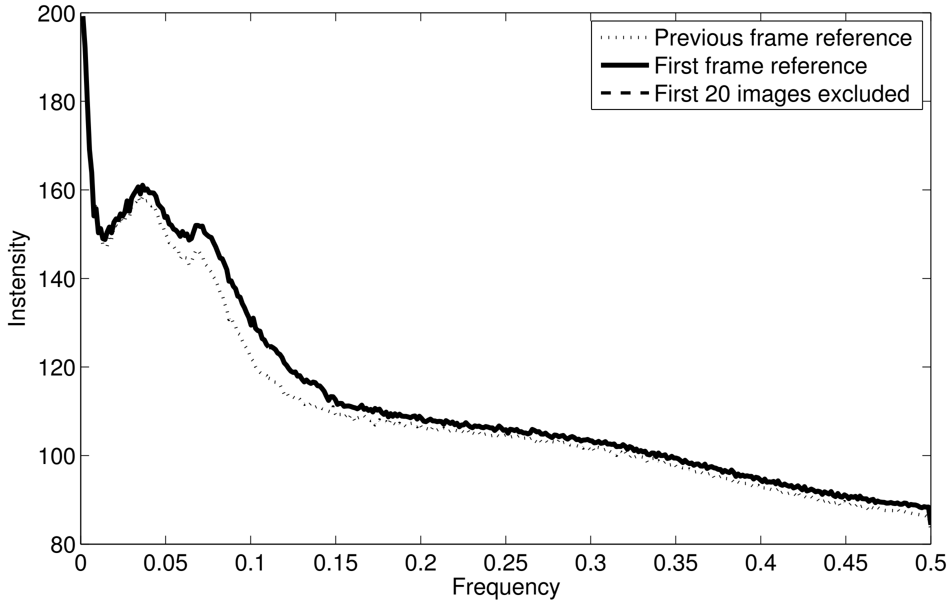

Figure 5.11: Azimuthal average of the power spectra for the three different implementations of the rigid registration. Excluding the first 20 frames has no effect so the result is obscured by the results from first frame referencing.

frame.

Figure 5.13 shows images from unregistered, rigidly registered and non-rigidly registered datasets of frames. The unregistered image shows clear blurring. When registered this blurring is reduced and it is possible to resolve individual atom columns. This is confirmed by the power spectra, with reflections marked in the registered case that are not present in the unregistered case. In addition the power spectra shows a regular array of bright points arising from readout noise that are reduced in the registered cases. The non-rigid registration program measured distortions of approximately 1 pixel in magnitude in the region of the particles, indicating vibration or rolling of the particles on the amorphous support.

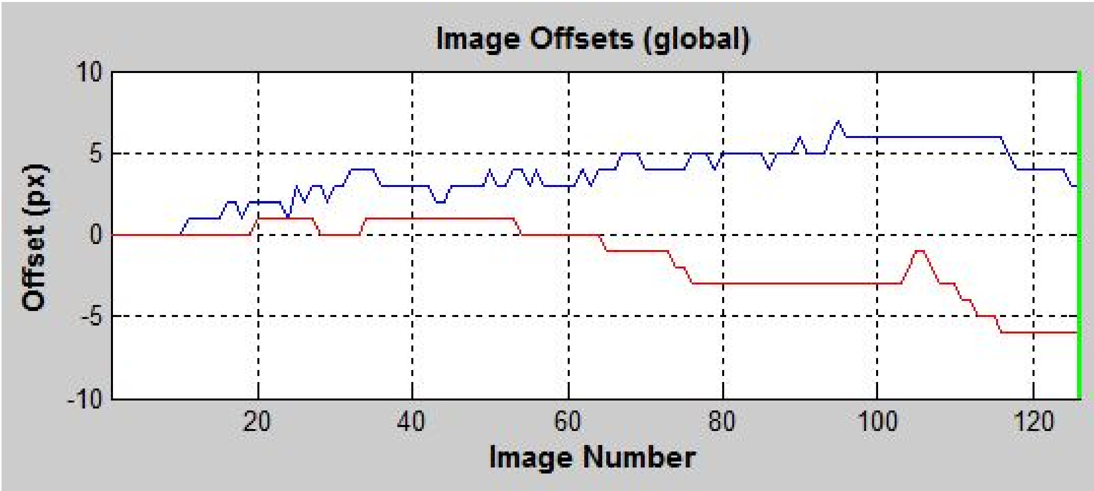

(a)

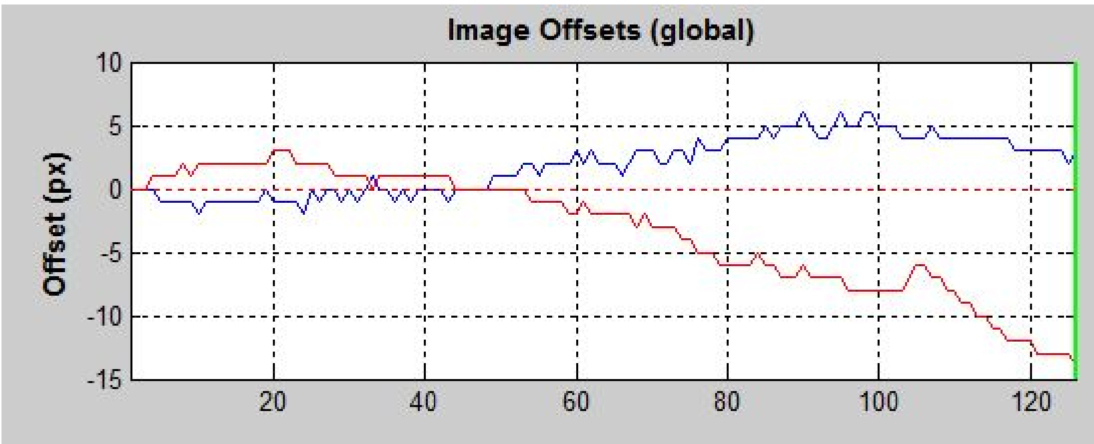

(b)

Figure 5.12: Offset of each frame relative to the first using (a) the previous frame (b) the first frame as a reference image.

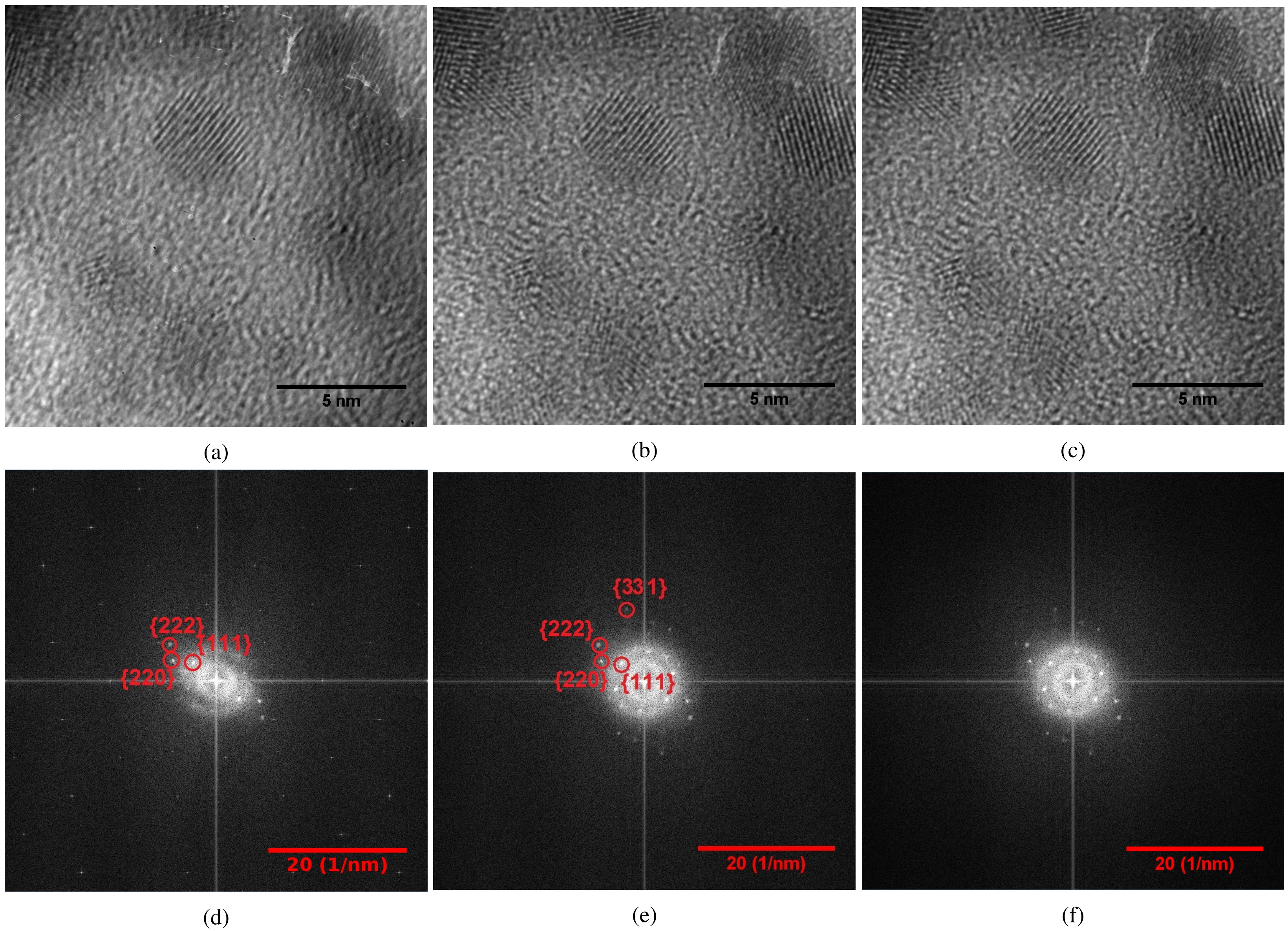

Figure 5.13: Images of Au particles on amorphous Ge. Images represent a total exposure time of 7.5s, and are formed from a summation of 126 images (a) without registration, (b) with rigid registration and (c) non-rigid registration. The corresponding power spectra are shown in (d)-(f).

5.3.3 Discussion

The images show improvement in some directions more than in others, as expected. When the drift direction is parallel to a lattice spacing there will be no loss of intensity whereas when the drift is perpendicular maximum blurring will occur. In the registered images it is clear there has been a significant reduction in readout noise. This arises from the fact that readout noise is a fixed pattern on the detector and as frames are shifted relative to each other by the rigid registration the readout noise is spread over multiple pixels suppressing its effects. A related concern is that readout noise can have a pinning effect in registration, as the noise leads to high pixel values for the same pixel on the detector in all frames which will favour a zero frame shift such that the brighter pixels remain aligned. This issue is confirmed by the results in Figures 5.10 & 5.12. When registered with the previous frame in the data, the changes between the frames will be small due to the limited time for drift between the frames. This means that the offset between frames is small and hence artefacts in the detector are more likely to be registered with respect to each other giving a zero offset. When registering to the first frame of the series frames captured later in the series show the greater offset from the reference image due to the increased time for drift to occur. As the offset is larger the accuracy of the registration improves as there is less chance of the fixed pattern noise being registered with itself resulting in a zero shift. The rationale behind removing the first twenty frames from the final image is that the first frames are those that are most similar to the reference image, so are the most likely to be improperly registered due to the effects of readout noise. However, the results show that this has very little effect indicating that drift is sufficiently rapid that the offset rapidly become large enough such that readout noise is not registered between frames. There is also the concern that non-rigid registration could lead to the readout noise being reintroduced. However, the bright spots seen in Figure 5.13d are not present in the aligned power spectrum from the non-rigidly aligned data shown in Figure 5.13f indicating this is not the case.

It is clear that rigid registration significantly improves the resolution achieved in an image formed from a time series of frames, as the blurring effects of sample drift can be removed. The ability to rigidly register series collected at a high frame rate has already been demonstrated and is now being implemented as a hardware option in cameras such as the Gatan OneView [93]. Non-rigid registration of the data presented here shows little further improvement. This is to be expected as the distortions detected by the registration algorithm are of the order of one pixel, implying that the benefits of non-rigid registration are only observed close to the Nyquist frequency. However, we can see from the power spectra presented that there is little information at these spatial frequencies. However, as shown in the previous sections a direct detector is capable of acquiring data at high spatial frequencies, indicating that non-rigid registration could offer improvements in certain situations.

5.3.4 Conclusions

In this section it has been shown that rigid registration of a time series of frames collected at high frame rate can be used to improve resolution by removing the blurring arising from drift. We have also applied non-rigid registration which detects and corrects distortions, which lead to corrections of the order of 1 pixel. This indicates potential improvements to signal collection close to the Nyquist Frequency, which is a key advantage of direct detectors.

5.4 Characterisation of the DE-20

5.4.1 Introduction

The DE-20 is a commercial camera sold by Direct Electron, with a 5k by 4k array size with a pixel pitch of 6.4μm. The detector can be operated up to 30fps for full frame readout with higher frame rates achievable by selecting only a sub-area of the detector.

5.4.2 Experimental Details

The DE-20 detector was characterised at 200kV on a FEI Tecnai instrument. All parameters reported were measured at 30fps with a dose of 0.228 electrons/pixel/frame with 192 frames being captured for final image summation. The MTF was calculated from analysis of the sharp edge created by the shadow of a beam stop. The shorter straight edge of the head of the beam stop was used rather than the shaft of the beam stop due to alignment of the shaft with the pixel array causing aliasing, whereas the head was inclined with respect to the array. The detector is fitted with a Faraday plate which measures the electron dose in an exposure. To convert pixel values to electrons for the uniform illumination used to calculate the NPS, an image was scaled such that the mean pixel value matched the electron dose/pixel measured by the Faraday plate.

5.4.3 Results and Discussion

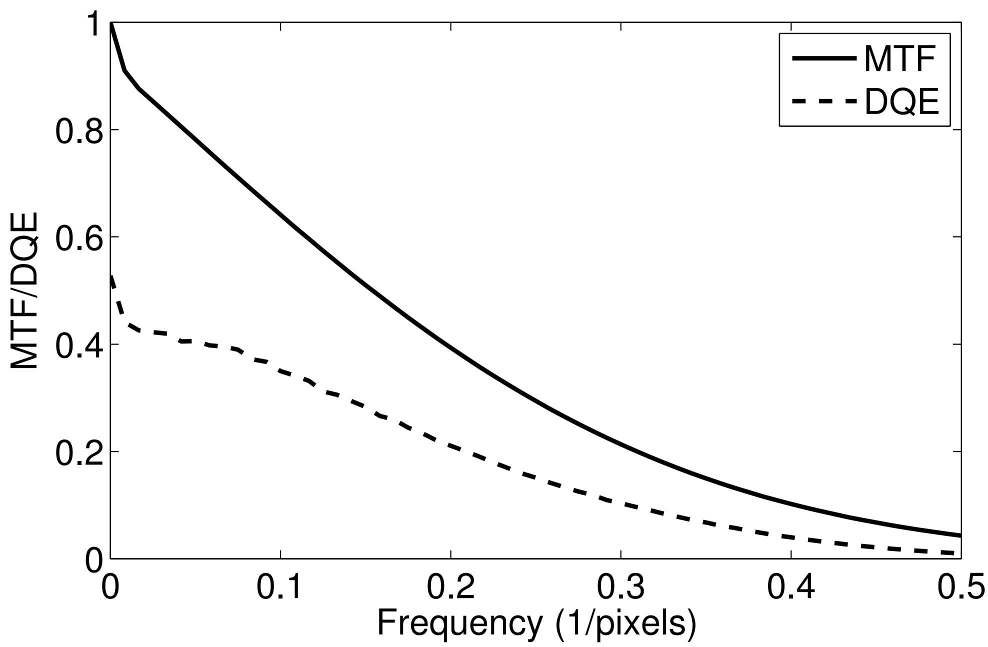

Figure 5.14: MTF and DQE of the Direct Electron DE-20 detector measured at 30fps.

Figure 5.14 shows the MTF and DQE calculated for the DE-20 camera. The results show that compared to the DUOS detectors discussed earlier in this chapter the

MTF falls much more rapidly as expected due to the smaller pixel size. This smaller pixel size means that for the same lateral distance travelled by an electron, signal is generated in more pixels giving a larger drop in the MTF at low spatial frequencies. A measurement of the MTF and DQE at 200kV for this camera has not been published, although data at 300kV has been published by McMullan et al. [45]. Comparing the data from this publication with the experimental data included here it is clear that the performance increases by a factor of four from 200kV to 300kV. At 200kV there is a much sharper initial drop at low spatial frequencies; at 0.1 pixels^{-1} at 300kV the MTF exceeds 0.8, whereas at 200kV the MTF is close to 0.6 at the same spatial frequency. This sharper drop suggests that there are still significant numbers of electrons that deposit most of their energy in the detector although this cannot be quantified as the thickness is not known. The small pixel size of the detector implies that there will also be an improvement in the MTF arising from the smaller interaction volume of those electrons which pass through the detector.

The differences in the DQE results between the published 300kV data and that presented here is also in line with expectations. Comparing the MTF to the DQE for the two cases it is clear that the noise, as described by the NNPS must be larger for the 200kV case with the wider distribution of energies deposited in the 200kV case leading to these higher levels of noise.

5.4.4 Conclusions

This section has shown characterisation results from the Direct Electron DE-20 camera. The smaller pixel size of this camera compared to the DUOS detector explains the more rapid drop at low spatial frequencies. Additionally this characterisation is compared to published results for the same camera at an operating voltage of 300kV, where it is clear the increased operating voltage improves performance.

Chapter 6

Basis for Future Work

6.1 New Materials for Direct Electron Detectors

6.1.1 Introduction

Si is almost the universal material for detectors and semiconductor devices for fast electrons. However, other materials are of interest due to potential performance improvements. Gallium Nitride (GaN) is of particular interest for a number of reasons. Firstly it has been shown that GaN has higher intrinsic radiation hardness [94] compared to Si. Secondly it has a wider band-gap (3.4eV for GaN compared to 1.1eV for Si) meaning less signal is generated per electron which improves dynamic range as more carriers need to be generated to fill the well depth of the pixel and saturate the sensor. Thirdly it has a faster rate of energy loss, leading to smaller interaction volumes, hence improving MTF and DQE performance.

Before time and money is invested in the detailed design of specific detectors, modelling allows a theoretical measurement of the improvement expected from changing the base material. The same Monte Carlo simulation described in Chapter 3 was used to simulate detectors using potential new materials.

Results for Si and GaN detectors with a thickness of 30μm were initially modelled at 80kV and 200kV followed by a more complete dataset generating simulated detectors with thicknesses of 20μm, 25μm and 50μm in the two materials across a 20kV to 300kV range at 20kV intervals. From this dataset value for the MTF and DQE were extracted at half the Nyquist frequency and at the Nyquist frequency.

6.1.2 Results

The MTF for the two different materials at two different operating voltages are shown in Figure 6.1. As expected the MTF is better for GaN with a larger improvement at lower operating voltages; at the Nyquist limit the MTF shows an improvement of *ca.* 0.025 at 200keV, and *ca.* 0.2 at 80keV.

The cumulative frequency shows the maximum number of events/electron, at the point of which the frequency reaches 20000, which is the total number of electrons simulated. Figure 6.2 shows that at 80keV the GaN detector has a maximum of $<$100 events/electron, compared to approximately 200 events for Si. At 200keV comparable results show a maximum of 200 events in GaN and 450 events in Si. However, it is clear that the average number of events in Si is lower, which implies that the gain of the detector will be lower.

Figure 6.3 shows in greater detail the voltage dependence of the different materials. The MTF improves towards either extreme of the voltage range simulated, with a minima within the voltage range. At lower voltages the performance is independent of thickness, but as voltage increases thinner detectors perform better. GaN detectors outperform Si versions and the minima for GaN detectors are displaced to higher energies relative to their Si counterparts.

Figure 6.4 shows a subset of trajectories from the dataset, showing 50 electron trajectories for 140keV electrons travelling in GaN and Si projected onto a plane. These trajectories clearly show that electrons in GaN interact with a smaller volume, with only a few electrons escaping to the opposite side of the detector, whereas electrons travelling through Si can reach much larger lateral displacements and a higher proportion of electrons escape the detector. Electrons which escape do not deposit all their

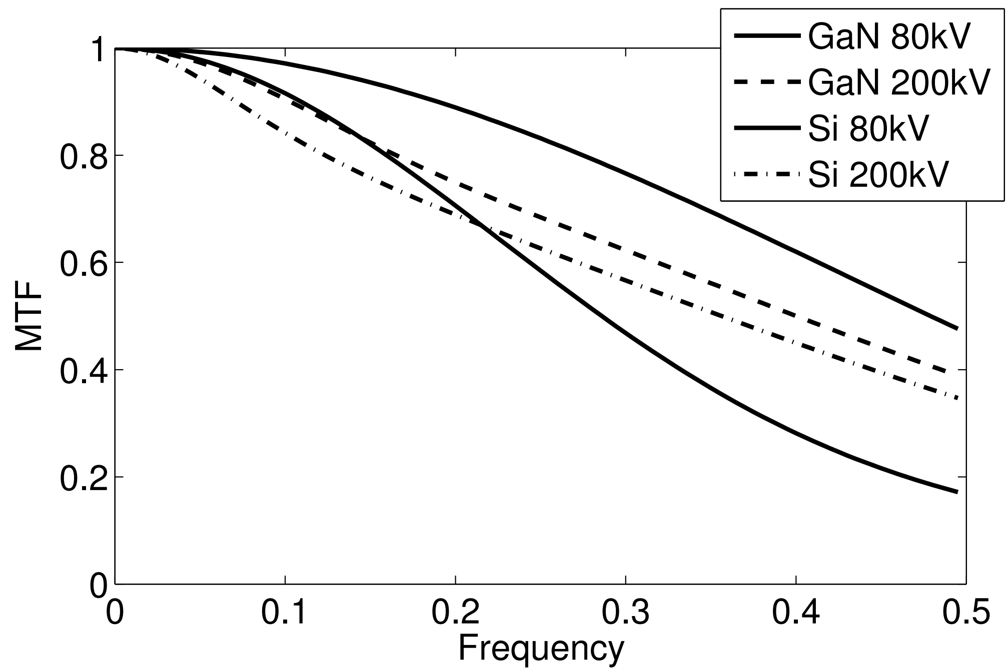

Figure 6.1: MTF for Si and GaN devices with 30μm layers, at 200kV and 80kV.

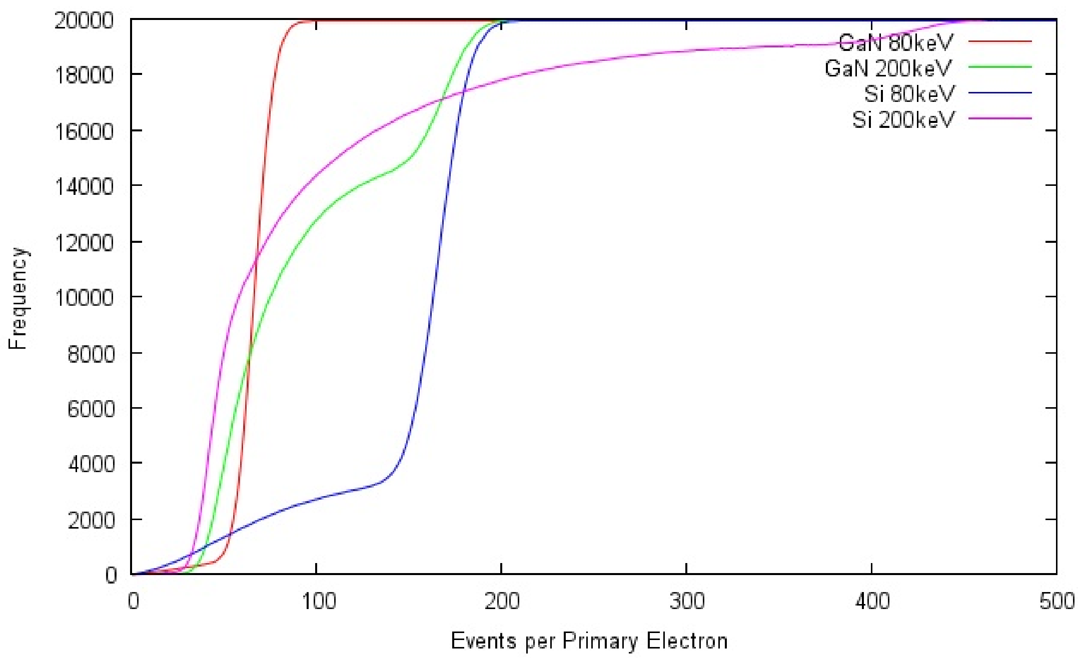

Figure 6.2: Cumulative frequency of events/140kV primary electron for a 50μm thick detector.

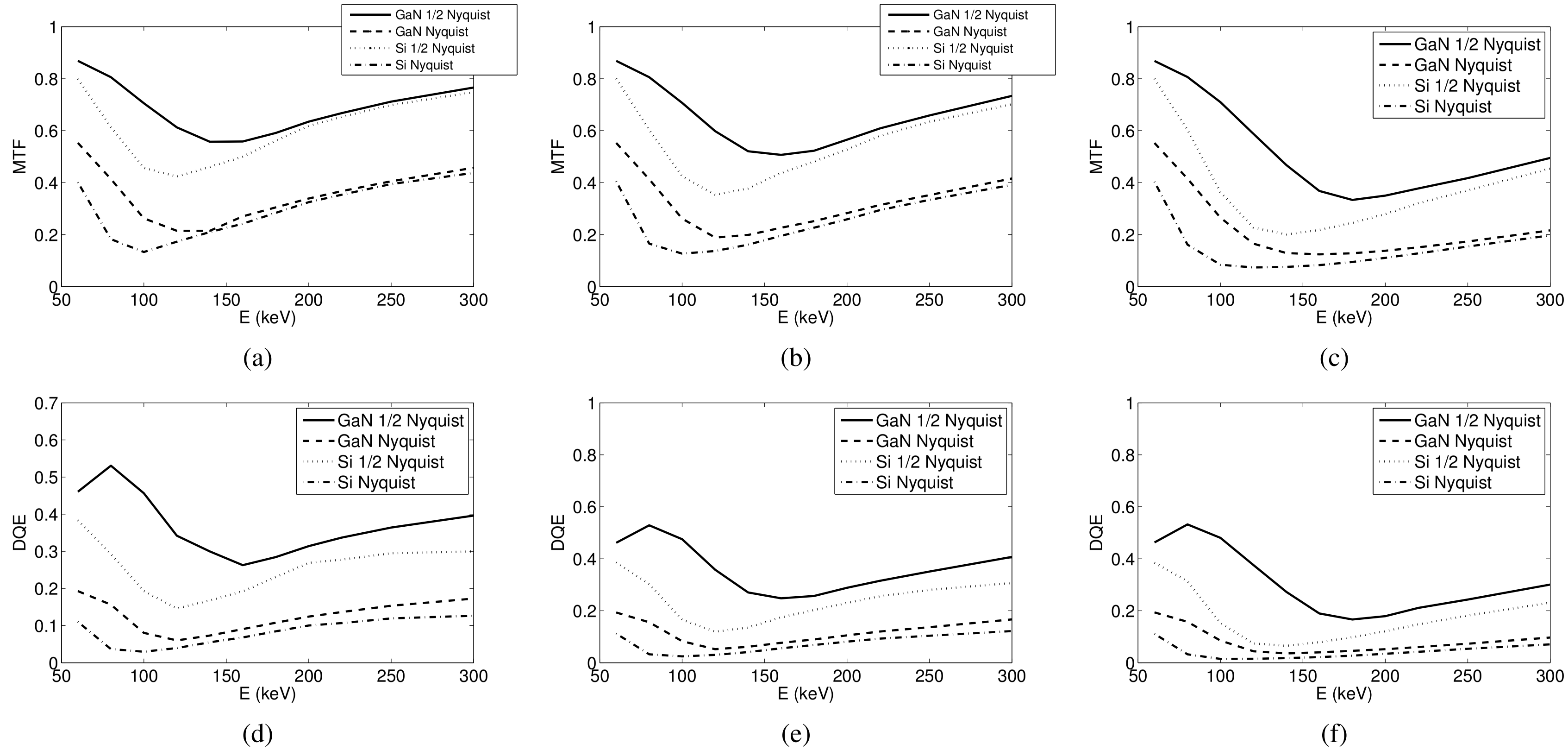

Figure 6.3: Comparison of the MTF and DQE of GaN and Si detectors as a function of operating voltage and thickness. The, MTF and DQE are shown at half the Nyquist Frequency and at the Nyquist Frequency for a range of voltages. (a) MTF at 20μm, (b) MTF at 25μm, (c) MTF at 50μm, (d) DQE at 20μm, (e) DQE at 25μm and (f) DQE at 50μm.

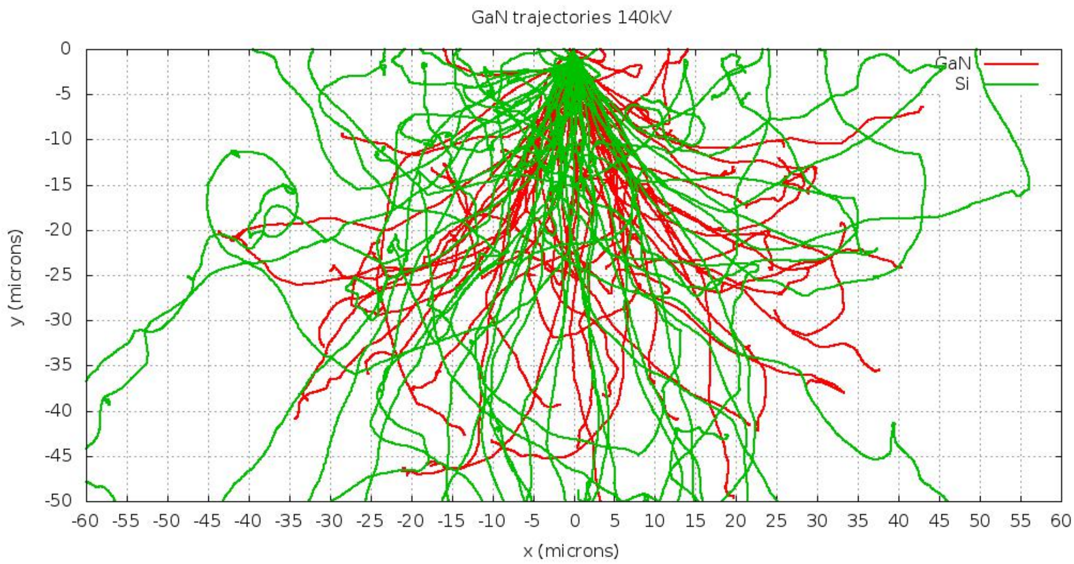

Figure 6.4: Trajectories of 50 electrons at 140keV through a 50μm thick detector based on Si and GaN.

energy, which means that the gain of the detector is lower.

6.1.3 Analysis

The general shape of the plots in Figure 6.3 has been explained in Section 3.2. The shape was attributed to a two types of electron, those which pass through the detector with a very straight trajectory and those which are deflected and deposit larger amounts of their energy in a detectable form. At low energies the increasing average electron interaction volume degrades the performance as the voltage increases. However at a critical voltage electrons are able to pass through the detector giving straight trajectories with minimal lateral scattering. The fact GaN detectors outperform Si ones, while also having their minima displaced to higher voltages indicates a higher rate of energy loss for an electron travelling through GaN. This higher rate of loss leads to a shallower penetration depth, improving the MTF due to the smaller mean lateral displacement. This shallower depth of penetration is shown in Figure 6.4. Recalling the Bethe equation (Equation 2.9) it is clear that the higher rate of energy loss is due to the larger average atomic number and density of GaN compared to Si.

The potential improvements in performance from the use of GaN based detectors are more significant at lower energies. At low energies where performance is dominated by electrons that dissipate all their energy within the detector the GaN detector will excel due to the smaller interaction volume. However at higher voltages electrons passing through the detector become the dominant type that determine properties. In this case the increased rate of energy dissipation of electrons in GaN is a minor effect. For this situation it is the mean free path between Rutherford scattering events which is expected to be more important, as for larger distances there will be fewer events and reduced probability for scattering through an angle which leads to large lateral displacement. Referring to equations 2.2 & 2.3 which describe the mean free path between the elastic scattering events indicates that the change in mean free path from using GaN rather than Si is less than the change in the rate of energy dissipation between the two materials, explaining why the difference between the two materials is much smaller at high voltage.

Considering the Dynamic range of detectors, if the simple approximation of equal well depth regardless of material is made, then the dynamic range is inversely proportional to the average events/electron. When electrons deposit most of their energy in a detectable form, such as at low operating voltages, then GaN is superior. Figure 6.2 shows that at 80kV there are fewer than half the events in GaN compared to Si arising from the wider bandgap of GaN. However when electrons pass through the detector a situation in which different amounts of energy deposited can arise. As the rate of energy deposition is higher in GaN an electron which passes through the detector will deposit more detectable energy in GaN than in Si. Figure 6.2 shows that under certain conditions, in this case a 50μm thick detector at 200kV, the dynamic range of a GaN detector will be less due to a larger number of events being generated from the increased amount of energy deposited.

6.1.4 Conclusions

In this section it has been shown that switching from Si to GaN based detectors could result in improved detector performance. The improvements are most noticeable at lower operating voltages where most of the electron's energy is dissipated within the detector. It has also been shown that when detector performance is dominated by the effects from electrons which pass through the detector, which is the case for thin detectors above approximately 100kV, the improvements are much smaller. In this case the improvements are unlikely to justify the increased cost and complexity of fabrication in GaN which arise because GaN device fabrication is a much smaller industry so the costs of fabricating equivalent structures are much higher and because GaN has not been used for this application before there is a much larger design workload.

6.2 Splitting Sensor and Readout PCBs

6.2.1 Premise

This work has primarily focused on the performance of sensors, however there are also practical considerations that must be taken into account when designing a camera system. The physical size of the detector is critical for mounting as many electron microscopes have limited space inside the column for mounting a detector. The TEM data previously described made use of existing hardware in the form of a Gatan mechanical "sledge" to position the camera. However for EBSD a new approach is required. In the initial work presented in Chapter 4 the detector was mounted inside the SEM but this is impractical for two reasons. Firstly, it requires a large amount of space inside the chamber which is only possible on some models of SEM and secondly for EBSD there are advantages in changing the detector position and measuring changes in the pattern to calculate strain. However manoeuvring the whole detector with sufficient precision to accomplish this is generally impractical. The proposed solution is to separate the sensor PCB from the rest of the detector using a flexible PCB so that the sensor can be mounted on a mechanical system to adjust its position within the chamber, with the rest of the system outside the vacuum and with the flexible PCBs passing through an interface flange on the chamber. As this setup implies increased separation between the sensor and the first amplifiers in the readout electronics the effects on the SNR from this setup need to be assessed. This section outlines designs for implementing the separation of sensor and readout electronics together with optical tests to measure the effects of this configuration on the detector performance.

6.2.2 Board Splitting Design

The initial test involved splitting the sensor from the rest of the detector to check if any signal remained with a larger distance between charge generation and amplification. To test this, board to board connectors of the type used to interface between the sensor and readout PCBs were soldered to the ends of ribbon cables. It was apparent that degradation of signal was not significant enough to render the image unusable and so mechanical considerations were then taken into account. It was judged that due to difficulties in passing the ribbon cable across the microscope flange and the rigidity of the system, precise positioning would be difficult. To overcome these design issues a flexi-PCB was constructed to replace the ribbon cable assembly.

There were two major design decisions which needed to be made about the PCB interface. The first was how many PCBs would be used to implement the interface, either one PCB for the whole system, or two, one for each of the two connectors on the rigid PCBs. It was decided that a single PCB would be preferable as it would make interfacing across the flange of the microscope easier. The other decision that needed to be made was how many layers to use in the PCB design. A single sided PCB has the highest flexibility and lowest cost. However, as the PCB is required to route a total 128 tracks, as there are two connectors, each with two rows of 32 pins, a single sided PCB proved inappropriate due to a requirement for exceptionally narrow tracks,

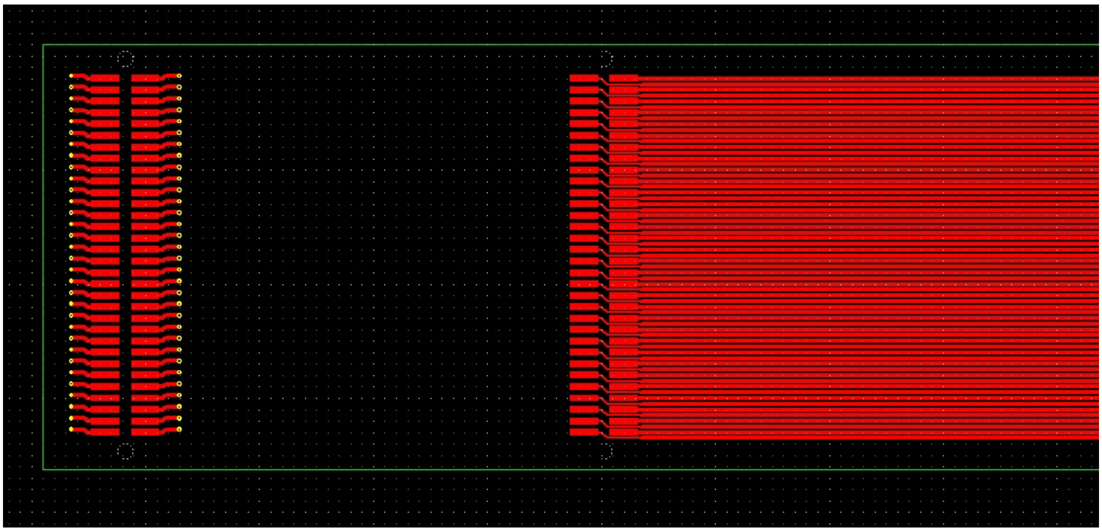

Figure 6.5: One end of one side of the PCB design. Green lines are the edges of the PCB, red are copper tracks and yellow are the position of vias for bridging connections between the two sides of the board.

or tracks of significantly different length. Different lengths of track will have different resistances, which will lead to different attenuation of signals. Hence, the final design used a double sided flexible PCB with vias to connect across the two layers on either side of the board. One side of one end of the design is shown in Figure 6.5. Each side of the board has 64 tracks making the set of connections between two connectors, the pads being positioned such that when the connectors are attached they slot into the rigid PCBs. The tracks on each side are displaced by half the the track pitch to minimise cross talk.

6.2.3 Prototype Data Acquisition

For the optical testing of sensors a test environment was created on an optical bench with a number of features. Table clamps were used to hold the detector in position at a set distance away from a light source. A light source consisted of a cluster of blue LEDs mounted in a cage to fix the light source at a set position. This light source has a wavelength of 470nm and a power of 600μW/cm^2 at a distance of 10cm from the source on the axis passing through the centre of the LED array. At this intensity the detector saturates, so to reduce the intensity to a level below saturation, neutral density filters were stacked together and a diffusion filter was used to ensure uniform illumination.

For both split and unsplit configurations a set of 32 images were taken under the following conditions; dark images were recorded to find the pedestal level and images illuminated without filters to reduce intensity were recorded to find the saturation level. The pedestal level was then subtracted from the saturation level to find the dynamic range.

6.2.4 Results

Tables 6.1 and 6.2 show the parameters measured in ADC counts compared between the unsplit system and both the ribbon cable splitting and PCB splitting configurations respectively. The values given for the uncertainty in each of the measured values are the standard deviations of the pixel values used to calculate the parameter. There are two features to consider, the change in the absolute values and the change in the width of the spread. The pedestal level shows an increase when using a split board configuration. This increase in level likely arises from the extra resistance and capacitance added by the extra electronics introduced to split the two boards. This will increase the RC time constant of the system, meaning less charge will dissipate between readout events. The saturation level also shows reductions. This is also expected as the saturation level is fixed by the properties of the pixel and the signal from the sensor is an analog signal. The increased distance between the sensitive layer and the ADC converters lead to attenuation of the analog signal resulting in a lower level of signal being recorded. The dynamic range of the system is reduced significantly as a consequence of the pedestal

Parameter	Unsplit Configuration	Split Configuration	Change
Pedestal Level	$38640 \pm 0.60\%$	$39274 \pm 0.41\%$	$(1.64 \pm 0.73)\%$
Saturation	$45946 \pm 0.80\%$	$44591 \pm 0.55\%$	$(-2.95 \pm 0.96)\%$
Dynamic Range	$7307 \pm 4.41\%$	$5339 \pm 2.30\%$	$(-26.9 \pm 4.97)\%$

Table 6.1: Measured parameters of the detector comparing the base and ribbon cable splitting system.

Parameter	Unsplit Configuration	Split Configuration	Change
Pedestal Level	$38640 \pm 0.60\%$	$39800 \pm 1.62\%$	$(3.00 \pm 1.72)\%$
Saturation	$45946 \pm 0.80\%$	$43615 \pm 1.37\%$	$(-5.07 \pm 1.58)\%$
Dynamic Range	$7307 \pm 4.41\%$	$3815 \pm 23\%$	$(-47.79 \pm 23.4)\%$

Table 6.2: Measured parameters of the detector, comparing the base and PCB splitting system.

level and saturation level getting closer together and a relatively small change of a few % results in a significant reduction in dynamic range. However, as the reduction comes from attenuation of signal there will also be a corresponding reduction in gain, meaning that the dynamic range in terms of electron dose is affected much less. In all cases the PCB performs worse which is not unexpected as the distance over which the two boards are separated is larger.

The variation in values is due, to some extent to noise, both the unavoidable shot noise of electrons on the detector, but also readout noise. It is clear from the images shown in Figure 6.6 that there is a fixed pattern to the noise. It is difficult to identify the exact cause of this. Possible causes are periodic instabilities in clocking signals or cross talk between adjacent conductors. However as the noise has a fixed pattern post-acquisition corrections can be applied to reduce this. The appearance of the noise in Figure 6.6 is also worse than in practical use as the flat illumination and the brightness and contrast settings enhance the pattern. When an image is projected onto the detector, the larger variation in signal intensity makes the fixed pattern noise much less obvious.

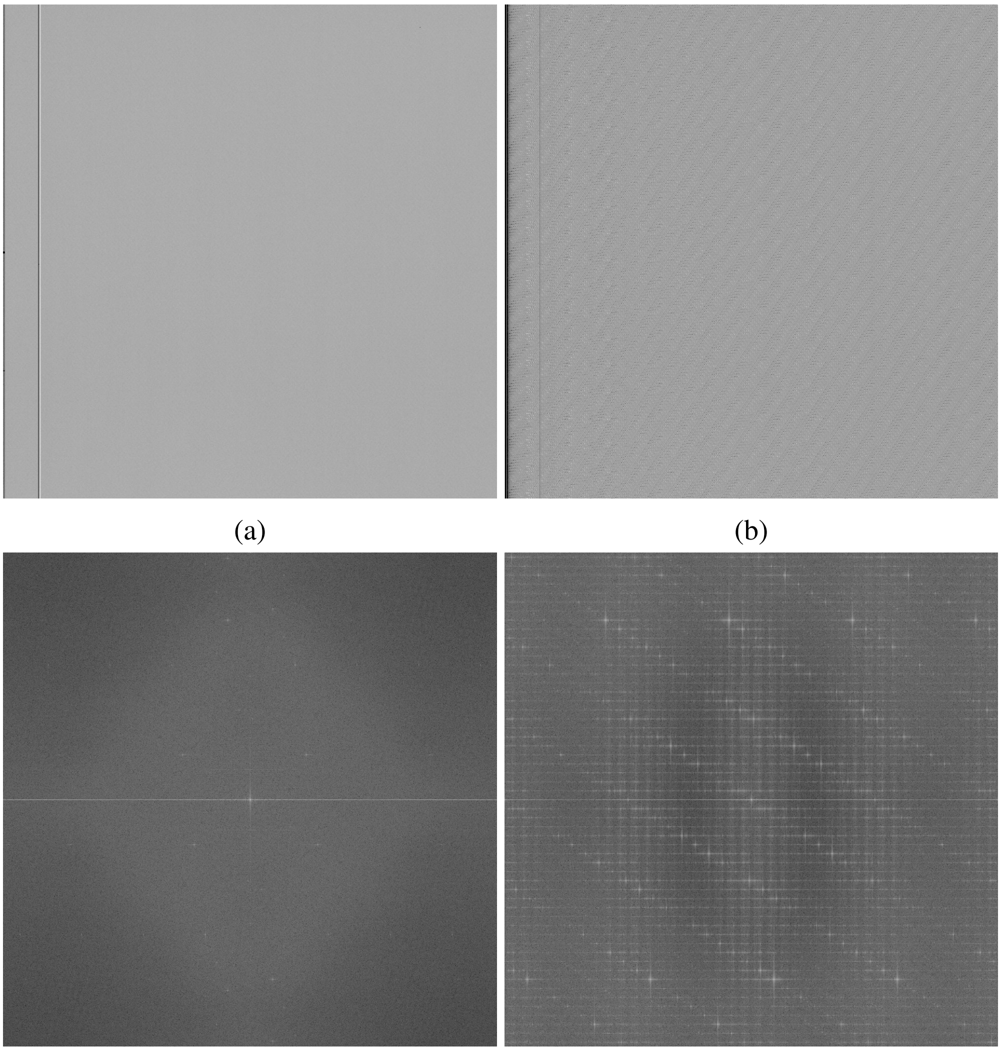

(a) (b) (c) (d)

Figure 6.6: Images showing the DUOS detector saturated with light. (a) Unsplit configuration, (b) with the sensor and readout electronics split by the flexi-PCB. (c) and (d) corresponding power spectrum calculated from (a) and (b).

6.2.5 Conclusions

In this section optical testing of two configurations for splitting the sensor from readout electronics have been characterised using optical illumination. The results indicate that while splitting of the sensor from the rest of the system is not desirable in terms of detector performance, it is possible. This work suggests that in the future it would be possible to use flexible PCBs to mount the detector in a system with limited space, to produce a system that is capable of observing changes in EBSD patterns as the camera length is adjusted through precise changes in the position of the sensor.

Appendix A

ImageJ Codes for Detector Characterisation

A.1 Code for calculation of Line Profile and MTF

```java
//Grigore Moldovan, University of Oxford, 2007-2009

import java.awt.*;
import ij.*;
import ij.process.*;
import ij.gui.*;
import ij.plugin.filter.PlugInFilter;
import ij.measure.*;
import ij.util.*;

public class ModulationTransfer_ implements PlugInFilter {

  int range = 0;          // number of pixels in each direction
  int oversampling = 0;         // oversampling for edge profile
  double[] coefficients = {0, 0, 0};  // edge position
  boolean tune = false;       // scan edge for optimum modulation
  boolean smooth = false;       // apply local average in line spread
```

```java
  double gradient = 0.0;       // gradient of local average (defines window size)

  public int setup(String arg, ImagePlus imp) {
    if (arg.equals("about")) {
      showAbout();
      return DONE;
    }
  return DOES_ALL;
  }

  private void showAbout() {
    IJ.showMessage("About...", "Calculate modulation transfer from a shadow image. G Moldovan, Oxford 2007-2009");
  }

  private boolean get_user_input() {

    // show dialogue
    GenericDialog user_dialogue = new GenericDialog("Modulation Transfer Function");
    user_dialogue.addNumericField("Range of line profile:", range, 0, 6, "pixels");
    user_dialogue.addNumericField("Pixel oversampling:", oversampling, 0, 6, "");
    user_dialogue.addNumericField("Edge intercept:", coefficients[0], 0, 6, "");
    user_dialogue.addNumericField("Edge gradient:", coefficients[1], 0, 6, "");
    user_dialogue.addNumericField("Edge curvature:", coefficients[2], 0, 6, "");
    user_dialogue.addCheckbox("Tune edge coefficients", tune);
    user_dialogue.addCheckbox("Smooth line spead", smooth);
    user_dialogue.addNumericField("Gradient of smooting:", gradient, 0, 6, "");
    user_dialogue.showDialog();

    // read input
    if(user_dialogue.wasCanceled())
      return false;

    if(user_dialogue.invalidNumber()) {
      IJ.error("Error", "Invalid input number");
```

```java
      return false;
    }

    range = (int)(user_dialogue.getNextNumber());
    oversampling = (int)(user_dialogue.getNextNumber());
    coefficients[0] = user_dialogue.getNextNumber();
    coefficients[1] = user_dialogue.getNextNumber();
    coefficients[2] = user_dialogue.getNextNumber();
    tune = user_dialogue.getNextBoolean();
    smooth = user_dialogue.getNextBoolean();
    gradient = user_dialogue.getNextNumber();
    return true;
  }

  public void run(ImageProcessor ip) {

    if(get_user_input()) {
    map shadowMap = new map();
    edge shadowEdge = new edge(oversampling, range, coefficients);

    IJ.log("Calculate modulation transfer. G Moldovan, Oxford 2008");
    IJ.log("Pixel range is "+shadowEdge.range);
    IJ.log("Oversampling is "+shadowEdge.oversampling);
    IJ.log("Edge dimension is "+shadowEdge.dimension);
    IJ.log("Edge coefficients are ");
    for (int i=0; i<shadowEdge.dimension; i++)
      IJ.log("   coefficient "+i+" of "+shadowEdge.coefficients[i]);

    // fine tune edge coefficients
    if (tune) {

      // second coefficient (angle)
      double start = shadowEdge.coefficients[1];
      IJ.log("tuning sencond coefficient from "+ (start-0.002) +" to "+ (start+0.002));
      double end = 0.0;
      double best = 0.0;
      int count = -1;
      for(int i=-10; i<=10; i++) {
        IJ.showProgress(count++, 21); // show progress
        shadowEdge.coefficients[1] = start + i * 0.0002;
        shadowMap = new map();
        shadowMap.read(ip, shadowEdge);
```

```
        shadowMap.align(shadowEdge);
        shadowEdge.read(shadowMap);
        shadowEdge.analyse();
        if (best < shadowEdge.alignment) {
          best = shadowEdge.alignment;
          end = shadowEdge.coefficients[1];
        }
      }
      shadowEdge.coefficients[1] = end;

      // first coefficient (displacement)
      shadowMap = new map();
      shadowMap.read(ip, shadowEdge);
      shadowMap.align(shadowEdge);
      shadowEdge.read(shadowMap);
      shadowEdge.centre();

      // print modifications
      IJ.log("Fine tuned edge coefficients to ");
      for (int i=0; i<shadowEdge.dimension; i++)
        IJ.log("   coefficient "+i+" of "+shadowEdge.coefficients[i]);

    }

    // read profile and spread
    shadowMap.read(ip, shadowEdge); IJ.log("Read "+shadowMap.length+" pixels");
    shadowMap.align(shadowEdge); IJ.log("Aligned using edge parameters");
    shadowEdge.read(shadowMap); IJ.log("Using median to find most significant pixel values"); // debug

    if (smooth)
      shadowEdge.smooth(gradient);
    shadowEdge.analyse();
    shadowEdge.print();
  }
  }
}

class edge {
  int oversampling;
  int range;
  int bins;
  int dimension;
```

```java
  boolean smooth;
  double[] coefficients;
  double[][] counts; // number of pixels at give distance from edge
  double[][] profile; // profile across the edge
  double[][] spread; // line spread of the edge
  double[][] modulation; // modulation transfer of edge
  double alignment; // single coefficient expressing magnitude of spread

  edge(int newOversampling, int newRange, double[] newCoefficients) {
    this.range = newRange;
    this.oversampling = newOversampling;
    this.dimension = (int)newCoefficients.length;
    this.coefficients = new double[this.dimension];
    for(int i=0; i<this.dimension; i++)
      this.coefficients[i] = newCoefficients[i];
    this.bins = this.range * this.oversampling;
    this.counts = new double[3][2*this.bins+1];
    this.profile = new double[3][2*this.bins+1];
    this.spread = new double[3][2*this.bins+1];
    this.modulation = new double[3][this.range+1];
  }

  // calculate y of edge for given x
  double getY (double x) {
    double y=0;
    for(int i=0; i<this.dimension; i++)
      y += this.coefficients[i] * Math.pow(x, i);
    return y;
  }

  // read counts, profile and spread
  void read (map shadowMap) {
    for (int y=0; y<2*this.bins+1; y++) {
      this.counts[0][y] = (y-this.bins)/(this.oversampling*1.0); // compose distance array
      this.profile[0][y] = (y-this.bins)/(this.oversampling*1.0); // compose distance array
      this.spread[0][y] = (y-this.bins)/(this.oversampling*1.0); // compose distance array
      double[] pixelValues = new double[shadowMap.length]; // pixel values at this distance interval
      double[] dPixelValues = new double[shadowMap.length]; // diff(pixelvalues) at this distance
```

```java
            interval
        double minimumY = (y-this.bins-0.5)/this.oversampling; // minimum y for this distance interval
        double maximumY = (y-this.bins+0.5)/this.oversampling; // maximum y for this distance interval
        //IJ.log("minimumY "+minimumY+" maximumY "+maximumY); // debug

        // read pixel values in this y interval
        this.counts[1][y] = 0;
        //IJ.showProgress(y+1, 2*this.bins+1); // show progress
        for (int i=0; i<shadowMap.length-1; i++) {
          if (shadowMap.y[i]>=minimumY && shadowMap.y[i]<maximumY && shadowMap.x[i]==shadowMap.x[i+1]) {
            pixelValues[(int)this.counts[1][y]] = shadowMap.z[i];
            dPixelValues[(int)this.counts[1][y]] = shadowMap.z[i]-shadowMap.z[i+1];
            this.counts[1][y] += 1;
          }
        }
        pixelValues = truncateArray(pixelValues, 0, (int)this.counts[1][y]);
        dPixelValues = truncateArray(dPixelValues, 0, (int)this.counts[1][y]);

        // get most significant value (median, mean or mode)
        this.profile[1][y] = arrayMedian(pixelValues);
        this.profile[2][y] = arrayError(pixelValues);
        this.spread[1][y] = arrayMedian(dPixelValues);
        this.spread[2][y] = arrayError(dPixelValues);
      }
    }

    // fine tune first coefficient
    void centre() {

      // first coefficient
      int centreIndex = arraySymmetryCentre(this.spread[1]); // find centre of edge spread
```

```
    double centrePosition = this.spread[0][centreIndex]; // set new coefficient
    this.coefficients[0] += centrePosition;
  }

  // apply local average starting from edge on each direction
  void smooth (double gradient) {
    this.smooth = true;
    for (int i=0; i<=this.bins; i++) {

      // recalculate period
      int period = (int)(i/gradient);
      if (period > i/2.0) period = (int)(i/2.0);

      // select left average interval using reflection at 0
      int left_start = (int)(this.bins) - i - period;
      if (left_start < 0) left_start = 0;
      int left_end = (int)(this.bins) - i + period;
      if (left_end > (int)(this.bins)) left_end = (int)(this.bins);
      double[] left_average_array = truncateArray(this.spread[1], left_start, left_end);

      // select right average interval using reflection at 2 * distance_bins + 1
      int right_start = (int)(this.bins) + i - period;
      if (right_start < (int)(this.bins)) right_start = (int)(this.bins);
      int right_end = (int)(this.bins) + i + period;
      if (right_end > (int)(2 * this.bins)) right_end = (int)(2 * this.bins);
      double[] right_average_array = truncateArray(this.spread[1], right_start, right_end);

      // get most significant value (median, mean or mode)
      double left_average = arrayMean(left_average_array);
      double right_average = arrayMean(right_average_array);
      this.spread[2][(int)(this.bins) - i] += Math.abs(left_average - this.spread[1][(int)(this.bins) - i]);
```

```
      this.spread[1][(int)(this.bins) - i] = left_average;
      this.spread[2][(int)(this.bins) + i] += Math.abs(right_average - this.spread[1][(int)(this.bins) + i]);
      this.spread[1][(int)(this.bins) + i] = right_average;
    }
    IJ.log("Applying local average on spread using "+gradient);
  }

  // calculate modulation from spread
  void analyse () {
    this.alignment = 0.0; // reset aligment coefficient
    double[] fft_array = arrayAbsoluteFFT(this.spread[1]); // get fft of point spread
    for (int i=0; i < range+1; i++) {
      this.modulation[0][i] = i/(2.0*(this.range)); // compose frequency array
      this.modulation[1][i] = fft_array[i]; // read modulation
      this.alignment += this.modulation[1][i];
    }
    this.modulation[1] = normaliseArray(this.modulation[1]);
  }

  // print results
  void print() {
    PlotWindow countsPlot = new PlotWindow("number of pixels", "distance", "count", this.counts[0], this.counts[1]);
    countsPlot.draw();

    PlotWindow profilePlot = new PlotWindow("edge profile", "distance", "edge profile", this.profile[0], this.profile[1]);
    profilePlot.addErrorBars(Tools.toFloat(this.profile[2]));
    profilePlot.draw();

    PlotWindow spreadPlot;
    if (!smooth)
      spreadPlot = new PlotWindow("edge spread", "distance", "point spread", this.spread[0], this.
```

```
          spread[1]);
    else
      spreadPlot = new PlotWindow("smoothed edge spread",
          "distance", "point spread", this.spread[0],
          this.spread[1]);
    //spreadPlot.setColor(Color.red);
    spreadPlot.addErrorBars(Tools.toFloat(this.spread[2])
        );
    spreadPlot.draw();

    PlotWindow modulationPlot = new PlotWindow("
        modulation transfer", "frequency", "modulation
        transfer", this.modulation[0], this.modulation[1])
        ;
    modulationPlot.draw();
  }

  double arrayMedian (double[] array) {
    for (int outer = 1; outer < (int)(array.length);
        outer++) {
      for (int inner = 0; inner < (int)(array.length)-
          outer; inner++) {

        // read values
        double first = array[inner];
        double second = array[inner + 1];

        // write maximum and minimum
        array[inner] = Math.min(first,second);
        array[inner + 1] = Math.max(first,second);
      }
    }
    double median = array[(int)((int)(array.length)/2)];
    return median;
  }

  double arrayMean (double[] array) {
    double sum = 0.0;
    for (int i=0; i<(int)(array.length); i++)
      sum += array[i];
    double mean =  sum/array.length;
    return mean;
  }

  double arrayError (double[] array) {
    double error = 0.0;
```

```java
    double mean = arrayMean(array);
    for (int i = 0; i < (int)array.length; i++)
      error += Math.pow((array[i] - mean), 2);
    //error = error / (int)array.length;
    error = Math.sqrt(error)/(int)array.length;
    return error;
  }

  double[] arrayAbsoluteFFT(double[] array) {
    double[] abs_fft_array = new double[(int)(array.length)];
    for (int k = 0; k < (int)(array.length); k++) {
      double cos_part = 0;
      double sin_part = 0;
      double constant = -2.0 * Math.PI * k / (int)(array.length);
      for (int n = 0; n < (int)(array.length); n++) {
        cos_part += array[n] * Math.cos(constant * n);
        sin_part += array[n] * Math.sin(constant * n);
      }
      abs_fft_array[k] = Math.sqrt(Math.pow(cos_part,2) + Math.pow(sin_part,2));
    }
    return abs_fft_array;
  }

  double[] normaliseArray (double[] array) {
    double minimum = array[0];
    double maximum = array[0];

    for (int index = 0; index < (int)(array.length); index++)
      minimum = Math.min(minimum, array[index]);
    for (int index = 0; index < (int)(array.length); index++)
      maximum = Math.max(maximum, array[index]);

    for (int index = 0; index < (int)(array.length); index++)
      array[index] = array[index] / maximum;
    return array;
  }

  double[] truncateArray (double[] array, int startIndex, int endIndex) {
    int arrayLenght = endIndex - startIndex + 1;
```

```
      double[] new_array = new double[arrayLenght];
      for (int index = 0; index < arrayLenght; index++)
        new_array[index] = array[index + startIndex];
      return new_array;
    }

    double[] reverseArray (double[] array) {
      double[] newArray = new double[(int)(array.length)];
      for(int i=0; i<(int)(array.length); i++)
        newArray[i] = array[(int)(array.length)-i-1];
      return newArray;
    }

    int arraySymmetryCentre (double[] array) {
      int index = 0;
      double maximum = 0.0;
      double[] match = new double[(int)(array.length)];
      for(int i=10; i<(int)(array.length)-10; i++) {

        // split the array in two
        int arrayLength = Math.min(i, (int)(array.length)-i
            ) - 1;
        double[] leftArray = truncateArray(array, i-
            arrayLength, i);
        double[] rightArray = truncateArray(array, i, i+
            arrayLength);
        rightArray = reverseArray(rightArray);

        // see how straight
        CurveFitter fit = new CurveFitter(leftArray,
            rightArray);
        fit.doFit(CurveFitter.STRAIGHT_LINE);
        match[i] = fit.getRSquared();

        // find position of best match
        if(maximum < match[i]) {
          maximum = match[i];
          index = i;
        }
      }
      return index;
    }
}

class map {
    double[] x; // x coordinates
```

```
double[] y; // y coordinates
double[] z; // pixel values
int length; // number of pixels

map () {
  this.length = 0;
}

void read (ImageProcessor ip, edge shadowEdge) {
  int width = ip.getWidth();
  int height = ip.getHeight();
  double[] fullX = new double[width * height];
  double[] fullY = new double[width * height];
  double[] fullZ = new double[width * height];
  for (int x=0; x<width; x++) {
    if(shadowEdge.getY(x)>=0) {
      for (int y=0; y<height; y++) {
        if((int)(Math.abs(shadowEdge.getY(x) - y)) <= (
            shadowEdge.range + 1)) {
          fullX[this.length] = x;
          fullY[this.length] = y;
          fullZ[this.length] = ip.getPixelValue(x, y);
          this.length++;
        }
      }
    }
  }
  this.x = new double[this.length+1];
  this.y = new double[this.length+1];
  this.z = new double[this.length+1];
  for (int i=0; i<this.length; i++) {
    this.x[i] = fullX[i];
    this.y[i] = fullY[i];
    this.z[i] = fullZ[i];
  }
}

void align (edge shadowEdge) {
  for (int i=0; i<this.length; i++) {
    this.x[i] = this.x[i];
    this.y[i] = this.y[i] - shadowEdge.getY(this.x[i]);
    this.z[i] = this.z[i];
  }
}

void print () {
```

```
      for (int i=0; i<1024; i++) {
        IJ.log(" "+this.x[i]+" "+this.y[i]+" "+this.z[i]);
      }
    }
}
```

A.2 Code for calculation of NPS

```

//Grigore Moldovan, University of Oxford, 2007−2009

import java.awt.*;
import ij.*;
import ij.process.*;
import ij.gui.*;
import ij.plugin.filter.PlugInFilter;
import ij.measure.*;
import ij.util.*;

public class NoisePowerSpectrum_ implements PlugInFilter {
//calculate noise power spectrum of a stack

  // input parameters
  public boolean show_spectra = false; // show spectrum stack?
  public boolean reduce_length = false; // reduce number of points in the output?
  public int spectrum_points = 0;  // number of output points

  // own parameters
  public ImagePlus imp;   // image handle, MUST BE SQUARE AND POWER OF
      TWO
  private ImageStack image_stack;  // stack of images
  private ImageStack spectrum_stack; // stack of NPS
  private int spectrum_slices;  // number of slices
  private int spectrum_size;  // image size in pixels
  private int spectrum_radius;  // spectrum radius in pixels
  private double[] spectrum_frequency; // NPS azimuthal frequency (1/pixels)
  private double[] spectrum_count;  // NPS azimuthal count
  private double[] spectrum_average; // NPS azimuthal average
  private double[] spectrum_error;  // NPS azimuthal standard error

  public int setup(String arg, ImagePlus imp) {
    if (arg.equals("about")) {
      show_about();
      return DONE;
    }
```

```
    // get initial values
    image_stack = imp.getStack();

    return DOES_ALL;
  }

  private void show_about() {
    IJ.showMessage("About...", "Calculate azimuthal profile of noise power spectrum. G Moldovan, Oxford 2007-2009");
  }

  private boolean get_user_input() {

    // show dialogue
    GenericDialog user_dialogue = new GenericDialog("Noise Power Spectrum Azimuthal Profile");
    user_dialogue.addCheckbox("Reduce size of output", reduce_length);
    user_dialogue.addNumericField("Size of output:", spectrum_points, 0, 4, "pixels ");
    user_dialogue.addCheckbox("Show spectra", reduce_length);
    user_dialogue.showDialog();

    // read input
    if(user_dialogue.wasCanceled())
      return false;

    if(user_dialogue.invalidNumber()) {
      IJ.error("Error", "Invalid input number");
      return false;
    }

    reduce_length = user_dialogue.getNextBoolean();
    spectrum_points = (int)(user_dialogue.getNextNumber());
    show_spectra = user_dialogue.getNextBoolean();
    return true;
  }

  public void run(ImageProcessor stack_processor) {

    // get user input on final spectrum size
    if(get_user_input()) {

      // get stack of spectra
      spectrum_stack = get_stack_spectrum();
      spectrum_slices = spectrum_stack.getSize();
```

```
        spectrum_size = spectrum_stack.getWidth();
        spectrum_radius = spectrum_size / 2 - 1;

        // get azimuthal spectrum from stack
        spectrum_frequency = get_stack_azimuthal_frequency();
        spectrum_count = get_stack_azimuthal_count();
        spectrum_average = get_stack_azimuthal_average();
        spectrum_error = get_stack_azimuthal_error();

        // reduce spectrum size
        if (reduce_length == true) {
            spectrum_frequency = reduce_spectrum_length(spectrum_frequency);
            spectrum_count = reduce_spectrum_length(spectrum_count);
            spectrum_average = reduce_spectrum_length(spectrum_average);
            spectrum_error = reduce_spectrum_length(spectrum_error);
        }

        // plot spectrum and log analysis
        if (show_spectra)
            show_spectra();
        plot_spectrum();
        log_spectrum();
    }
}

private ImageStack get_stack_spectrum () {
// calculate noise power spectrum of an image

    // get spectrum for each slice
    ImageStack ps_stack = new ImageStack(image_stack.getWidth(), image_stack.getWidth());
    for (int slice = 1; slice <= image_stack.getSize(); slice++)
        ps_stack.addSlice("", get_slice_power_spectrum(image_stack.getProcessor(slice)));

    return ps_stack;
}

private double[] get_stack_azimuthal_frequency () {
// return frequency array from image size
    double [] stack_azimuthal_frequency = new double[spectrum_radius];
    for (int index = 0; index < spectrum_radius; index++)
        stack_azimuthal_frequency[index] = (double)(index) / (double)(spectrum_size - 4);

    return stack_azimuthal_frequency;
```

```
}

private double[] get_stack_azimuthal_count () {
// return pixel count array from image and stack size

   double[] stack_azimuthal_count = new double[spectrum_radius];

   stack_azimuthal_count = get_slice_azimuthal_count();

   // insert stack size
   for (int index = 0; index < spectrum_radius; index++)
      stack_azimuthal_count[index] *= (double)(spectrum_slices);

   return stack_azimuthal_count;
}

private double[] get_stack_azimuthal_average () {
// get average azimuthal profile of all stack. spectrum_count should have been calculated at this point

   // read average from all slices
   double[][] all_slices_azimuthal_average = new double[spectrum_slices][spectrum_radius];
   for (int slice = 1; slice <= spectrum_slices; slice++) {

      // get sum from one slice
      double[] slice_azimuthal_average = get_slice_azimuthal_sum(spectrum_stack.getProcessor(slice));

      // copy results to memory
      for (int index = 0; index < spectrum_radius; index++)
         all_slices_azimuthal_average[slice - 1][index] = slice_azimuthal_average[index];
   }

   // calculate average
   double[] stack_azimuthal_average = new double[spectrum_radius];
   for (int index = 0; index < spectrum_radius; index++) {
      for (int image = 1; image <= spectrum_slices; image++)
         stack_azimuthal_average[index] += all_slices_azimuthal_average[image - 1][index];

      stack_azimuthal_average[index] /= spectrum_count[index];
   }

   return stack_azimuthal_average;
```

```
}

private double[] get_stack_azimuthal_error () {
// get error in azimuthal profile of all stack. spectrum_count should have been calculated at this point

  // read variance from all slices
  double [][] all_slices_azimuthal_variance = new double[spectrum_slices][spectrum_radius];
  for (int slice = 1; slice <= spectrum_slices; slice++) {

    // get variance from one slice
    double[] slice_azimuthal_variance = get_slice_azimuthal_variance(spectrum_stack.getProcessor(slice));

    // copy results to memory
    for (int index = 0; index < spectrum_radius; index++)
      all_slices_azimuthal_variance[slice - 1][index] = slice_azimuthal_variance[index];
  }

  // calculate total variance
  double[] stack_azimuthal_variance = new double[spectrum_radius];
  for (int index = 0; index < spectrum_radius; index++) {
    for (int image = 1; image <= spectrum_slices; image++)
      stack_azimuthal_variance[index] += all_slices_azimuthal_variance[image - 1][index];
  }

  // calculate standard deviation
  double[] stack_azimuthal_standard_deviation = new double[spectrum_radius];
  for (int index = 0; index < spectrum_radius; index++)
     stack_azimuthal_standard_deviation[index] = Math.sqrt(stack_azimuthal_variance[index] / spectrum_count[index]);

  // calculate standard error
  double[] stack_azimuthal_standard_error = new double[spectrum_radius];
  for (int index = 0; index < spectrum_radius; index++)
     stack_azimuthal_standard_error[index] = stack_azimuthal_standard_deviation[index] / Math.sqrt(spectrum_count[index]);

  return stack_azimuthal_standard_error;
}

private ImageProcessor get_slice_power_spectrum (ImageProcessor ip) {

```

```
    // get row power specturm
    FHT fht = new FHT(ip);
    fht.setShowProgress(false);
    fht.transform();
    FHT ps = fht.conjugateMultiply(fht);
    ps.swapQuadrants();

    // get corrected power spectrum
    ps.multiply(1.0/(ip.getWidth()*ip.getHeight()));

    return ps;
  }

  private double[] get_slice_azimuthal_count () {
  // get average azimuthal profile for this image

    double[] azimuthal_count = new double[spectrum_radius];

    // loop between image pixels
    for (int x = 0; x < spectrum_size; x++) {
      for (int y = 0; y < spectrum_size; y++) {
        int distance = (int)(Math.sqrt(Math.pow((spectrum_size / 2.0 - x),2) +
            Math.pow((spectrum_size / 2.0 - y), 2)));
        if (distance < spectrum_radius)
          azimuthal_count[distance]++;
      }
    }

    return azimuthal_count;
  }

  private double[] get_slice_azimuthal_sum (ImageProcessor image_processor) {
  // get integrated azimuthal profile for this image

    double[] azimuthal_sum = new double[spectrum_radius];

    // loop between image pixels
    for (int x = 0; x < spectrum_size; x++) {
      for (int y = 0; y < spectrum_size; y++) {
        int distance = (int)(Math.sqrt(Math.pow((spectrum_size / 2.0 - x), 2) +
            Math.pow((spectrum_size / 2.0 - y), 2)));
        if (distance < spectrum_radius)
          azimuthal_sum[distance] += image_processor.getPixelValue(x, y);
      }
    }

```

```
        return azimuthal_sum;
    }

    private double[] get_slice_azimuthal_variance (ImageProcessor image_processor) {
    // get variance in azimuthal profile for this image. spectrum_average should have
        been calculated at this point

        double[] azimuthal_variance = new double[spectrum_radius];

        // loop between image pixels
        for (int x = 0; x < spectrum_size; x++) {
            for (int y = 0; y < spectrum_size; y++) {
                int distance = (int)(Math.sqrt(Math.pow((spectrum_size / 2.0 - x), 2) +
                    Math.pow((spectrum_size / 2.0 - y), 2)));
                if (distance < spectrum_radius)
                    azimuthal_variance[distance] += Math.pow((image_processor.
                        getPixelValue(x, y) - spectrum_average[distance]), 2);
            }
        }

        return azimuthal_variance;
    }

    private double[] reduce_spectrum_length (double[] full_spectrum) {
    // reduce length of full_spectrum to spectrum_points

        double[] reduced_spectrum = new double[spectrum_points];

        for (int new_index = spectrum_points - 1; new_index >= 0; new_index--) {
            int old_index = (new_index * (spectrum_radius - 1) / (spectrum_points - 1));
            reduced_spectrum[new_index] = full_spectrum[old_index];
        }

        return reduced_spectrum;
    }

    private void plot_spectrum () {
    // print data for inspection and make available for saving

        PlotWindow plot = new PlotWindow("noise␣power␣spectrum", "frequency␣(1/
            pixel)", "noise␣power␣spectrum", spectrum_frequency, spectrum_average);
        plot.addErrorBars(Tools.toFloat(spectrum_error));
        plot.draw();
    }

    private void log_spectrum () {
```

```
// log parameters used in this run

    IJ.log("Azimuthal profile of Noise Power Spectrum...");
    IJ.log("Number of slices in the input stack "+spectrum_slices);
    IJ.log("Size of power spectrum images "+spectrum_size);
    IJ.log("Length of azimuthal profile "+spectrum_radius);
    if (reduce_length == true)
      IJ.log("Spectrum size reduced to "+spectrum_points);
  }

  private void show_spectra () {
  // show the stack of spectra

    ImagePlus spectrum_processor = new ImagePlus("PS stack", spectrum_stack);
    spectrum_processor.show();
  }
}
```

Bibliography

[1] Deptuch, G., Besson, A., Rehak, P., Szelezniak, M., Wall, J., Winter, M. and Zhu, Y. (2007) *Direct electron imaging in electron microscopy with monolithic active pixel sensors*, Ultramicroscopy, **107**(8):674.

[2] McMullan, G., Chen, S., Henderson, R. and Faruqi, A. R. (2009) *Detective quantum efficiency of electron area detectors in electron microscopy*, Ultramicroscopy, **109**(9):1126.

[3] McMullan, G., Cattermole, D. M., Chen, S., Henderson, R., Llopart, X., Summerfield, C., Tlustos, L. and Faruqi, A. R. (2007) *Electron imaging with Medipix2 hybrid pixel detector*, Ultramicroscopy, **107**(4-5):401.

[4] Roberts, P. T. E., Chapman, J. N. and Macleod, A. M. (1982) *A CCD-Based Image Recording-System for the CTEM*, Ultramicroscopy, **8**(4):385.

[5] Milazzo, A. C., Leblanc, P., Duttweiler, F., Jin, L., Bouwer, J. C., Peltier, S., Ellisman, M., Bieser, F., Matis, H. S., Wieman, H., Denes, P., Kleinfelder, S. and Xuong, N. H. (2005) *Active pixel sensor array as a detector for electron microscopy*, Ultramicroscopy, **104**(2):152.

[6] Faruqi, A. R., Henderson, R., Pryddetch, M., Allport, P. and Evans, A. (2006) *Direct single electron detection with a CMOS detector for electron microscopy*, Nuclear Instruments & Methods in Physics Research Section A-Accelerators Spectrometers Detectors and Associated Equipment, **566**(2):770.

[7] Janesick, J. and Putnam, G. (2003) *Developments and applications of high-performance CCD and CMOS imaging arrays*, Annual Review of Nuclear and Particle Science, **53**(1):263.

[8] Moldovan, G., Li, X. and Kirkland, A. (2008) *Can direct electron detectors outperform phosphor-CCD systems for TEM?*, EMAG: Electron Microscopy and Analysis Group Conference 2007, **126**:C012089.

[9] FEI, *Falcon II Direct Electron Detector*, <http://www.fei.com/products/falcon-2/> [2015].

[10] Gatan Inc, *Gatan Digital Imaging*, <http://www.gatan.com/techniques/digital-imaging> [2012].

[11] Direct Electron, *DE-12 Camera Specification*, <http://www.directelectron.com/documents/Specs-DE12.pdf> [2013].

[12] Medipix Collaboration, *The Medipix Homepage*, <http://medipix.web.cern.ch/medipix/> [2012].

[13] Faruqi, A. R. (2001) *Prospects for hybrid pixel detectors in electron microscopy*, Nuclear Instruments & Methods in Physics Research Section A-Accelerators Spectrometers Detectors and Associated Equipment, **466**(1):146.

[14] Fornaini, A., Calvet, D. and Visschers, J. L. (2001) *Soft X-ray sensitivity of a photon-counting hybrid pixel detector with a silicon sensor matrix*, Nuclear Instruments and Methods in Physics Research Section A: Accelerators, Spectrometers, Detectors and Associated Equipment, **466**(1):142.

[15] Faruqi, A. R., Cattermole, D. M., Henderson, R., Mikulec, B. and Raeburn, C. (2003) *Evaluation of a hybrid pixel detector for electron microscopy*, Ultramicroscopy, **94**(3-4):263.

[16] Faruqi, A. R., Henderson, R. and Tlustos, L. (2005) *Noiseless direct detection of electrons in Medipix2 for electron microscopy*, Nuclear Instruments & Methods in Physics Research Section A-Accelerators Spectrometers Detectors and Associated Equipment, **546**(1-2):160.

[17] McMullan, G. and Faruqi, A. R. (2008) *Electron microscope imaging of single particles using the Medipix2 detector*, Nuclear Instruments & Methods in Physics Research Section A-Accelerators Spectrometers Detectors and Associated Equipment, **591**(1):129.

[18] Meyer, R. R. and Kirkland, A. I. (2009), *Direct Electron Detector*, patent: US7888761.

[19] Johnson, L. C., Campbell, D. L., Hull, E. L. and Peterson, T. E. (2011) *Characterization of a high-purity germanium detector for small-animal SPECT*, Physics in Medicine and Biology, **56**(18):5877.

[20] Shokouhi, S., McDonald, B. S., Durko, H. L., Fritz, M. A., Furenlid, L. R. and Peterson, T. E. (2009) *Thick Silicon Double-Sided Strip Detectors for Low-Energy Small-Animal SPECT*, IEEE Transactions on Nuclear Science, **56**(3):557.

[21] Peterson, T. E., Wilson, D. W. and Barrett, H. H. (2004) *Ultrahigh-resolution small-animal Imaging using a silicon detector*, IEEE Nuclear Science Symposium, Conference Record, **1-5**.

[22] Moldovan, G., Li, X., Wilshaw, P. and Kirkland, A. (2008) *Thin silicon strip devices for direct electron detection in transmission electron microscopy*, Nuclear Instruments and Methods in Physics Research Section A: Accelerators, Spectrometers, Detectors and Associated Equipment, **591**(1):134.

[23] Gontard, L. C., Moldovan, G., Carmona-Galn, R., Lin, C. and Kirkland, A. I. (2014) *Detecting single-electron events in TEM using low-cost electronics and a silicon strip sensor*, Microscopy, **63**(2):119.

[24] Yang, H., Pennycook, T. and Nellist, P. D. (2014) *Maximising Phase Contrast in Aberration-corrected STEM using Pixelated Detectors*, in *18th International Microscopy Congress Proceedings*.

[25] Turchetta, R., Berst, J. D., Casadei, B., Claus, G., Colledani, C., Dulinski, W., Hu, Y., Husson, D., Normand, J. P. L., Riester, J. L., Deptuch, G., Goerlach, U., Higueret, S. and Winter, M. (2001) *A monolithic active pixel sensor for charged particle tracking and imaging using standard VLSI CMOS technology*, Nuclear Instruments & Methods in Physics Research Section A-Accelerators Spectrometers Detectors and Associated Equipment, **458**(3):677.

[26] Stanitzki, M. (2011) *Advanced monolithic active pixel sensors for tracking, vertexing and calorimetry with full CMOS capability*, Nuclear Instruments and Methods in Physics Research Section A: Accelerators, Spectrometers, Detectors and Associated Equipment, **650**(1):178.

[27] Velthuis, J. J., Cussans, D., Goldstein, J., Page, R., Wilson, J. A., Worm, S. D., Coath, R. E., Crooks, J. P., Dauncey, P. D., Gao, R., Head, R., Miller, O. D., Nash, S., Nomerotski, A., Price, T., Rajovic, V., Stanitzki, M., Strube, J., Turchetta, R., Tyndel, M., Watson, N. K. and Zhang, Z. (2011) *Beam test results of FORTIS, a 4T MAPS sensor with a signal-to-noise ratio exceeding 100*, Journal of Instrumentation, **6**:P12006.

[28] Lauxtermann, S., Lee, A., Stevens, J. and Joshi, A. (2007) *Comparison of Global Shutter Pixels for CMOS Image Sensors*, in *Proceedings of the International Image Sensor Workshop*, page 82.

[29] Moldovan, G., Jeffery, B., Nomerotski, A. and Kirkland, A. (2009) *Imaging modes for direct electron detection in TEM with column parallel CCD*, Nuclear Instruments and Methods in Physics Research Section A: Accelerators, Spectrometers, Detectors and Associated Equipment, **607**(1):13.

[30] McMullan, G., Clark, A. T., Turchetta, R. and Faruqi, A. R. (2009) *Enhanced imaging in low dose electron microscopy using electron counting*, Ultramicroscopy, **109**(12):1411.

[31] McMullan, G., Turchetta, R. and Faruqi, A. R. (2011) *Single event imaging for electron microscopy using MAPS detectors*, Journal of Instrumentation, **6**:C04001.

[32] Battaglia, M., Contarato, D., Denes, P. and Giubilato, P. (2009) *Cluster imaging with a direct detection CMOS pixel sensor in Transmission Electron Microscopy*, Nuclear Instruments & Methods in Physics Research Section A-Accelerators Spectrometers Detectors and Associated Equipment, **608**(2):363.

[33] Mooney, P., Contarato, D., Denes, P., Gubbens, A., Lee, B., Lent, M. and Agard, D. (2011) *A High-Speed Electron-Counting Direct Detection Camera for TEM*, Microscopy and Microanalysis, **17**(Supplement S2):1004.

[34] Gatan Inc, *Direct Detection - Configurations and Specifications*, <http://www.gatan.com/products/tem-imaging-spectroscopy/k2-direct-detection-cameras> [2012].

[35] Deptuch, G., Claus, G., Colledani, C., Deveaux, M., Gay, A., Dulinski, W., Gornushkin, Y., Hu-Guo, C. and Winter, M. (2003) *Development of monolithic active pixel sensors for charged particle tracking*, Nuclear Instruments and Methods in Physics Research Section A: Accelerators, Spectrometers, Detectors and Associated Equipment, **511**(1-2):240.

[36] Deptuch, G., Dulinski, W., Caccia, M. and Winter, M. (2005) *High-resolution, back-side illuminated monolithic active pixel sensor for low-energy electron imaging*, Nuclear Science, IEEE Transactions on, **52**(5):1745.

[37] Jin, L., Milazzo, A.-C., Kleinfelder, S., Li, S., Leblanc, P., Duttweiler, F., Bouwer, J. C., Peltier, S. T., Ellisman, M. H. and Xuong, N.-H. (2008) *Applications of*

direct detection device in transmission electron microscopy, Journal of structural biology, **161**(3):352.

[38] Milazzo, A.-C., Moldovan, G., Lanman, J., Jin, L., Bouwer, J. C., Klienfelder, S., Peltier, S. T., Ellisman, M. H., Kirkland, A. I. and Xuong, N.-H. (2010) *Characterization of a direct detection device imaging camera for transmission electron microscopy*, Ultramicroscopy, **110**(7):741.

[39] McMullan, G., Faruqi, A. R., Henderson, R., Guerrini, N., Turchetta, R., Jacobs, A. and van Hoften, G. (2009) *Experimental observation of the improvement in MTF from backthinning a CMOS direct electron detector*, Ultramicroscopy, **109**(9):1144.

[40] Battaglia, M., Contarato, D., Denes, P., Doering, D., Duden, T., Krieger, B., Giubilato, P., Gnani, D. and Radmilovic, V. (2010) *Characterisation of a CMOS active pixel sensor for use in the TEAM microscope*, Nuclear Instruments & Methods in Physics Research Section A-Accelerators Spectrometers Detectors and Associated Equipment, **622**(3):669.

[41] Guerrini, N., Turchetta, R., Hoften, G. V., Henderson, R., McMullan, G. and Faruqi, A. R. (2011) *A high frame rate, 16 million pixels, radiation hard CMOS sensor*, Journal of Instrumentation, **6**:C03003.

[42] Contarato, D., Denes, P., Doering, D., Joseph, J. and Krieger, B. (2011) *Direct detection in Transmission Electron Microscopy with a 5 μm pitch CMOS pixel sensor*, Nuclear Instruments & Methods in Physics Research Section A-Accelerators Spectrometers Detectors and Associated Equipment, **635**(1):69.

[43] Li, X., Zheng, S. Q., Egami, K., Agard, D. A. and Cheng, Y. (2013) *Influence of electron dose rate on electron counting images recorded with the K2 camera*, Journal of structural biology, **184**(2):251.

[44] Ruskin, R. S., Yu, Z. and Grigorieff, N. (2013) *Quantitative characterization of electron detectors for transmission electron microscopy*, Journal of structural biology, **184**(3):385.

[45] McMullan, G., Faruqi, A. R., Clare, D. and Henderson, R. (2014) *Comparison of optimal performance at 300 keV of three direct electron detectors for use in low dose electron microscopy*, Ultramicroscopy, **147**:156.

[46] Lindström, G. (2003) *Radiation damage in silicon detectors*, Nuclear Instruments and Methods in Physics Research Section A: Accelerators, Spectrometers, Detectors and Associated Equipment, **512**(1-2):30.

[47] Faruqi, A. R., Henderson, R. and Holmes, J. (2006) *Radiation damage studies on STAR250 CMOS sensor at 300keV for electron microscopy*, Nuclear Instruments & Methods in Physics Research Section A-Accelerators Spectrometers Detectors and Associated Equipment, **565**(1):139.

[48] Battaglia, M., Contarato, D., Denes, P., Doering, D., P.Giubilato, Kim, T. S., Mattiazzo, S., Radmilovic, V. and Zalusky, S. (2009) *A rad-hard CMOS active pixel sensor for electron microscopy*, Nuclear Instruments & Methods in Physics Research Section A-Accelerators Spectrometers Detectors and Associated Equipment, **598**(2):642.

[49] Anelli, G., Campbell, M., Delmastro, M., Faccio, F., Floria, S., Giraldo, A., Heijne, E., Jarron, P., Kloukinas, K., Marchioro, A., Moreira, P. and Snoeys, W. (1999) *Radiation tolerant VLSI circuits in standard deep submicron CMOS technologies for the LHC experiments: practical design aspects*, Nuclear Science, IEEE Transactions on, **46**(6):1690.

[50] Eid, E.-S., Chan, T. Y., Fossurn, E. R., Tsai, R. H., Spagnuolo, R., Deily, J., Jr., W. B. B. and Peden, J. C. (2001) *Design and characterization of ionizing radiation-*

tolerant CMOS APS image sensors up to 30 Mrd (Si) total dose, Nuclear Science, IEEE Transactions on, **48**(6):1796.

[51] Xue, F., Ping, L., Wei, L., Bin, Z., Xiaodong, X., Gang, W., Bin, H. and Yahong, Z. (2011) *Gate-enclosed NMOS transistors*, Journal of Semiconductors, **32**(8):084002.

[52] Mooney, P. and Gubbens, A. (2009), *Passive Pixel Direct Detection Sensor*, patent: US 20100123077.

[53] Milazzo, A.-C., Cheng, A., Moeller, A., Lyumkis, D., Jacovetty, E., Polukas, J., Ellisman, M. H., Xuong, N.-H., Carragher, B. and Potter, C. S. (2011) *Initial evaluation of a direct detection device detector for single particle cryo-electron microscopy*, Journal of structural biology, **176**(3):404.

[54] Ludtke, S. J., Baker, M. L., Chen, D.-H., Song, J.-L., Chuang, D. T. and Chiu, W. (2008) *De Novo Backbone Trace of GroEL from Single Particle Electron Cryomicroscopy*, Structure, **16**(3):441.

[55] Stagg, S. M., Lander, G. C., Quispe, J., Voss, N. R., Cheng, A., Bradlow, H., Bradlow, S., Carragher, B. and Potter, C. S. (2008) *A test-bed for optimizing high-resolution single particle reconstructions*, Journal of structural biology, **163**(1):29.

[56] Bammes, B. E., Rochat, R. H., Jakana, J., Chen, D.-H. and Chiu, W. (2012) *Direct electron detection yields cryo-EM reconstructions at resolutions beyond 3/4 Nyquist frequency*, Journal of structural biology, **177**(3):589.

[57] Brilot, A. F., Chen, J. Z., Cheng, A., Pan, J., Harrison, S. C., Potter, C. S., Carragher, B., Henderson, R. and Grigorieff, N. (2012) *Beam-induced motion of vitrified specimen on holey carbon film*, Journal of structural biology, **177**(3):630.

[58] Meyer, R. R. and Kirkland, A. (1998) *The effects of electron and photon scattering on signal and noise transfer properties of scintillators in CCD cameras used for electron detection*, Ultramicroscopy, **75**(1):23.

[59] Meyer, R. R. (2002), *Quantitative Automated Object Wave Restoration in High-Resolution Electron Microscopy*, unpublished Doctor Rerum Naturalium Thesis, Technischen Universität Dreseden.

[60] Joy, D. C. (1995) *The single scattering model*, pages 25–37, Monte Carlo Modeling for Electron Microscopy and Microanalysis, Oxford University Press, Oxford/New York, 1st edition.

[61] Livingston, M. S. and Bethe, H. A. (1937) *Nuclear Physics C. Nuclear Dynamics, Experimental*, Rev. Mod. Phys., **9**(3):245.

[62] Bethe, H. (1930) *Zur Theorie des Durchgangs schneller Korpuskularstrahlen durch Materie*, Annalen der Physik, **397**(3):325.

[63] Rutherford, E. (1911) *The Scattering of Î± and Î² Particles by Matter and the Structure of the Atom*, Philosophical Magazine, **21**:669.

[64] Gauvin, R. and Lesperance, G. (1992) *A Monte-Carlo code to simulate the effect of fast secondary electrons on K(ab) factors and spatial-resolution in the TEM*, Journal of Microscopy, **168**:153.

[65] Bishop, H. E. (1975) *The history and development of Monte Carlo methods for use in X-Ray microanalysis.*, in Heinrich, K. F. J., Newbury, D. E. and Yakowitz, H. (Editors), *Use of Monte Carlo Calculations in Electron Probe Microanalysis and Scanning Electron Microscopy*, page 5, U.S. Department of Commerce.

[66] Newbury, D. E. and Myklebust, R. L. (1981) *A Monte Carlo Electron Trajectory Simulation For Analytical Electron Microscopy*, in Geiss, R. H. (Editor), *Analytical Electron Microscopy*, page 91, San Francisco Press.

[67] Meyer, R. R., Kirkland, A. I., Dunin-Borkowski, R. E. and Hutchison, J. L. (2000) *Experimental characterisation of CCD cameras for HREM at 300 kV*, Ultramicroscopy, **85**(1):9.

[68] de Ruijter, W. J. and Weiss, J. K. (1992) *Methods to measure properties of slow-scan CCD cameras for electron detection*, Review of Scientific Instruments, **63**(10):4314.

[69] den Broek, W. V., Aert, S. V. and Dyck, D. V. (2012) *Fully Automated Measurement of the Modulation Transfer Function of Charge-Coupled Devices above the Nyquist Frequency*, Microscopy and Microanalysis, **18**(02):336.

[70] Vulovic, M., Rieger, B., van Vliet, L. J., Koster, A. J. and Ravelli, R. B. G. (2010) *A toolkit for the characterization of CCD cameras for transmission electron microscopy*, Acta Crystallographica Section D-Biological Crystallography, **66**:97.

[71] Faruqi, A. R. and McMullan, G. (2011) *Electronic detectors for electron microscopy*, Quarterly reviews of biophysics, **44**(3):357.

[72] Zuo, J. M. (2000) *Electron detection characteristics of a slow-scan CCD camera, imaging plates and film, and electron image restoration*, Microscopy research and technique, **49**(3):245.

[73] Gao, S., Kang, R. K., Guo, D. M. and Huang, Q. S. (2010) *Study on the Subsurface Damage Distribution of the Silicon Wafer Ground by Diamond Wheel*, Advanced Materials Research, **126-128**:113.

[74] Potts, P. (1987) page 336, A Handbook of Silicate Rock Analysis, Blackie.

[75] Thurber, W. R., Mattis, R. L., Liu, Y. M. and Filliben, J. J. (1980) *Resistivity and Dopant Density Relationship for Boron Doped Silicon*, J. Electrochem. Soc., **127**(10):2291.

[76] Tyagi, M. S. and Overstraeten, R. V. (1983) *Minority carrier recombination in heavily-doped silicon*, Solid-State Electronics, **26**(6):577.

[77] Ibe, O. C. (2013) *One-Dimensional Random Walk* in *Elements of Random Walk and Diffusion Processes*, Wiley.

[78] Anaxagoras, T., Fant, A., Allinson, N., Riley, G., Kent, P., Powell, N., Moldovan, G., Rodenburg, J. and Kirkland, A. (2010) *DUOS - Two-Speed Imager Within the Same Pixel Array*, in Solorzano, G. and de Souza, W. (Editors), *Proceedings of the 17th International Microscopy Congress*.

[79] Littmark, U. (1980) *Handbook of range distributions for energetic ions in all elements*, New York ; Oxford : Pergamon Press, New York ; Oxford.

[80] Brewer Science, *Brewer Science ProTEK B3*, <http://www.brewerscience.com/uploads/products/protek/datasheets/ds_protek_b3.pdf> [2015].

[81] Clough, R. (2011), *Large-Area Thin Free-Standing Imaging Devices*, unpublished MEng Thesis, University of Oxford.

[82] Microchemicals *AZ5214 E Image Reversal Photoresist*, <http://www.microchemicals.com/micro/az_5214e.pdf> [2015].

[83] Dingley, D. (2004) *Progressive steps in the development of electron backscatter diffraction and orientation imaging microscopy*, Journal of microscopy, **213**(3):214.

[84] Groeber, M. A., Haley, B. K., Uchic, M. D., Dimiduk, D. M. and Ghosh, S. (2006) *3D reconstruction and characterization of polycrystalline microstructures using a FIB-SEM system*, Materials Characterization, **57**(4-5):259.

[85] Wilkinson, A. J., Meaden, G. and Dingley, D. J. (2006) *High resolution mapping of strains and rotations using electron backscatter diffraction*, Materials Science and Technology, **22**(11):1271.

[86] Mukai, M., Ikeda, A., Zhou, J., Kaneyama, T., Young, N., Nellist, P. and Kirkland, A. (2010) *Development of a 200kV aberration corrected analytical electron microscope equipped with a monochromator*, in *17th International Microscopy Congress*, IOP.

[87] Gatan Inc, *Ultrascan Camera*, <http://www.gatan.com/products/tem-imaging-spectroscopy/ultrascan-camera> [2012].

[88] MathWorks, *Curve Fitting Toolbox*, <http://uk.mathworks.com/products/curvefitting/> [2015].

[89] Kroon, D.-J. and Slump, C. H. (2009) *MRI Modalitiy Transformation in Demon Registration*, IEEE Internaional Symposium on Biomedical Imaging - From Nano to Macro.

[90] Cachier, P., Pennec, X. and Ayache, N. (1999) *Fast non rigid matching by gradient descent: Study and improvements of the "demons" algorithm*, Technical Report INRIA, **RR-3706**.

[91] Wang, H., Dong, L., O'Daniel, J., Mohan, R., Garden, A. S., Ang, K. K., Kuban, D. A., Bonnen, M., Chang, J. Y. and Cheung, R. (2005) *Validation of an accelerated "demons" algorithm for deformable image registration in radiation therapy*, Physics in Medicine and Biology, **50**(12):2887.

[92] Jones, L., Yang, H., Pennycook, T. J., Marshall, M. S., VanAert, S., Browning, N. D., Castell, M. R. and Nellist, P. D. (2015), *Smart Align - A new tool for Robust Non-rigid Registration of Scanning Microscope Data*, paper submitted to *Advances in Structural and Chemical Imaging*.

[93] Gatan Inc, *OneView Camera*, <http://www.gatan.com/products/tem-imaging-spectroscopy/oneview-camera> [2014].

[94] Ionascut-Nedelcescu, A., Carlone, C., Houdayer, A., von Bardeleben, H. J., Cantin, J. L. and Raymond, S. (2002) *Radiation hardness of gallium nitride*, IEEE Transactions on Nuclear Science, **49**(6):2733.